ADVANCED MR DIFFUSION ANALYSIS IN LIVER

ADVANCED MAGNETIC RESONANCE (MR) DIFFUSION ANALYSIS IN HEALTHY HUMAN LIVER

By
ol

A Thesis

Submitted to the School of Graduate Studies

In Partial Fulfillment of the Requirements for the Degree

Doctor of Philosophy

McMaster University

Doctor of Philosophy (2015)

McMaster University, Department of Medical Physics and Applied Radiation Science, Hamilton, Ontario

TITLE:	Advanced Magnetic Resonance (MR) Diffusion Analysis in Healthy Human Liver
AUTHOR:	Oi Lei Wong (Hon) B.Sc., M.Sc. (McMaster University), M.Sc (Hong Kong University of Science and Technology)
SUPERVISOR:	Michael D. Noseworthy
NUMBER OF PAGES:	xvii, 155

ABSTRACT

Diagnosing diffuse liver disease first involves measurement of blood enzymes followed by biopsy. However, blood markers lack spatial and diagnostic specificity and biopsy is highly risky and variable. Although structural changes have been evaluated using diffusion weighted imaging (DWI), the technique is minimally quantitative. Quantitative MR diffusion approaches, such as intra-voxel incoherent motion (IVIM) and diffusion tensor imaging (DTI) have been proposed to better characterize diseased liver. However, the so called pseudo-hepatic artefact due to cardiac motion, drastically affects DWI results. The overall goals of this thesis were thus to evaluate the pseudo-hepatic anisotropy artefact on the quality of diffusion tensor (DT) and IVIM metrics, and to identify potential solutions.

Intra- and intersession DTI repeatability was evaluated in healthy human livers when varying the number of diffusion encoding gradients (NGD) and number of signal averages (NSA). Although no further advantage was observed with increasing NGD beyond 6 directions, increased NSA improved intra- and inter-session repeatability. The pseudo-hepatic artefact resulted in increased fractional anisotropy (FA) and tensor eigenvalues (λ_1, λ_2, λ_3), most prominent in the left liver lobe during systole of the cardiac cycle. Without taking advantage of tensor directional information, increasing the acquired NGD slightly improved

IVIM fit quality thus helping to minimize the pseudo-hepatic artefact. Combining IVIM and DTI resulted in FA values closer to the hypothesized value of 0.0, which, based on liver microstructure is most logical. Although both IVIM-DTI and DTI-IVIM exhibited similar fit R^2 values, the latter failed more often, especially near major blood vessels. Thus, IVIM-DTI was concluded to be more robust and thus the better approach.

ACKNOWLEDGEMENTS

Special thanks should be given to my supervisor, Dr. Michael Noseworthy, for his guidance and support. All those midnight and sun-rise skype sessions across the globe and travelling adventures will not be forgotten. I wish to give my deepest appreciation to my PhD committee; Dr. Raimond Wong, Dr. Tom Farrell and Dr. Ryan Rebello, whose help shaping this project.

I would like to acknowledge the members of the IRC for their mentorship and companionship (Arv, Andrew, Graham, Ali, Norm, Sergi, Peter Shefield, Steve, Evan, Gavin, Brendon, Alex, Raghda, Alireza, Ben, Conrad, Peter Bevan, Jeff, Saurabh, Paul, Marla and Olga). In particular, special thanks are given to Alyaa for all the poof reading and mental support. I wish to thanks the MR technologists of IRC (Cheryl, Julie, Janet and Toni), and co-ordinators (Edward, Raymond and Betty) and MR technologista of the Department of Interventional and Diagnostic of radiology of Hong Kong Sanatorium & Hospital (Benny, Michael, Polo, Charles, Tat, Cura, Kit, Johnny and Winnie). Without their support, my PhD would not be possible.

Special thanks are also given to the research team (Silvia, Luke and Terry), senior physicist (Dr. P.M. Wu) and research fellow (Dr. Jing Yuan) of Medical Physics and Research Department of Hong Kong Sanatorium & Hospital for all the statistical advice, mentorship and leading their sympathetic ears.

Mr. Wyman Li and Hong Kong Sanatorium and Hospital have provided support on my PhD research funding, for which I am greatly thankful.

Last but not least, I would like to thank my parents, husband and our lovely Vanilla for enduring a stressed out student.

TABLE OF CONTENTS

LISTS OF FIGURES

LISTS OF TABLES

LIST OF ABBREVIATIONS

ADC	Apparent diffusion coefficient
DWI	Diffusion Weighted Imaging
DTI	Diffusion Tensor Imaging
D	True diffusivity
*D**	Pseudo-diffusion coefficient
EPI	Echo-Planer Imaging
f	perfusion fraction
FA	Fractional anisotropy
FFT	Fast Fourier Transformation
HASTE	Half Fourier Acquisition Single Shot Turbo Spin Echo
IVIM	Intra-Voxel Incoherent Motion
MD	Mean diffusivity
NGD	Number of Gradient Directions
NSA	Number of Signal Averages
RD	Radial diffusivity
ROI	Region Of Interest
SD	Standard Deviation
SNR	Signal to Noise Ratio
STE	Scan Time Equivalency
TE	Echo Time
TR	Repetition Time

CHAPTER 1

LIVER PHYSIOLOGY AND MRI PRINCIPLES

1.1 LIVER FUNCTION AND PHYSIOLOGY

The liver is a triangularly shaped versatile organ, which is located in the right hypochondriac and epigastric region. Liver functions include metabolic regulation (e.g. glucose concentration level regulation, and lipid and lipoprotein metabolism) [1], waste product removal, vitamin and mineral storage, and drug inactivation [1]. It is also responsible for hematological regulation and production of bile [2]. Based on its superficial features, it can be subdivided into to right, left, quadrate and caudate lobe. The right and left liver lobe is separated by the falciform ligament, and the caudate and the left liver lobe is separated by the ligamentum venosum [3,4]. Around 25 - 35% of the blood reaches the liver from the hepatic artery [5–7]. The remaining blood comes from the hepatic portal vein, which sources from the oesophagus, stomach, small intestine and the large intestine and spleen. Eventually, the blood returns to the system circulation through the hepatic vein, which joins the inferior vena cava [2].

Liver cells can be generalized as parenchymal cells and non-parenchymal cells. The majority of the liver cells are parenchymal cells, known as hepatocytes. Examples of non-parenchymal cells include biliary epithelium cells, Kupffer cells, stellate cells and sinusoidal endothelial cells [4,8]. These non-parenchymal cells are specialized for different functions, for example, stellate cells play a significant role in regeneration, hepatic fibrogenesis and the development of cirrhosis [8–12].

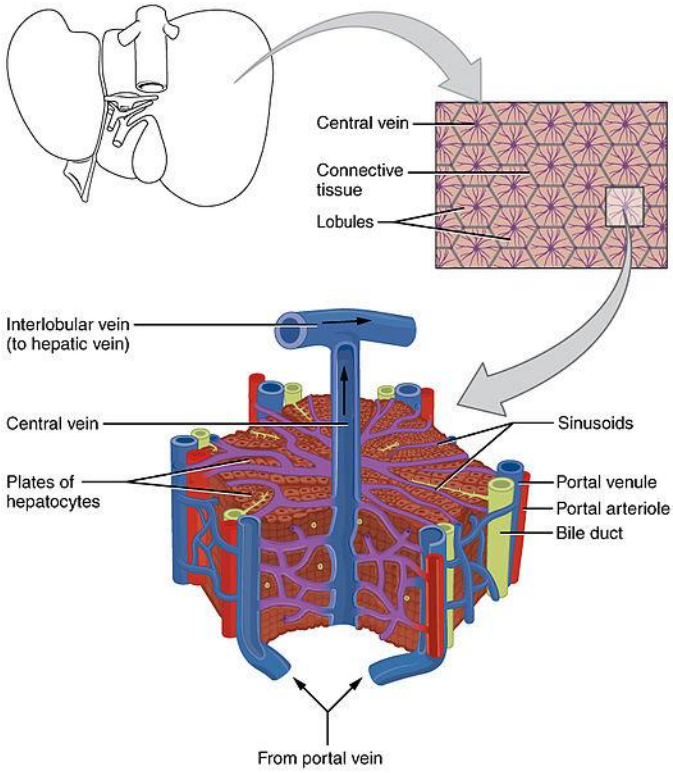

Figure 1.1: *The organization of hepatic lobules (OpenStax College 2015)*[1].

As illustrated in **Figure 1.1**, hepatocytes are organized as a network of one cell thick plates, which are separated by short microvilli [2]. These plates are arranged radially around the central vein to form hexagonal liver lobules. The network of liver lobules is referred to as the hepatic parenchyma, the functional unit of the liver [13]. The hepatic arteries, hepatic portal veins, and the bile ducts can be found at each of the six "corners" of a lobule [14]. Although the anatomical liver structure is quite regularly arranged, heterogeneous functionality

[1] "Download for free at http://cnx.org/contents/14fb4ad7-39a1-4eee-ab6e-3ef2482e3e22@6.27."

has been suggested [15]. An alternative zonation system termed "hepatic acinus" is thus often used in the literature for better characterization of hepatocytes using three sub-divided zones (**Figure 1.2**). The periportal zone I is located nearest to the vascular supply, zone III is located nearest to the central vein, and the transition zone II is sandwiched between zones I and III. Well oxygenated blood first flows through the periportal zone I and eventually through the centrilobular zone III to reach the central vein, thus resulting in the poorest oxygenation in zone III [16]. It is also worth noting that zone III hepatocytes contain a higher level of drug metabolizing enzymes [4]. As such, the function of hepatocytes in zone I is mainly specialized for oxidative liver functions while hepatocytes in zone III are mainly specialized for glycolysis, lipogenesis and drug detoxification (**Table 1.1**).

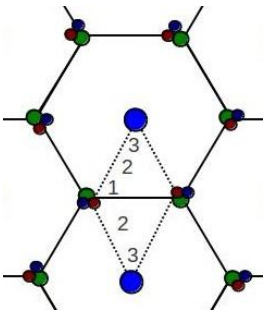

Figure 1.2: *Sketch of the liver acinus. The area of a liver acinus is denoted using dotted lines while the hexagonal lobule is defined by solid lines. The central vein, bile duct, portal venule and portal arteriole were indicated using light blue, green, blue and red circles. The periportal, transition and centrilobular zones are denoted as 1, 2 and 3. Not all the hepatic processes completely follows the zonation. Thus, the periportal, transition and centrilobular zones only represent the functional gradient of the hepatocytes.*

Table 1.1: *Predominant functions of parenchymal cells of the liver at periportal and centrilobular zones based on the distribution of enzymes, translocators, cellular structures or cell densities. (Tabulated from Jungermann and Kietzmann, 1996)*

Periportal (Zone 1)	**Centrilobular (Zone 3)**
Glucose release	Glucose uptake
Oxidative energy metabolism	Glutamine formation
Urea formation	Xenobiotic metabolism
Protective metabolism	Plasma protein synthesis
Plasma protein synthesis	
Cholesterol synthesis	
Bilirubin formation	

Among all types of liver diseases, research related to hepatitis (hepatitis C and hepatitis B viral infection) and fatty liver disease has been widely conducted due to their high prevalence (20-40% for non-alcoholic fatty liver disease in North America [17]). Furthermore, hepatitis C virus infection and fatty liver disease have been associated with hepatic fibrosis, cirrhosis, portal hypertension and hepatocellular carcinoma (HCC) [7,18]. About 20-30% of patients with hepatitis C progress into cirrhosis within a 20-year duration [18,19]. About 25% of non-alcoholic fatty liver patients progressed into fibrosis and cirrhosis [19]. Additionally, patients with both fatty liver and hepatitis C have a higher chance of developing into cirrhosis [20,21].

In the past decades, excessive alcohol consumption has been identified as the major cause of fatty liver. However, it was later revealed that other factors, such as obesity, diabetes, hyperlipidemia and family history of certain diseases (e.g. steatohepatitis and cryptogenic cirrhosis), also may be associated with the

elevated risk of developing fatty liver disease [21,22]. Although fatty liver disease is often clinically classified into alcoholic fatty liver disease and non-alcoholic fatty liver disease, they are difficult to identify based on the morphological grounds alone [23]. It is because both types of fatty liver disease often present with a very similar spectrum of liver abnormality such as steatosis, steatohepatitis and fibrosis [1,21,23–25]. Nevertheless, both types of fatty liver disease usually begin with steatosis, the process of infiltrating fat droplets in the hepatocytes. When steatosis of the liver exceeds 5% of the total liver weight, it is clinically classified as fatty liver disease. Furthermore, fatty liver disease is speculated to be related to alcoholic, obese, diabetic and malnutrition status [23]. Hepatic steatosis usually originates in the centrilobular zone 3 [23]. More specifically, the presence of fatty acids in hepatocytes induces hepatic injury due to elevated oxidative stress [26]. In response to the hepatic injuries, inflammation and activation of hepatic stellate cells are often observed. One of the most prominent effects of hepatic stellate cell activation includes synthesis of extracellular matrix [26]. Despite the rare incidence of steatohepatitis, steatosis may also develop into steatohepatitis and fibrosis if the cause of steatosis persists [27]. In extreme cases, the development of hepatic steatosis can lead to the development of fibrosis and irreversible chronic cirrhosis, owing to the accumulation of collagen in the extracellular space or scar tissue in the liver [26,27]. In addition to the enlarged hepatocytes due to steatosis [14], the progressive increase in collagen alters the shape of the liver lobules [1].

Disruption in the micro-circulatory blood flow and portal hypertension, therefore, result [14,26]. Moreover, the reported highest 5-year cumulative risks of developing HCC in patients with cirrhosis, though the reported risk varies with the underlying conditions, is quite high (17% for hepatitis C viral cirrhosis in the Western countries, 10% for hepatitis B viral cirrhosis in the West, 8-12% for alcoholic cirrhosis, and 4% for biliary cirrhosis) [28]. This epidemiologic data suggests a possible underlying relationship between steatosis, hepatitis, cirrhosis and liver cancer.

With the improvement in lifestyle, the incidence of obesity and, hence, non-alcoholic fatty liver disease drastically increased in the US [19,29]. As discussed above, the incidence of steatosis, hepatitis, cirrhosis and liver cancer are often correlated. Early detection of liver disease at a reversible stage such as fatty liver is, therefore, important. Although the current gold standard of reference based on biopsy and histological evaluation has a high sensitivity and specificity (for example, sensitivity and specificity in diagnosing non-alcoholic steatohepatitis are up to 88 % and 89 %, respectively, using liver biopsy [30]), it is risky and erratic due to sampling error and inter-observer variation [19,30,31]. Thus, monitoring of treatment response and disease progression with only biopsy specimens is less preferable since repetition of liver biopsy is needed. In addition to biopsy, liver disease diagnosis using surrogate markers, although exhibiting less discriminating values, are often used for screening purposes. For example, elevation of serum albumin may be observed in both fatty liver and HCC.

Another example is the use of the aspartate aminotransferase (AST) to alanine aminotransferase (ALT) ratio for diagnosing liver disease. Often, these liver-specific transaminases are released into the blood stream in response to liver cell damage. Depending on the type of liver disease, the magnitude of the AST/ALT ratio may vary. And, this change is often subject specific with respect to referencing normal liver function. Reliable liver disease staging with the use of surrogate markers alone is continually under investigation [31,32]. Nevertheless, liver disease diagnosis with blood-based surrogate markers suffers from lack of spatial specificity. The American College of Radiology (ACR) has developed a Liver Radiological evaluation (Li-RADS) system for systemic interpretation and reporting of computed tomography and MR examinations of patients with high risk of developing HCC [33]. However, how the Li-RADS system links or correlates to surrogate measures is still a matter of debate. Thus, the need for quantitative liver diagnosis and long-term treatment monitoring, in a non-invasive fashion using MRI, is evident.

1.2 DIFFUSION WEIGHTED IMAGING OF THE LIVER

Based on Einstein's formulation of molecular diffusion, the probability distribution of the displacement of water molecules, at a particular time, can be assumed Gaussian [34]. The process of water molecule migration can be

expressed in mathematical terms using the diffusion coefficient (D). Quantification of water diffusion can easily be done with MRI, by applying a pair of diffusion sensitizing gradients, consisting of a dephasing and rephasing gradient with the same duration and gradient strength (**Figure. 1.3**). By applying the dephasing gradient, a phase shift is introduced (in the clockwise direction, for example) and MR signal reduction results. The application of the rephasing gradient then leads to another phase shift in the opposite direction which in principle compensates the effect of the dephasing gradient. Thus, no change in MR signal should be expected in the case of stationary spins. On the other hand, mobile spins will experience a different amount of phase shift in the rephasing gradient, compared to the dephasing gradient. Signal attenuation should, therefore, be expected. Additionally, the sensitivity of the signal attenuation (i.e. diffusion weighting) can be adjusted by varying the duration or the strength the diffusion sensitive gradient pair, and is often termed the magnitude of diffusion weighting, or b-value.

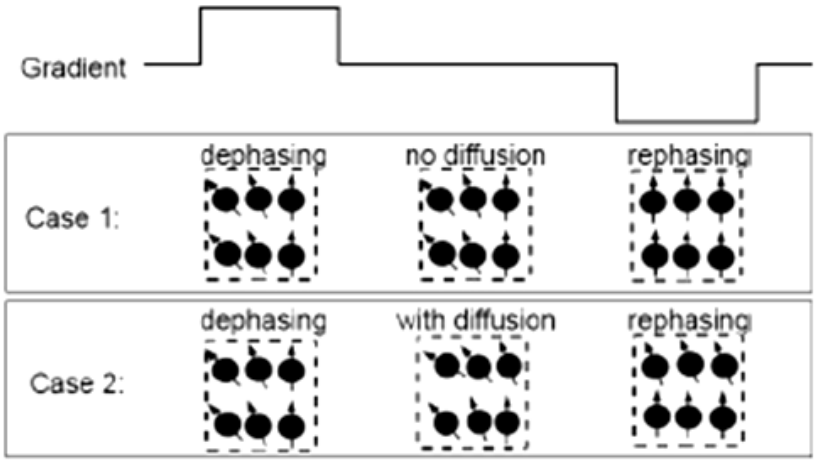

Figure 1.3: *The gradient pulse pair consists of a dephasing gradient and a rephrasing gradient. The rephrasing gradient undoes the effect of the dephasing gradient. For the case of no diffusion (case 1), no change in the spin orientation should should occur between the two gradient pulses.. For simplicity, let's assume the diffusion process is a 1D problem where the first row of the spins moved to the right. The rephrasing gradient thus fails to realign all spins. The signal in case 1 is then stronger than that in case 2.*

An estimate of D can be obtained using the slope of the log of signal attenuation as a function of b-value. The simplest way to calculate D requires the signal attenuation measurements using two sets of b-values. The signal measured at b=0s/mm^2 (S_0) has no diffusion weighting and as a result a T2-weighted image is obtained. On the other hand, diffusion weighted signal (S) can be obtained using a non-zero b-value. The D calculated from DWI is usually replaced by apparent diffusion coefficient (ADC) since diffusion processes in biological

tissues are restricted by the cellular structure. The ADC can be calculated according to **Equation [1.1]** where the signal attenuation due to the diffusion weighted gradient pair can be expressed using

$$\frac{S}{S_0} = exp\left(-b \cdot ADC\right) \quad \textbf{[1.1]}$$

The potential clinical usefulness of DWI in liver disease diagnosis has been suggested by many researchers [35–40]. As discussed in the previous section, structural change in diseased liver parenchyma can be probed through a measure such as the apparent diffusion coefficient (ADC), which shows a different value in diseased liver parenchyma comparing to the healthy liver parenchyma [41,42]. For example, lower ADC values have been reported in patients with liver fibrosis compared to healthy volunteers [41,43]. Also, the potential usefulness of DWI in treatment response monitoring has been illustrated based on its ability to detect structural change in liver parenchyma after internal radiotherapy [36] and conformal radiotherapy [37]. Both groups reported an increase in ADC after the use of radiation, for which tumor lysis, loss of cell membrane integrity and increase in extracellular space are thought to be the cause. Eccles *et al.* further concluded that the observed change in ADC value in irradiated normal liver tissue was a result of epithelial cell death and subsequent radiation-induced inflammatory response [37].

1.3 INTRAVOXEL INCOHERENT MOTION IN THE LIVER

Although liver DWI is valuable, the reported ADC value in previous studies were shown to vary according to the choice of b-value [44]. The source of this apparent discrepancy was the fact that routine DWI is derived based on a monoexponential signal attenuation, which was later reported to be inaccurate *in vivo* [45,46]. In fact, the observed non-monoexponential signal attenuation suggests that the monoexponential model provides an incomplete description of the diffusion process [47]. Various mathematic models such as intravoxel incoherent motion (IVIM) [48], stretched exponential [49] and kurtosis models [50] have, therefore, been proposed for better quantitation of the diffusion process. Unfortunately, the calculated metrics from most non-monoexponential models, except IVIM, are lacking of a physiologic basis [47]. Research based on the IVIM technique is, therefore, most popular.

The original IVIM model was developed by Le Bihan et al. in the 1980s to separate the microcirculatory perfusion and true diffusion effect using a relatively straightforward 2 compartment model [51]. Within any biological tissues, a volume fraction of water motion is thought to correspond to the incoherent water motion in the capillary network. This water motion is related to the microvascular perfusion and is referred as pseudodiffusion (D*). The volume fraction is referred to as the perfusion fraction (f), which is related to the interstitial water diffusion. Meanwhile, intercellular water diffusion of the same biological tissue contributes

to the remaining volume fraction of water motion (i.e. this volume fraction corresponds to 1-f). This water motion is related to the structure of the tissue and is referred as the true diffusion (D). These parameters can be estimated by solving **Equation [1.2]** using nonlinear curve fitting. Thus, IVIM allows quantification of microvascular perfusion and true diffusion without intravenous injection of an MR contrast agent.

$$S/S_0 = (1-f)e^{-bD} + fe^{-b(D+D^*)} \quad \textbf{[1.2]}$$

Previous studies have shown the potential usefulness of IVIM in diagnosing liver diseases [39,45]. The ability to differentiate between cirrhosis, haemangioma, hepatic cellular carcinoma (HCC) and cysts has been shown to be successful using IVIM [52]. Moreover, improved sensitivity and specificity in liver fibrosis and cirrhosis detection results when using both IVIM and contrast-enhanced MRI [39]. Unfortunately, reliably estimating IVIM metrics has proven to be difficult [53]. ROI-based analysis is encouraged to improve the reliability of the estimated metrics [47]. Furthermore, repeated MR signal measurements with various b-values is often necessary to obtain more reliable IVIM metrics, which unfortunately leads to a prolonged scan time. In addition, the estimated IVIM metrics are subject to sample size [53], the choice of b-value [54,55], fitting strategy [56] and motion compensation scheme [57–59]. For example, b-values less than 100 s/mm^2 are noted to probe the perfusion region while b-values larger than 100 s/mm^2 are labeled to probe the diffusion region [47]. It should be noted,

however, both region have contribution to each other. Thus, to adequately model IVIM b-values from both perfusion and diffusion region need to be selected.

1.4 PRINCIPLE OF DIFFUSION TENSOR IMAGING

Although the results from DWI and IVIM in liver disease diagnosis seem promising, both techniques ignore the fact that diffusion is a three dimensional process. More importantly, the usefulness of diffusion directionality in tissue characterization has been illustrated using *in vivo* diffusion tensor imaging (DTI) in various regions such as brain [60], muscles [61], kidney [62] and prostate [63]. DTI, as opposed to DWI, involves the reconstruction of the diffusion tensor (DT), which is a better mathematical description of the spatial orientation of the diffusion process. Instead of using a scalar value D in **Equation [1.1]**, it is substituted by a 3x3 rank 2 tensor. Since the DT matrix is symmetric (i.e. $D_{ij} = D_{ji}$), a minimum of 7 signal measurements (6 non-coplanar diffusion weighted measurements and 1 measurement for S_0) are required for the tensor reconstruction [64]. Furthermore, the benefit of tensors is they are rotationally invariant. In the case of DWI, the signal is the projection of the true diffusion vector onto the diffusion encoding gradient. As the direction of diffusion process changes according to the orientation of the tissue of interest, the intensity of DWI signal would change as a result. The estimated DT metrics, on the other hand, are not affect by the tissue orientation. Thus, the repeatability of DTI should,

theoretically, be superior to that of DWI [65,66]. More importantly, not all metastatic lesions can be differentiated using DWI alone [67]. Additional parameters or an alternate methods in water diffusivity estimation are, therefore, needed. The performance of DTI does not only provide diffusivity in a three dimensional sense using eigenvalues (λ_1, λ_2 and λ_3) and eigenvectors (v_1, v_2, v_3), it also allows the determination of fractional anisotropy (FA), a scalar that is related to the shape of tissue structures. When water is diffusing freely within the target tissue (i.e. isotropic water diffusion), FA will equal to zero. When FA goes towards one, water diffusion is highly restricted in 2 of 3 directions. In this case, water diffusion is said to have anisotropic geometry. Other DT scalars such as mean diffusivity (MD, mean of eigenvalues) and radial diffusivity (RD, mean of λ_2 and λ_3, where $\lambda_1 > \lambda_2, \lambda_3$) are also useful in monitoring the structural change of a tissue of interest. For example, RD and the principle eigenvalue (λ_1) have been related to white matter pathology in the brain [68].

Since DTI has been developed and successfully applied in the study of human brain for decades [69], a basic DTI sequence is readily available on most clinical scanners. With the improvement in technology, increase in signal to noise ratio (SNR) and faster image acquisition have been developed. This opens up an opportunity in applying DTI in the liver, where lower SNR and motion are typically of concern.

To date, there are only a limited number of publications in liver DTI. Taouli et al. reported no significant differences in ADC measured along x, y and z

orientations [40]. It has been concluded that liver FA measurement is not useful because the liver has a near isotropic diffusion [40]. Also, no significant differences in ADC measurement along the x, y and z orientations have been found within cirrhotic liver tissues [41]. However, non-zero FA values have been reported in animal [70] and human liver [42,71] studies. Erturk et al. showed significantly different FA between cysts, hemangiomas and metastases within human liver, suggesting the potential usefulness of liver FA [42]. Nevertheless, the results from DTI and DWI can be influenced by motion [72], choice of b-value [73], SNR [74] and the number of diffusion gradients [75].

1.5 DEALING WITH LIVER MOTION

All three techniques (DWI, IVIM and DTI) discussed previously are susceptible to motion, and thus produce artifacts. This is especially critical for upper abdominal diffusion imaging since cardiac-induced artifact, and breathing-induced artifact are pronounced [47]. Motion compensation is often performed using one of two approaches: real-time during image acquisition [57,58] or off-line image registration [59,76]. Real-time approaches include multiple breath-holding, navigator echo sequence, cardiac triggering and respiratory triggering. However, all of these techniques assume no change in the shape of the target organ as long as the images are acquired at the same phase of the cardiac and respiratory cycles. When compared with free-breathing approaches, improvement

in the reproducibility of ADC [77] and IVIM metrics [55] have been reported using respiratory triggering. However, respiratory techniques probe breathing motion based on thoracic or abdominal wall motion (i.e. using positional-based triggering) using a respiratory bellows. The respiratory expansion during the respiratory cycle is detected by the respiratory bellows, which is secured around either the thoracic or the abdominal region of the subject. Such technique often fails in a shallow breather or in a subject with a mix of thoracic and abdominal breathing habits. A navigator echo sequence, on the other hand, involves probing the diaphragm motion with a low resolution 1D pattern. This technique involves a more direct respiratory motion monitoring and should give a better estimation of respiratory motion. In the work of Nasu et al., however, a significantly larger ADC value was observed using a navigator compared to a free breathing approach, while no difference in ADC was observed between respiratory triggering and a free-breathing technique [78]. They concluded that the small non-linear motion of the liver, known as pseudo-hepatic anisotropy, leads to a locally elevated ADC value.

Although linear image registration performs well for so called rigid bodies such as brain [79], it is not appropriate for use in deformable organs. Non-linear image registration to correct for change in liver shape during respiration has been applied [59]. However, motion induced diffusion weighted signal error is composed of two components: magnitude and phase, where phase error cannot be corrected through image registration [57]. Although the modified IVIM model

has been performed to correct the motion induced phase error, even the author admitted that their modified IVIM model is hard to validate without a gold standard. [57]. Since there is no gold standard to evaluate whether image registration has been done properly, the potential error can be hard to identify. More importantly, non-linear image registration approaches involved the modification of the diffusion weighted raw image data. Additional caution should be taken when using linear and non-linear image registration approaches.

Both real-time and offline image registration approaches have their advantages and disadvantages. At this moment, the best way to deal with hepatic motion correction is still debatable. Nevertheless, with further improvement in parallel imaging, coil design and faster imaging sequences, the effect of motion error on quantitative DWI will become minimized.

CHAPTER 2

HYPOTHESES and OBJECTIVES

2.1 HYPOTHESES

Gross pathological and histopathological studies have shown that liver structure changes in fibrosis, cirrhosis and fatty liver [80]. In fact, liver tissue structural and perfusion changes, in the presence of liver disease, are often closely related. For example, enlarged fatty hepatocytes due to increasing fat content may lead to restricted extracellular diffusivity, and the presence of fat droplets may also lead to restricted intracellular water diffusion [81]. Hepatic injuries such as stenosis are often reversible and progress into non-reversible liver disease such as HCC and cirrhosis [20,82]. To assess liver disease, biopsy with subsequent histological analysis is the current standard of care. This approach is not completely risk free and is often problematic due to sampling error and inter-observer differences [20,40]. A better, non-invasive technique to diagnose and monitor liver disease is unquestionably needed. Even more importantly an approach to identify early stage liver disease is needed.

Liver micro-structural tissue properties can be assessed using diffusion weighted imaging (DWI) which is sensitive to microcellular water diffusivity [64]. The DWI approach has shown clear clinical utility when assessing liver disease [35–40]. Although perfusion in the liver can be assessed *in vivo* using dynamic contrast enhanced MRI (dceMRI), perfusion methods are challenging since their use requires *a priori* knowledge of both arterial and portal vein input functions (i.e. the liver has dual inputs making the modeling a challenge). A model-free

perfusion approach has been suggested as a useful complement in diagnosing cirrhosis, however the analysis is not completely model free [39].

A non-invasive alternative to dceMRI modeling of injected tracers is intravoxel incoherent motion (IVIM). Using this approach, microvascular perfusion, and true cellular diffusion effects can be quantified simultaneously without the need for an intravenous contrast agent. Previous IVIM studies have shown clinical utility in diagnosing diffuse liver disease while assuming isotropic diffusion in the liver [83]. However, a recent study has revealed asymmetric lobules in the human liver [80], suggesting liver diffusion is only close to isotropic. Furthermore, motion induced liver signal modulation, due to the pseudo-hepatic anisotropy artifact, has been shown to be directional [57]. In fact, the importance of directionality has been revealed in a number of tissues such as brain, muscle and kidney through the use of diffusion tensor imaging (DTI). In particular, DT metrics such as fractional anisotropy (FA) and the tensor eigenvalues are quantifiable mathematical quantities relating the shapes of cellular structures. Recently, combined IVIM and DTI has been successfully performed in kidney [62] and muscles [84]. However, the directional dependency of both the liver perfusion and diffusion effects has not previously been studied. The goal of this work was to first evaluate the effect of the pseudo-hepatic anisotropy artifact on the quality of DT and IVIM metrics. Further, a possible solution in minimizing the effect of pseudo-hepatic anisotropy was introduced through the use of combined IVIM and DTI assessment. Thus, the hypotheses of the work

detailed in this thesis were (1) the pseudo-hepatic anisotropy artifact leads to a change in DT and IVIM metrics; (2) this pseudo-hepatic anisotropy artifact can be characterized using multiple non-coplanar gradient encoding directions; and (3) the modification of the current IVIM model to incorporate directional information in the liver is a feasible procedure.

2.2 METHODS

Healthy volunteers for the studies presented in this thesis were recruited through the Medical Physics and Research Department (Hong Kong Sanatorium & Hospital, Hong Kong SAR), and the Imaging Research Center (St. Joseph's Healthcare, Hamilton, Ontario). Local research ethics board approval was granted for studies at both sites. Healthy staff members working at Hong Kong Sanatorium & Hospital were recruited in most of the studies (Chapter 3-5). Although an unusual approach (i.e. not public volunteers) this group was chosen since blood tests and hepatitis B vaccinations are mandatory on the first day of work at the Hong Kong Sanatorium & Hospital. Thus, the health status of each volunteer was reliably known. For the feasibility study investigating the simultaneous use of IVIM and DTI (Chapter 6), younger healthy volunteers at St. Joseph's healthcare were recruited, since extra long breath-holding (in total 35s per breath-hold, repeated 45 times) was required and this was easier to achieve using a younger aged population.

In theory, the rotational invariance of DTI provides quantitative measurements of tissue diffusion *in vivo*, with better precision than DWI [65,66]. Although non-zero FA has been reported in the liver [70], isotropic liver diffusion has been assumed in most body imaging studies [83]. The initial work in this thesis was done to assess the reproducibility of liver DT metrics (Chapter 3). This was carried out to evaluate the effect of SNR and number of gradient directions (NGD) on the calculated DT metrics. To eliminate any potential biasing factor, each subject was asked to participate in a total of three sessions (1.5 hours/session) within a two week timeframe.

Based on the work of Murphy *et al.* liver DWI signal modulation is related to liver motion [57]. More specifically, signal changes were identified as the result of non-linear motion, which led to the pseudo-hepatic anisotropy artifact [78]. As the DTI sequence is very sensitive to motion, and the abdomen is affected by complex cycles of both cardiac and respiratory movements, it is necessary to evaluate the relationship between DT metrics and liver microstructure throughout the course of these physiological cycles. The effect of bulk cardiac and respiratory motion on DT metrics was thus studied on a regional (anatomically) basis using two separate experiments each focussing on only one source of motion contamination (Chapter 4). The effect of respiratory motion was first evaluated by comparing the DT metrics in the right liver lobe between free breathing and breath-holding scans. The cardiac effect was studied by comparing DT metrics, of the left and right liver, acquired during multiple phases of the cardiac cycle.

Bulk cardiac and respiratory motions were compensated for simultaneously using cardiac triggering and multiple breath-holds. The residual non-linear liver motion was hypothesized to lead to pseudo-hepatic anisotropy artifact, predominantly in the left liver lobe. As the amount of liver deformation changes according to the phase of the cardiac cycle, it was hypothesized that DT metrics would reflect this cyclic variation.

Although motion correction for liver IVIM using non-rigid image registration was recently proposed [57], validation of non-linear motion correction was challenging. It is generally assumed in Chapter 5 that liver motion can be generalized into linear displacement, which can be minimized by linearly registering to a baseline image, and non-linear compression due to force, which is hypothesized to be minimized using multiple diffusion encoding gradients. Hypothetically, the pseudo-hepatic anisotropic artifact (due to compression) and the perfusion effect would lead to an intra-voxel motion of a similar magnitude. Thus, the pseudo-hepatic anisotropic artifact would be mistaken as flow signal and give rise to motion contaminated liver parenchyma. In this case, the combination of the IVIM effect and pseudo-hepatic anisotropic artifact can be separated from the true water diffusivity using the IVIM model. This was verified in the first part of chapter 5 by applying a Gaussian Mixture model on the voxel-wise IVIM metrics and the voxel-wise goodness-of-fit. In the presence of the pseudo-hepatic anisotropy artifact, three clusters of voxels (each mainly located in the left liver lobe, right liver lobe and vessels) within the whole liver were

identified (Chapter 5). A test was then performed to correlate the resultant clusters with their geometric location based on their mean IVIM metrics. The later part of Chapter 5 mainly focuses on the minimization of the pseudo-hepatic anisotropy artifact with the aid of multiple diffusion encoding gradients. Since non-linear liver motion is directional [57], it can potentially be minimized by averaging over multiple non-coplanar gradient directions.

Lastly, combined IVIM and DTI analysis has recently been applied in human kidney [62] and skeletal muscles [84], showing the combination of these two methods is feasible. The rationale for combining both is that the additional metrics generated from the combined analysis may gain additional benefit in the characterization of liver parenchyma, especially when diseased or in early stages of disease. Two approaches (IVIM-DTI and DTI-IVIM) in combining IVIM and DTI analysis in healthy human liver were, first, proposed and tested in Chapter 6. Both approaches were then compared with the conventional IVIM approach to look for the potential benefit in liver tissue characterization. Finally, the best technique was then decided based on the comparison between the results from IVIM-DTI and DTI-IVIM through error analysis.

CHAPTER 3

REPEATABILITY OF DT METRICS IN HEALTHY LIVER

Intra-session and Inter-session repeatability of Diffusion Tensor Metrics in Healthy Human Livers

Oi Lei Wong, MSc, Gladys Goh Lo, MD., Wing Wa Li, MSc and Michael D. Noseworthy, Ph.D., P.Eng

3.1 CONTEXT OF THE PAPER

Previous diffusion weighted imaging (DWI) studies have quantified liver diffusion using 1 or 3 gradient directions. Recently, there has been growing interest in applying diffusion tensor imaging (DTI) for differentiating liver disease [42]. However, poor DTI consistency will reduce the confidence in disease progress assessment, reducing clinical significance. More importantly, DT metrics have been shown to be related to the choice of number of diffusion gradient directions [75] and SNR [85]. However, DTI repeatability studied are often based on human brain [74] and muscle studies [86]. Repeatability of liver DTI metrics is absent in the literature and thus needs evaluation. In this study, we have determined intra-session and inter-session repeatability of human liver DT metrics. Briefly, the repeatability of DT metrics is improved with elevated SNR.

However, no relation between the number of diffusion encoding gradients and repeatability of DT metrics was observed.

3.2 DECLARATION STATEMENT

Oi Lei Wong as principle author wrote the article, performed analysis and created figures and tables as appropriate. Michael D. Noseworthy, as the corresponding author, provided guidance and advice, and performed proofreading/editing and submission of the manuscript for publication. Dr. Thomas Leung and Dr. Gladys Lo provided clinical guidance and commentary. Wing Wah Li provided imaging protocol commentary and performed the MR image acquisition.

This paper has been submitted to the journal, Journal of Computer Assisted Tomography

3.3 PAPER

Intra-session and Inter-session repeatability of Diffusion Tensor (DT) metrics in Healthy Human Liver

Oi Lei Wong, MSc[1,2,3], Thomas Wai Tong Leung, MD[4]., Gladys Goh Lo, MD.[5], Wing Wa Li, MSc[5] and Michael D. Noseworthy, Ph.D., P.Eng.[1,2,6,7†]

[1]Department of Medical Physics and Applied Radiation Science, McMaster University, Hamilton, Ontario, Canada.
[2]Image Research Center, St. Joseph's Healthcare, Hamilton Ontario, Canada.
[3]Medical Physics and Research Department, Hong Kong Sanatorium & Hospital, Hong Kong Special Administrative Region (SAR), China.
[4]Comprehensive Oncology Center, Hong Kong Sanatorium & Hospital, Hong Kong Special Administrative Region (SAR), China.
[5]Intervention and Radiology Department, Hong Kong Sanatorium & Hospital, Hong Kong Special Administrative Region (SAR), China.
[5]School of Biomedical Engineering, McMaster University, Hamilton, Ontario, Canada.
[6]Department of Electrical and Computer Engineering, McMaster University, Hamilton, Ontario, Canada.

***Corresponding Author:**
Dr. Michael D. Noseworthy, Ph.D., P.Eng.
Director, McMaster School of Biomedical Engineering,
Associate Professor, Department of Electrical and Computer Engineering,
McMaster University.
Hamilton, Ontario, Canada.
email: nosewor@mcmaster.ca
voice: +1 1 (905) 925-9140 ext.23727
http://www.ece.mcmaster.ca/~mikenose/web/HOME.html

ABSTRACT:

Purpose: To evaluate the effect of SNR and number of gradient directions on intra- and inter-session repeatability of diffusion tensor (DT) metrics in the healthy human liver.

Materials and Methods: Five healthy volunteers were recruited, and three liver DTI scan sessions were collected using a 1.5T MR scanner over a two-month interval. At each of 3 visits liver diffusion was assessed using a 6 direction DTI scan performed 9 separate times (providing from 1 to 9 NSA). Additionally four combinations of number of signal averages (NSA) and number of gradient directions (NGD) were also acquired (NSA/NGD = 1/30, 3/10, 3/12 and 5/6), maintaining a similar level of acquisition scan time equivalency (STE). ROI-based analysis was performed on whole liver, and a sample of each the right and left liver lobe. Inter-subject variability was determined with the 9 NSA scans while the combined effects of NSA and NGD on inter-subject variability was determined with the 4 STE scans. Inter-subject DT metric variation was evaluated using coefficient of variation (CV) while intra- and inter-session DT metric repeatability was measured using test-retest variability.

Results: Inter-subjection variability was <20%, while intra-session (V_{intra}) and inter-session (V_{inter}) repeatability < 5% and < 10%, respectfully. Inter-session repeatability was not affected by the number of gradient directions used. For all ROIs measured, decreases in $V_{inter}(FA)$, $V_{inter}(\lambda_1)$, $V_{inter}(RD)$ and $V_{inter}(MD)$ were observed with increasing NSA, and hence SNR.

Conclusion: Increased NSA (hence increased SNR) may improve the intra-session and inter-session repeatability. However, repeatability was not influenced by number of gradient diffusion encoding gradients.

KEYWORDS:

MRI, liver, diffusion tensor imaging.

INTRODUCTION:

The potential utility for diffusion weighted imaging (DWI) in diagnosing liver disease has been demonstrated in previous studies [1,2]. The rationale behind this may partly be related to the increased collagen in diseased liver tissue, which reflects a change in the apparent diffusion coefficient (ADC) [1,3]. For example, water diffusion is more restricted in fibrotic liver tissue compared to healthy, which correlates to a reduced liver ADC [1,4]. However, DWI provides limited information and does not provide information on tissue microstructure such as diffusion anisotropy. One variant, diffusion tensor imaging (DTI) allows the quantification of water diffusion anisotropy and has been widely applied in the brain [5]. Recently, application of DTI in the liver for the differentiation of fibrosis, malignancy and hemangioma has shown reasonably good success [3].

DTI metrics are often closely affected by SNR [6], number of diffusion encoding direction [7] and diffusion gradient scheme [8]. To date, DT metric repeatability studies have been done using human brain [9,10,11] and skeletal

muscle [12]. Due to the anatomical differences between these tissues and human liver parenchyma, it is not appropriate to assume liver DT metric repeatability to be equivalent to the previously reported results from other tissues. More importantly, measurement consistency is essential for quality clinical treatment monitoring and treatment outcome evaluation. Hence it is important to verify DT measurement reliability, when using this approach for assessing human liver. We, therefore, proposed to study the intra-session and inter-session repeatability of DT metrics at various SNR levels (modulated by number of signal averages, NSA) and number of diffusion encoding gradient directions (NGD).

MATERIALS AND METHODS:

Patient recruitment and inclusion criteria

Five healthy volunteers (3 male and 2 female, mean age of 32 ± 6 years) were recruited for the study, and informed consent was obtained from each. The study was approved by the Institutional Research Board (Hong Kong Sanatorium & Hospital, Hong Kong SAR, China) prior to this study. A questionnaire was provided to rule out any unsuitable candidates based on the following inclusion criteria: (1) absence from drug and alcohol abuse, (2) no current medication, (3) free from jaundice and systemic disease (such as diabetes, rheumatoid arthritis, systemic lupus erythematosus, sarcoidosis and mixed connective tissue disease) at the time of scan, (4) never treated with chemotherapy (for any type of malignancy, lymphoma and leukemia) and for chronic condition (such as

hypercholesterolaemia or rheumatological complaints) prior to and at the time of scan, (5) biological mother was free from hepatitis C and hepatitis B infection at time of birth, and (6) free from fatty liver at the time of scan. An additional MR session was provided prior to the repeatability study where a 2-point DIXON technique was used to screen out candidates with fatty liver. All volunteers were staff members working at the Hong Kong Sanatorium & Hospital where a liver function blood test and hepatitis B vaccination are mandatory at the beginning of employment. Thus, we believed liver health to be highly reliable.

Data Acquisition

All MR scanning was done at Hong Kong Sanatorium & Hospital (Hong Kong SAR, China) using a 1.5T Siemens MR scanner (Espree, Siemens Medical, Erlenberg, Germany) with subjects in a supine position. Unless otherwise specified, all image acquisition were axially acquired with a single shot dual-spin echo DTI EPI sequence (TE/TR = 86/2200ms; matrix=110×110; NSA=1; FOV=35cm; 8 slices 10mm thick, no gap; b-value = 300s/mm^2; fat saturation (SPAIR) on; partial fast Fourier transformation= 6/8). Respiratory motion compensation was done using respiratory triggering (with a respiratory pillow) at end-expiratory phase. All scans were done using identical prescan values (shim settings, center frequency, and transmit/receive gain values) and geometric prescription.

Each volunteer was asked to participate in 3 scan sessions within a two-week interval. All scanning was performed following at least 4 hours of fasting.

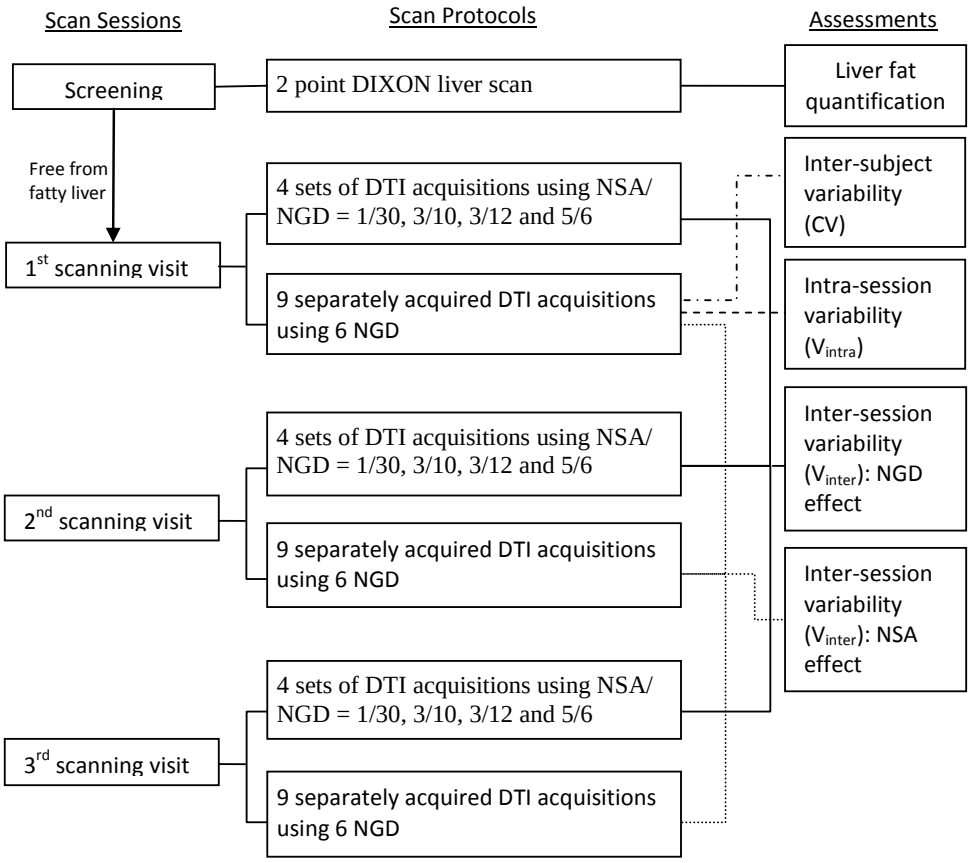

Figure 3.1: *Data collected from each scan visits. Intra-session repeatability and inter-subject variability were calculated using the data from the 1st scanning visit. Inter-session repeatability was calculated using the data from all scanning visits.*

As illustrated in *Figure 3.1*, only the data collected from the first scanning visit was used to evaluate inter-subject variability and intra-session repeatability. All scanning sessions were used to determine inter-session repeatability due to the variation of NGD and NSA.

Inter-subject variability and intra-session repeatability

Eddy current and motion correction were performed on the 9 separately acquired DT images (NSA =1; NGD = 6) from the first scanning visit. Motion

correction was done by linearly registering the images from each DT acquisition to the chronologically first b=0s/mm^2 image. The corrections were done using the McFlirt utility of the FMRIB Software Library (FSL) (FSL 4.1, Oxford Centre for Functional Magnetic Resonance Imaging of the Brain Analysis Group, Oxford, UK) [13]. Afterwards, five separate DTI acquisitions were randomly chosen (out of the 9 separately acquired DTI acquisitions) and this selection process was repeated until 9 combinations of 5 DTI acquisitions were chosen. The image set of each combination was averaged (yielding a mean diffusion weighted signal per diffusion weighted gradient) prior to calculation of the diffusion tensor, resulting in 9 DTI acquisitions each with an effective NSA of 5. DT metrics (i.e. fractional anisotropy (FA), principle eigenvalues (λ_1), radical diffusivity (RD, mean of two eigenvalues λ_2 and λ_3) and mean diffusivity (MD, mean of all three eigenvalues)) were then calculated offline using the FDT plug-in of FSL. The resultant DT metrics were subsequently utilized in the intra-session repeatability and inter-subject variability assessment (described in *Statistical Analysis* below).

Inter-session repeatability: effect of NGD and NSA

The focus of inter-session repeatability included variation of NGD and NSA. To evaluate the effect of variation in NGD to inter-session repeatability, four sets of separately acquired DTI scans were performed with varying NSA/NGD while maintaining the scan time equivalency (STE) (i.e. NSA/ NGD = 1/30, 3/10, 3/12 and 5/6). Eddy current and motion correction were performed using the MCFLIRT utility for each NSA/NGD combination prior to the calculation

of their mean diffusion weighted signal. For each NSA/NGD combination, motion correction was done by linearly registering the DT images to the chronologically first b=0s/mm^2 image. As a result, 4 sets of DT images with effective NSA of 1, 3, 3 and 5, respectively, were obtained for each scanning visit. To evaluate the effect of variation in NSA, each scanning visit also included a set of 9 separately acquired DTI acquisitions (NGD = 6, NSA = 1). Eddy current and motion correction were again performed using the MCFLIRT utility in a similar pipeline to that described previously. The images were then organized into 9 groups in random order to obtain 1, 2, 3, 4, 5, 6, 7, 8 and 9 DTI acquisitions in each group. The DTI acquisitions from each group were averaged prior to the DT metric calculation using the FDT plugin, making an end effective NSA of 1, 2, 3, 4, 5, 6, 7, 8 and 9, respectively. The resultant DT metrics were then used to evaluate the effect of NGD and NSA to inter-session repeatability, respectively, using the method described in the statistical section below.

Statistical Analysis

Circular regions of interest (ROI) (diameter, 10mm; one per region, 1 slice) were selected within the left liver lobe (LL) and right liver lobe (RL). A larger irregular shaped ROI was also selected to cover the whole liver. To avoid the mis-registration error between the diffusion data set and the anatomical image, ROIs were selected on the b-value = 0 s/mm^2 images using anatomical HASTE images as a guide. As such, the error introduced by the mismatch between the HASTE anatomical image and the DWI image set was minimized.

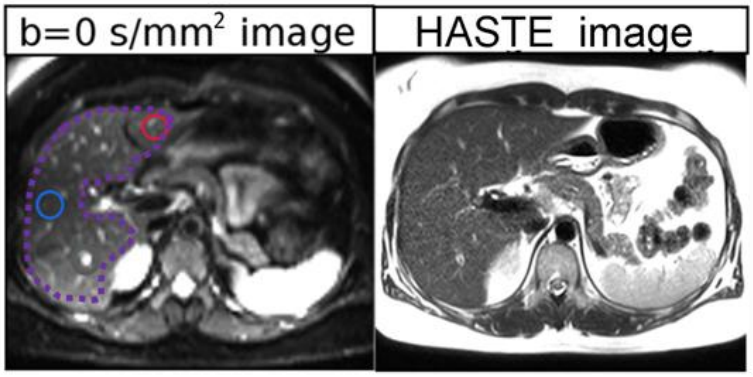

Figure 3.2: *ROI selection on one of the healthy volunteers. ROI of the left liver lobe (red circle), right liver lobe (blue circle) and whole liver (purple dotted line) overlaid on the b-value = 0s/mm^2 image. (E) Anatomical HASTE image of the corresponding slice location.*

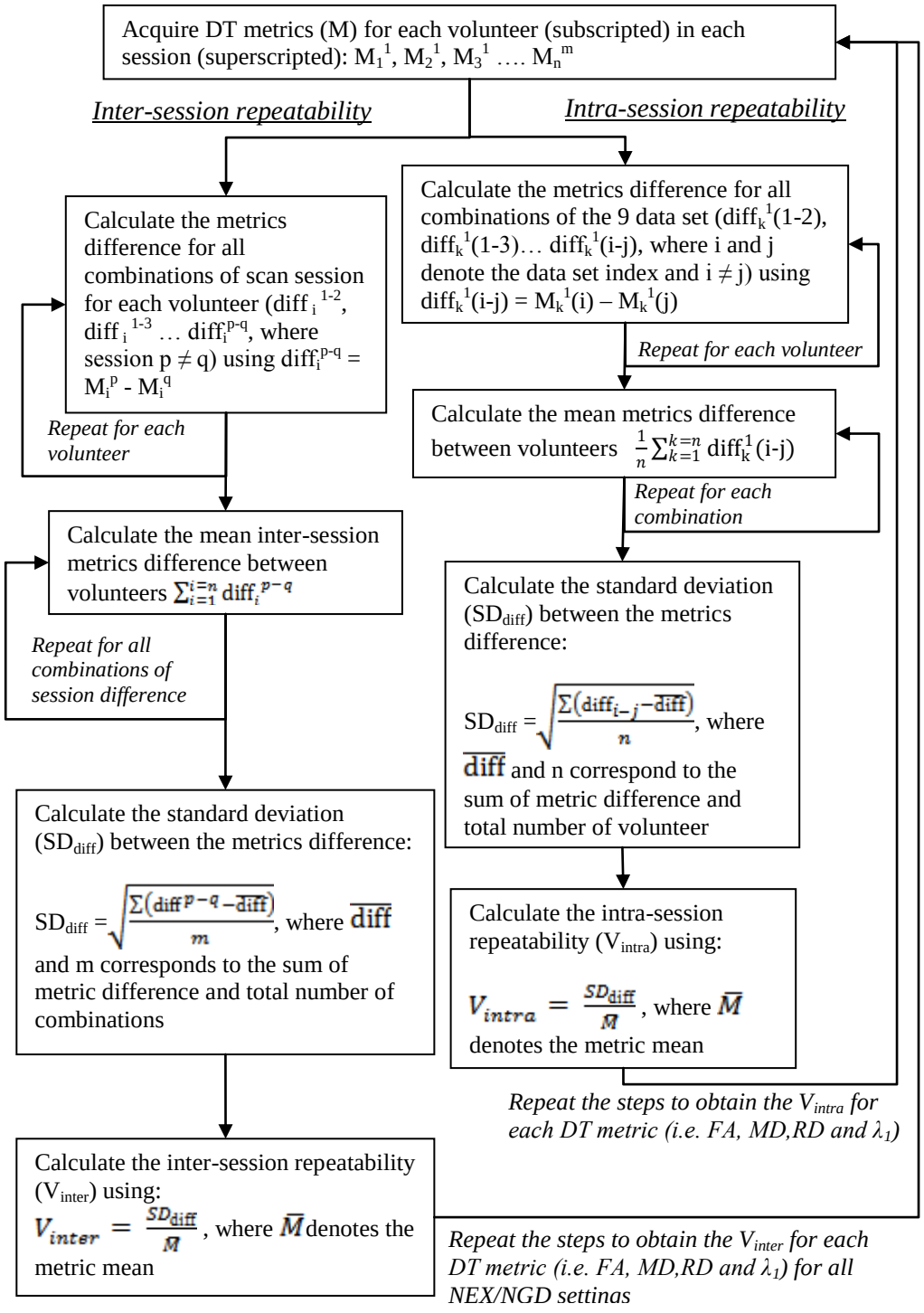

Figure 3.3: *Work flow for inter-session (right) and intra-session (left) repeatability calculations.*

The calculation of inter-session and intra-session repeatability are illustrated in a work flow chart (**Figure 3.3***)*. For intra-session repeatability analysis, FA, MD, RD and λ_1 differences between the 9 DT data sets (i.e. a total of 36 metrics difference for each DT metric) were first obtained for each volunteer using the DTI data set from the first scan session. For each DT metrics, the DT metric differences were then averaged between volunteers. The reported intra-session repeatability (V_{intra}) was defined as percent ratio between the standard deviation of the mean DT metric differences (SD_{diff}) to the mean of the corresponding DT metrics ($\bar{M}$). Inter-subject variation was also evaluated using the coefficient of variation (*CV*):

$CV = \frac{SD}{\bar{M}}$, where SD and ($\bar{M}$) correspond to the standard deviation and the mean of the measured DT metrics obtained from each subject. This was accomplished assuming the inter-subject variation was independent of the scan sessions, NSA and NGD. Therefore, it was done using one of the data sets (6 NGD and effective NSA of 5) from the first sessions. For all choices of ROIs, the mean and standard deviation of each DT metric were calculated for each subject, and the corresponding *CV* obtained.

As illustrated in **Figure 3.3**, inter-session repeatability (V_{inter}) was estimated similarly to V_{intra}. However, the between-session DT metric differences were used. Each inter-session DT metric difference was defined as the mean inter-session DT metric difference between volunteers. V_{inter} was obtained from

the percent ratio between the standard deviation of the entries in the array of DT metric difference and mean of the corresponding DT metrics. Coefficients of variation (*CV*) were also calculated for determining any possible NSA and/or NGD effects on inter-session variability. Lastly, the effect of NSA, NGD and ROI choice were evaluated by applying a Kruskal-Wallis test and Turkey's honest significant difference (HSD) test, when appropriate, on inter-session DT measurement difference and intra-session DT metric test-retest variability.

RESULTS:

Table 3.1: *Inter-subject variability of liver DT metrics using small circular ROI of the left liver lobe (LL), right liver lobe (RL)and large irregular shaped ROI of the whole liver.*

Region of interest (ROI)	FA		λ_1 [x 10^{-3} mm^2/s]		RD [x 10^{-3} mm^2/s]		MD [x 10^{-3} mm^2/s]	
	mean ± SD	CV [%]	mean ± SD	CV [%]	mean ± SD	CV [%]	mean ± SD	CV [%]
Left liver lobe (LL)	0.39 ± 0.07	17	3.56 ± 1.21	34	2.04 ± 0.59	29	2.55 ± 0.79	31
Right liver lobe (RL)	0.38 ± 0.10	26	2.62 ± 0.48	18	1.52 ± 0.24	16	1.89 ± 0.28	15
Whole liver (WL)	0.36 ± 0.07	19	3.46 ± 0.41	12	2.12 ± 0.22	11	2.57 ± 0.26	10

The lowest inter-subject variability was observed using an ROI encompassing the whole liver (*CV* < 20%) (**Table 3.1**). The inter-subject variability of λ_1, RD and MD was greastest in the left liver lobe (*CV* = 34%, 29% and 31%, respectively) compared to the right liver lobe (*CV* = 18%, 16% and 15%, respectively).

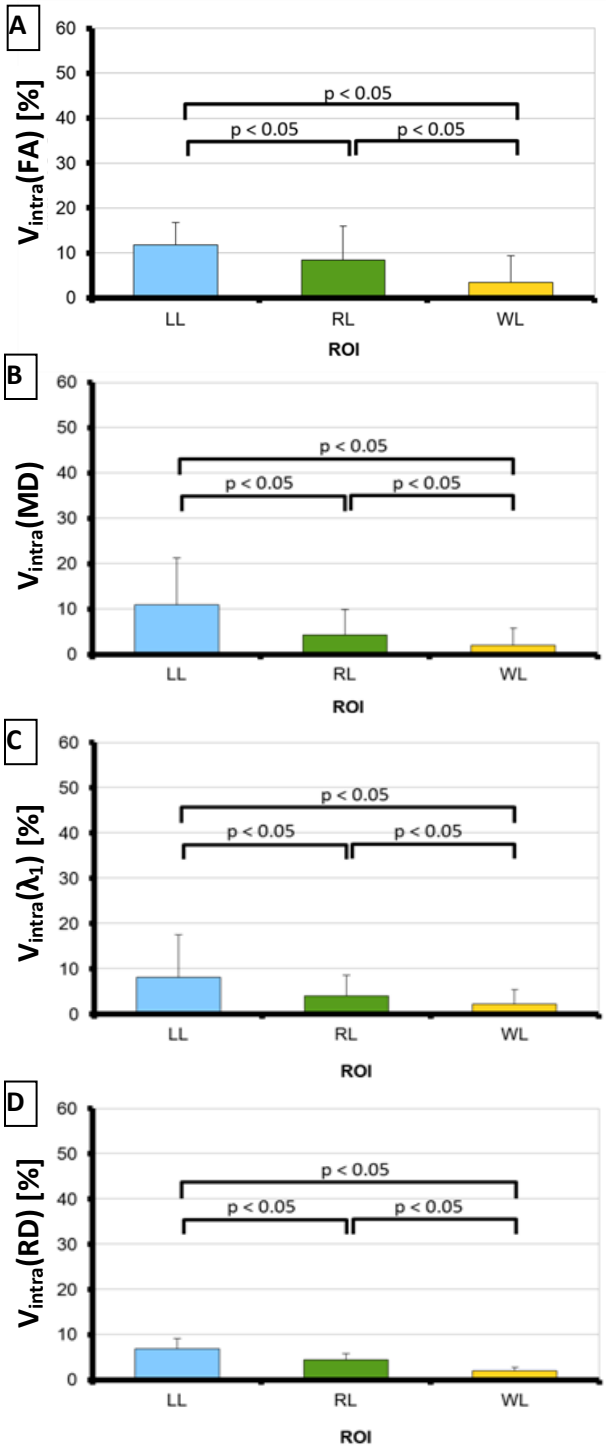

Figure 3.4: *Test-retest variability of intra-session repeated liver DT metric measurement from ROIs of left (LL) and right liver lobes (RL), and whole liver (WL) (Figure 3.2). Values are mean metric ± standard deviation.*

Intra-session repeatability of DT metrics, for calculated DT metrics using either measurement within the right liver lobe or whole liver was always less than 10% (i.e. $V_{intra} < 10\%$) (**Figure 3.4**). The test-retest variability of the left liver lobe (V_{intra} = 8-13%) was larger than that of the right liver lobe (V_{intra} = 4-8%). Significant difference between left liver lobe and whole liver ROI ($p<0.05$), left liver lobe and right liver lobe ($p<0.05$), and between right liver lobe and the whole liver ROI ($p<0.05$) were found based on Tukey's HSD test.

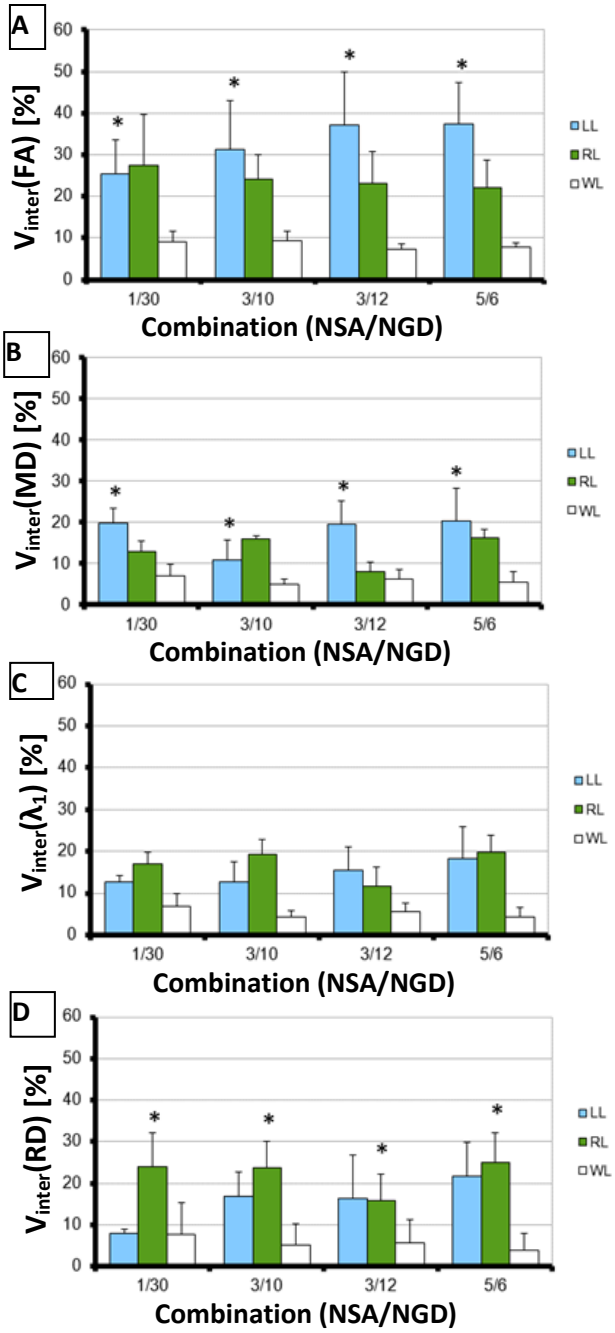

Figure 3.5: *Inter-session repeatability of the 4 NSA/NGD combinations in the ROI from the left liver lobe (LL), right liver lobe (RL) and whole liver (WL) (Figure 3.2). The mean and standard deviation of the (A) V(FA), (B) V(λ_1), (C) V(RD), and (D) V(MD), averaging over all sessions, are illustrated. Significant difference ($p<0.05$) from calculated metrics using WL is denoted with *.*

Inter-session repeatability as a function of NSA/NGD combination is shown in *Figure 3.5*. When an ROI of the whole liver was chosen, $V_{inter}(FA)$, $V_{inter}(\lambda_1)$, $V_{inter}(RD)$ and $V_{inter}(MD)$ were all less than 10%. No trends were observed in $V_{inter}(FA)$, $V_{inter}(\lambda_1)$, $V_{inter}(RD)$ and $V_{inter}(MD)$, based on number of gradient directions. The lowest DT metric variability was observed (CV = 1.4 – 6.4%) when ROI of the whole liver was chosen (**Table 3.2**). Furthermore, $CV(FA)$, $CV(\lambda_1)$, $CV(RD)$, and $CV(MD)$ were generally larger in the left liver lobe (CV = 7.0-16.8%) when comparing with the corresponding DT metrics of the right liver lobe (CV = 5.3-11.1%). Based on the Friedman test, significant differences were observed between the choice of ROI for inter-session variability of FA($p < 0.05$), MD ($p < 0.05$), λ_1 ($p< 0.05$) and RD ($p <0.05$). A significant difference between left liver lobe and whole liver were only observed in the inter-session variability of FA and λ_1 using Turkey's HSD test. A significant difference the right liver lobe and whole liver was also observed in the inter-session variability of RD ($p < 0.05$). However, no significant differences were observed between any of the NSA/NGD combinations ($p>0.05$) when assessed with Friedman and Turkey's HSD test.

Table 3.2: *Calculated DT metrics and corresponding CVs of 4 NSA/NGD combinations using small circular ROIs of the (LL) and right liver lobes (RL) and an ROI of the whole liver (WL) (**Figure 3.2**).*

ROI	combination (NSA/NGD)	FA		λ_1 [x10^{-3} mm^2/s]		RD [x10^{-3} mm^2/s]		MD [x10^{-3} mm^2/s]	
		Mean ± SD	CV [%]	Mean ± SD	CV [%]	Mean ±	CV [%]	Mean ±	CV [%]
Left Lobe (LL)	1/30	0.42 ± 0.07	16.8	4.23 ± 0.69	16.3	2.20 ± 0.14	6.4	2.88 ± 0.31	10.8
	3/12	0.34 ± 0.04	12.7	3.71 ± 0.36	9.7	2.18 ± 0.21	9.9	2.75 ± 0.23	8.4
	3/10	0.37 ± 0.06	16.1	3.77 ± 0.54	14.4	2.27 ± 0.17	7.7	2.71 ± 0.32	11.9
	5/6	0.39 ± 0.03	9.0	3.81 ± 0.33	8.6	2.16 ± 0.12	5.8	2.71 ± 0.19	7.0
Right Lobe (RL)	1/30	0.41 ± 0.04	10.9	2.81 ± 0.28	9.9	1.61 ± 0.18	11.1	2.01 ± 0.21	10.2
	3/12	0.32 ± 0.02	7.7	2.64 ± 0.21	8.1	1.69 ± 0.10	5.7	2.01 ± 0.17	8.5
	3/10	0.40 ± 0.02	5.7	2.95 ± 0.19	6.6	1.69 ± 0.15	9.1	2.11 ± 0.12	5.8
	5/6	0.41 ± 0.02	5.3	2.98 ± 0.30	9.9	1.65 ± 0.12	7.0	2.09 ± 0.17	8.3
Whole Liver (WL)	1/30	0.37 ± 0.02	6.4	3.72 ± 0.12	3.3	2.24 ± 0.09	4.1	2.73 ± 0.09	3.3
	3/12	0.31 ± 0.01	3.9	3.42 ± 0.06	1.6	2.17 ± 0.05	2.5	2.64 ± 0.05	1.9
	3/10	0.37 ± 0.01	2.6	3.58 ± 0.10	2.7	2.25 ± 0.05	2.3	2.64 ± 0.07	2.5
	5/6	0.38 ± 0.02	4.3	3.58 ± 0.07	2.0	2.13 ± 0.03	1.4	2.61 ± 0.04	1.4

An overall decreasing trend in V_{inter}(RD) was observed with increasing NSA for all ROIs (**Figure 3.6**). Also, a similar trend was observed for V_{inter} (λ_1) and V_{inter} (MD) with the whole liver ROI. When a smaller ROI was chosen (i.e. ROIs of the LL and RL), however, no trends were noted. Similar to other observations V_{inter} *(FA)*, V_{inter} *(λ_1)*, V_{inter} *(RD)* and V_{inter} *(MD)* were all less than 10% when assessing the whole liver ROI . Additionally, larger V_{inter} *(FA)* and V_{inter} *(λ_1)* were observed within ROIs of the left liver lobe (29.0-38.6% and 16.0-25.7% for V_{inter} *(FA)* and V_{inter} *(λ_1)*, respectively) compared to the right liver lobe (16.1-22.2% and 14.8-20.3% for V_{inter} *(FA)* and V_{inter} *(λ_1)*, respectively). No significant differences were observed over any DT inter-session DT variability (p>0.05) for all choices of NSA settings, using both Kruskal-Wallis and Turkey's HSD tests. However, significantly different test-retest variability from the whole liver , when compared with left liver lobe and right liver lobe) were observed using V_{inter}*(FA)*, V_{inter}*(λ_1)*, V_{inter}*(MD)* and V_{inter}*(RD)*.

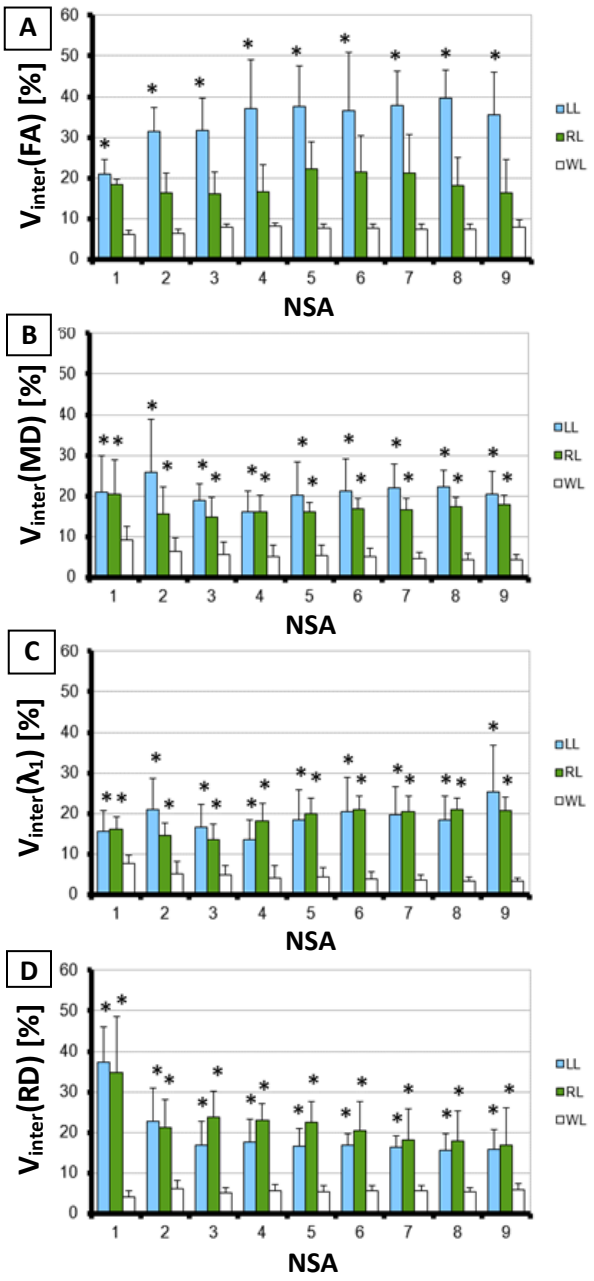

Figure 3.6: *Inter-session repeatability for 1 to 9 NSA using ROIs of left liver lobe (LL), right liver lobe (RL) and whole liver (WL) for (A) V(FA), (B) V(λ_1), (C) V(RD), and (D) V(MD). All values are shown represent the mean ±standard deviation over all sessions. Significantly different from the whole liver lobe is noted as *.*

The smallest CV for each calculated DT metric was obtained using the whole liver ROI (less than 5%). Although the *CV* of some estimated DT metrics was larger than 10%, when assessing individual liver lobes, they were still all less than 15% (except for $CV(\lambda_1)$ which was 21.2% when NSA = 1). Most importantly, the *CV(MD)* and $CV(\lambda_1)$ showed a decreasing trend as a function of NSA, when assessing the whole liver ROI. Apart from higher variation with NSA<4, a similar trend was also found in $CV(\lambda_1)$ and *CV(MD)* when analyzing individual liver lobe ROIs. Lastly, it was worth noting that increased *CV(FA)* as a function of NSA was observed in the right liver lobe (**Table 3.3**).

Table 3.3: *Calculated DT metrics and corresponding CVs for each combination of NSA (from 1 to 9) from a small circular ROI in the left liver lobe (LL), right liver lobe (RL) and an ROI encompassing the whole liver (WL) (**Figure 3.2**).*

ROI	NSA	FA		λ_1 [x10^{-3} mm^2/s]		RD [x10^{-3} mm^2/s]		MD [x10^{-3} mm^2/s]	
		Mean ± SD	CV [%]	Mean ± SD	CV [%]	Mean ± SD	CV [%]	Mean ± SD	CV [%]
Left Lobe (LL)	1	0.70 ± 0.06	9.1	5.76 ± 1.22	21.2	1.80 ± 0.18	10.2	2.89 ± 0.42	14.4
	2	0.54 ± 0.06	10.3	4.45 ± 0.61	13.7	2.07 ± 0.28	13.4	2.73 ± 0.29	10.7
	3	0.47 ± 0.05	9.8	4.13 ± 0.63	15.2	2.18 ± 0.21	9.9	2.73 ± 0.32	11.9
	4	0.42 ± 0.03	8.1	3.89 ± 0.36	9.2	2.21 ± 0.23	10.6	2.70 ± 0.20	7.5
	5	0.39 ± 0.03	9.0	3.81 ± 0.33	8.6	2.22 ± 0.20	9.2	2.71 ± 0.19	7.0
	6	0.36 ± 0.03	8.4	3.74 ± 0.35	9.2	2.25 ± 0.23	10.4	2.72 ± 0.21	7.6
	7	0.33 ± 0.03	7.5	3.70 ± 0.30	8.1	2.28 ± 0.24	10.7	2.75 ± 0.18	6.5
	8	0.32 ± 0.02	5.4	3.68 ± 0.25	6.8	2.28 ± 0.26	11.5	2.75 ± 0.16	6.0
	9	0.30 ± 0.02	6.3	3.61 ± 0.23	6.4	2.29 ± 0.25	10.9	2.59 ± 0.10	4.0
Right Lobe (RL)	1	0.77 ± 0.04	5.0	4.29 ± 0.49	11.4	1.34 ± 0.07	5.5	2.06 ± 0.13	6.4
	2	0.61 ± 0.03	4.4	3.39 ± 0.33	9.6	1.62 ± 0.14	8.8	2.00 ± 0.15	7.3
	3	0.52 ± 0.04	6.8	3.16 ± 0.31	9.7	1.69 ± 0.10	5.7	2.02 ± 0.14	7.2
	4	0.45 ± 0.03	6.1	3.06 ± 0.31	10.0	1.70 ± 0.08	5.0	2.07 ± 0.16	7.9
	5	0.41 ± 0.02	5.3	2.98 ± 0.30	9.9	1.73 ± 0.09	5.0	2.09 ± 0.17	8.3
	6	0.38 ± 0.02	6.4	2.89 ± 0.27	9.3	1.75 ± 0.09	5.0	2.08 ± 0.17	8.0
	7	0.36 ± 0.03	7.2	2.83 ± 0.25	8.8	1.75 ± 0.09	5.1	2.09 ± 0.16	7.6
	8	0.34 ± 0.03	8.2	2.76 ± 0.22	8.0	1.75 ± 0.10	5.7	2.07 ± 0.14	6.6
	9	0.33 ± 0.03	8.9	2.75 ± 0.20	7.3	1.77 ± 0.10	5.8	2.08 ± 0.12	6.0
Whole Liver (WL)	1	0.69 ± 0.03	4.2	5.16 ± 0.19	3.7	1.88 ± 0.09	4.9	2.74 ± 0.03	1.2
	2	0.54 ± 0.02	4.6	4.16 ± 0.11	2.7	2.08 ± 0.08	3.8	2.64 ± 0.03	1.1
	3	0.47 ± 0.02	3.8	3.88 ± 0.09	2.3	2.17 ± 0.05	2.5	2.63 ± 0.03	1.2
	4	0.42 ± 0.02	4.4	3.68 ± 0.06	1.7	2.20 ± 0.04	1.7	2.61 ± 0.02	0.9
	5	0.38 ± 0.02	4.3	3.58 ± 0.07	2.0	2.25 ± 0.02	0.9	2.61 ± 0.04	1.4
	6	0.36 ± 0.01	4.1	3.49 ± 0.06	1.7	2.27 ± 0.02	0.9	2.60 ± 0.03	1.1
	7	0.34 ± 0.01	4.3	3.45 ± 0.05	1.6	2.29 ± 0.03	1.2	2.62 ± 0.03	1.1
	8	0.32 ± 0.01	4.1	3.39 ± 0.04	1.2	2.30 ± 0.03	1.1	2.60 ± 0.01	0.5
	9	0.31 ± 0.01	3.8	3.36 ± 0.04	1.1	2.32 ± 0.02	0.9	2.61 ± 0.02	0.6

DISCUSSION:

Previous liver diffusion studies have focused on ADC repeatability when varying method of respiratory compensation [14] and with choice of b-value [15]. However, these studies were done only using the right liver lobe. This is likely because the left liver lobe often suffers from lower SNR, which potentially leads to an inaccurate diffusivity measurement [16,17]. Based on our study, larger inter-subject variability and intra-session test-retest variability of MD and RD were observed in the left liver lobe compared to that of the right lobe. This agrees with

Colagrande *et al*. where high ADC variability in the left liver lobe was noted [18]. However, we observed larger V_{inter}(RD) and V_{inter}(MD) in the right liver lobe using 5NSA/6NGD (i.e. same setting as the intra-session variability). It is worth noting that our DT metrics of the right liver lobe are not entirely free from pulsation and motion artifact. In fact, the difference between inter-session and intra-session repeatability of brain DTI has been attributed to motion artifact resulting from brain pulsation [9]. In addition, reproducibility of DT metrics are asalso affected by MR system performance including B_0 field inhomogeneity, scanner drift, and gradient coil stability [10,18]. These may contribute to additional inter-session error not otherwise observed in the intra-session scan.

Lowest test-retest variability was observed using a larger ROI (i.e. whole liver ROI). We noted significant inter-session differences between FA, λ_1, MD and RD, when comparing left liver to whole liver ROIs. Furthermore, a significant difference between intra-session FA and RD measurements were observed based on the Kruskal-Wallis test. However, significant difference between left liver and whole liver, and right liver and whole liver were only observed when comparing intra-session RD measurements. These results imply the repeatability of DT metric measurement depends on the choice of ROI. Even though we applied motion correction, we still implicate motion as a confounding factor that increases metric *CV* values.

There have been a number of approaches published for reporting repeatability of liver DWI reliability. Kim *et al.* reported the reproducibility of

ADC measurement on liver parenchyma and malignant hepatic tumors using both intraclass correlation coefficients (ICCs) and 95% Bland-Altman limit of agreement [19]. Some reported the reproducibility of liver ADC measurement only using 95% Bland-Altman limits of agreement [14,20]. Based on liver measurement reproducibility performed by Bilgili [15] and Rosenkrantz [21], the ADC *CV* of healthy liver parenchyma ranges between 9.7% to 16.2% and 7.3 to 10.6%, respectively, at 1.5T. Compared with the results of those studies, our calculated *CV*s for MD and RD, using NSA >1 for all choice of ROI, are comparable. Even though those previous studies were done to assess DWI reproducibility, it should be noted that our *CV(FA)*, done on DTI data also falls within a similar range. Thus liver DT is an appropriate and stable method for longitudinal diffusion quantification.

To the best of our knowledge, we are the first group studying the effect of NSA and NGD to the repeatability of liver DT metrics. Repeatability of DT metrics have been thoroughly investigated with human brain data, and the importance of diffusion gradient direction schemes [11] and SNR [9] are well characterized. In our study varying NSA was used to modulate SNR. The inter-session DT metric difference was shown to be insignificant to changes in NSA, based on Friedman test and Turkey's HSD test. However, this could be attributed to the small sample size. For all choice of ROIs, decreasing inter-session test-retest variability of RD was observed with an increase in NSA. Furthermore, decreases in *CV(FA)*, *CV(λ_1)* and *CV(MD)* were also observed with increasing

NSA. Thus the repeatability of liver DT metrics is affected by SNR, which is not surprising given similar conclusions were previously reported in human brain [9] and muscle DTI data [12]. However, no relationship between NGD and the repeatability of DT metrics can be drawn based on our results. The observed disagreement with the previous results using human brain and muscle data may be attributed to the structural difference between brain, muscle and liver parenchyma. When comparing muscle to brain white matter, diffusion is less restricted in muscle and as such the minimum NGD requirement is smaller for reliable muscle DT metric estimation [12]. In the case of liver parenchyma, where liver lobules have a close to symmetric structure and liver sinusoids are extremely leaky, water diffusion can be assumed to be even less restricted. As such, the minimum required NGD for reliable liver DT metric estimation could even be less than that for muscle (i.e. 12 gradients directions based on muscle studies by Froeling *et al.* [12]). In other words, there is a point at which adding NGD will not improve reliability further, and we suggest this is less than that found with muscle after which no or only very small benefit will be obtained. Although further verification may still be needed, we suspect that 6 NGD is the minimum requirement for reliable estimation of liver DT metrics as no further advantage was observed with addition of more directions.

It is noted that high FA value (>0.25) was obtained in all volunteers using all choice of NSA and gradient directions. More importantly, our estimated liver FA value was similar to that of the more fibrous human tissues such as muscle

and white matter. In particular, FA of healthy human calf muscle and white matter has been reported as 0.2-0.3 [12,22] and 0.4-0.7 [23], respectively. Isotropic diffusion, and hence FA~0, has previously been assumed for liver parenchyma [24,25]. We suspect anisotropic diffusion measures are the result of motion leading to liver deformation. Recently, DW signal modulation due to non-linear liver motion was reported to be prominent in healthy volunteers [17]. In a previous study cardiac motion was confirmed as the reason for artificially increasing liver FA [26].

In conclusion, the repeatability of DT metrics with varying NSA and NGD has been demonstrated. Based on our results, DT repeatability improves with increasing NSA. However, no benefit was observed with increasing NGD beyond 6 gradient directions. Lastly the choice of large ROIs increases the intra-session and inter-session repeatability of the measurement.

REFERENCE:

1. Girometti R., Furlan A., Esposito G., et al. Relevance of b-Values in Evaluating Liver Fibrosis: A Study in Healthy and Cirrhotic Subjects Using Two Single-Shot Spin-Echo Echo-Planar Diffusion-Weighted Sequences. J Magn Reson Imaging. 2008; 28: 411-9.
2. Talwalkar J.A., Yin M., Fidler J.L., et al. Magnetic Resonance Imaging of Hepatic Fibrosis: Emerging Clinical Applications. Hepatology. 2008; 47:332-42.
3. Erturk S.M., Ichikawa T., Kaya E., et al. Diffusion tensor imaging of cysts, hemagiomas, and metastases of the liver. Acta Radiol. 2014; 55: 654-60.
4. Naganawa S., Kawai H., Fukatsu H., et al. Diffusion Weighted Imaging of the liver: technical challenges and prospects for the future. Magn Reson Med Sci. 2005; 4:175-86.
5. Martino J., Lucas E.M. Subcortical anatomy of the lateral association fascicles of the brain: A review. Clinical Anatomy. 2014; 27: 563-69.
6. Anderson A.W. Theoretical Analysis of the Effects of Noise on Diffusion Tensor Imaging. Magn Reson Med. 2001; 46: 1174-88.
7. Ni H., Kavcic V., Zhu T., et al. Effects of Number of Diffusion Gradient Directions on Derived Diffusion Tensor Imaging Indices in Human Brain. AJNR Am J Neuroradiol. 2006; 27: 1776-81.

8. Jones D.K. The effect of gradient sampling schemes on measures derived from diffusion tensor MRI: A Monte Carlo study. Magn Reson Med. 2004; 51: 807-15.
9. Farrell J.A.D, Landman B.A, Jones C.K, et al. Effects of signal-to-noise ratio on the Accuracy and Reproducibility of DTI-derived Fractional Anisotropy, Mean Diffusivity, and Principle Eigenvector Measurements at 1.5T. J Magn Reson Imaging. 2007; 26: 756-7.
10. Veenith T.V., Carter E., Grossac J., et al. Inter Subject Variability and Reproducibility of Diffusion Tensor Imaging within and between Different Imaging Sessions. PLoS One. 2013; 8:e65941.
11. Landman B.A., Farrell J.A.D, Jones C.K., et al. Effect of diffusion weighted schemes on the reproducibility of DTI-derived derived fractional anisotropy, mean diffusivity, and principle eigenvector measurements at 1.5T NeuroImage. 2007; 36: 1123-38.
12. Froeling M, Nederveen A.J., Nicolay K., et al. DTI of human skeletal muscle: the effects of diffusion encoding parameters, signal-to-noise ratio and T2 on tensor indices and fiber tracts. NMR Biomed. 2013; 26:1339-52.
13. Behrens T.E.J, Woolrich M.W., Jenkinson M., et al. Characterization and propagation of uncertainty in diffusion-weighted MR imaging. Magn Reson Med. 2003; 50: 1077-88.
14. Kwee T.C., Takahara T., Koh D., et al. Comparison and Reproducibility of ADC Measurements in Breathhold, Respriatory Triggered, and Free-

Breathing Diffusion –Weighted MR Imaging of the Liver. J Magn Reson Imaging . 2008; 28:1141-8.

15. Bilgili MYK. Reproducibility of apparent diffusion coefficients measurements in diffusion-weighted MRI of the abdomen with different b values. Eur J Radiol. 2012; 81:2066-8.
16. Koh D, Collins D. Diffusion weighted MRI in the Body: Applications and challenges in oncology. AJR Am J Roentgenol. 2007; 188: 1622-35.
17. Nasu K, Kuroki Y, Kazama T, et al. Measurement of the apparent diffusion coefficient in the liver: is it a reliable index for hepatic disease diagnosis? Radiat Med. 2006; 24: 438-44.
18. Colagrande S., Pasquinelli F., Mazzoni L.N., et al. MR-Diffusion Weighted Imaging of Healthy Liver Parenchyma: Repeatability and Reproducibility of Apparent Diffusion Coefficient Measurement. J Magn Reson Imaging. 2010; 31: 912-20.
19. Kim S.Y., Lee S.S., Park B., et al. Reproducibility of Measurement of Apparent Diffusion Coefficients of Malignant Hepatic Tumors: Effect of DWI Techniques and Calculation Methods. J Magn Reson Imaging. 2012 36: 1131-8.
20. Larsen N.E., Haack S., Larsen L.P.S, et al. Qualitative liver ADC measurements using diffusion-weighted MRI at 3 Tesla: evaluation of reproducibility and perfusion dependence using different techniques for respiratory compensation. 2013; Magn Reson Mater Phy 26: 431-42.

21. Rosenkrantz A.B, Oei M., Babb J.S., et al. Diffusion-Weighted Imaging of the Abdomen at 3.0 Tesla: Image Quality ad Apparent Diffusion Coefficient Reproducibility Compared With 1.5Tesla. J Magn Reson Imaging. 2011; 33: 128-35.
22. Sinha S, Sinha U, Edgerton R. In Vivo Diffusion Tensor Imaging of the Human Calf Muscle. J Magn Reson Imaging. 2006; 24: 182-90.
23. Assaf Y, Pasternak O. Diffusion Tensor Imaging (DTI)-based White Matter Mapping in Brain Research: A Review. J Mol Neurosci 2008; 34: 51-61.
24. Taouli B, Vilgrain V, Dumont E, et al. Evaluation of Liver Diffusion Isotropy and Characterization of Focal Hepatic Lesions with Two Single-Shot Echo-planar MR Imaging Sequences: Prospective Study in 66 Patients. Radiology. 2003; 226: 71-8.
25. Taouli B, Martin A.J., Qayyum A, et al. Parallel imaging and diffusion tensor imaging for diffusion-weighted MRI of the liver: preliminary experience in healthy volunteers. AJR Am J Roentgenol. 2004; 183: 677-80.
26. Wong OL, Lo G.G., Lee R, et al. The effect of respiratory and cardiac motion in liver diffusion tensor imaging (DTI). J Comput Assist Tomogr. 2014; 38: 352-9

CHAPTER 4

EFFECT OF RESPIRATORY AND CARDIAC MOTION IN LIVER DTI

Effect of Respiratory and Cardiac motion in Liver DTI

Oi Lei Wong, MSc, Gladys Goh Lo, MD., Raymond Lee, MSc, Wing Wa Li, MSc, Po Lung Chan, MSc, Siu Ki Yu, Ph.D. and Michael D. Noseworthy, Ph.D., P.Eng

4.1 CONTEXT OF THE PAPER

Although isotropic diffusion in the liver has been assumed based on the histological structure of liver lobules, unexpectedly high FA values have been reported in resent studies[70]. More importantly, signal dropout due to cardiac motion has been shown to be non-linear motion related, so called pseudo-hepatic artifact [78]. We, therefore, proposed the presence of the pseudo-hepatic artifact can be illustrated using DT metrics in the presence of respiratory and cardiac motion.

4.2 DECLARATION STATEMENT

Oi Lei Wong as principle author wrote the article, designed the experiment, collected the data, performed analysis and created figures and tables as appropriate. Michael D. Noseworthy, as corresponding author, provided guidance and advice, and performed proofreading/editing and submission of the manuscript for publication. Dr. Gladys Lo provided clinical guidance and

commentary. Raymond Lee, Po Lung Chan and Wing Wah Li provided clinical commentary and performed the MR image acquisition. Dr. Siu Ki Yu provided methodological commentary.

This paper has been published in the journal *Journal of Computer Assisted Tomography*.

4.3 PAPER

The Effect of Respiratory and Cardiac Motion in Liver Diffusion Tensor Imaging (DTI)

Oi Lei Wong, MSc[1,2,3], Gladys Goh Lo, MD.[4], R Lee, MSc[4],Wing Wa Li, MSc[4] Po Lung Chan, MSc[4] Siu Ki Yu, Ph.D. [3] and Michael D. Noseworthy, Ph.D., P.Eng.[1,2,5,6†]

[1]Department of Medical Physics and Applied Radiation Science, McMaster University, Hamilton, Ontario, Canada.
[2]Image Research Center, St. Joseph's Healthcare, Hamilton Ontario, Canada.
[3]Medical Physics and Research Department, Hong Kong Sanatorium & Hospital, Hong Kong Special Administrative Region (SAR), China.
[4]Intervention and Radiology Department, Hong Kong Sanatorium & Hospital, Hong Kong Special Administrative Region (SAR), China.
[5]School of Biomedical Engineering, McMaster University, Hamilton, Ontario, Canada.
[6]Department of Electrical and Computer Engineering, McMaster University, Hamilton, Ontario, Canada.

***Corresponding Author:**
Dr. Michael D. Noseworthy, Ph.D., P.Eng.
Director, McMaster School of Biomedical Engineering,
Associate Professor, Department of Electrical and Computer Engineering,
McMaster University.
Hamilton, Ontario, Canada.
email: nosewor@mcmaster.ca
voice: +1 1 (905) 925-9140 ext.23727
http://www.ece.mcmaster.ca/~mikenose/web/HOME.html

ABSTRACT

Objective: To evaluate the effect of respiratory and cardiac motion on diffusion tensor imaging (DTI) metrics in healthy human liver.

Methods: Fifteen healthy subjects, participating in either part of this study, were scanned using a 1.5-T magnetic resonance imaging (MRI) device. Coronal liver DTI (6 diffusion-encoding directions; b, 300 mm2/s) during breath holding was compared to free breat5hing. Cardiac motion effects were evaluated by comparing breath-held DTI scans acquired during both diastole and systole.

Results: Free breathing resulted in a significantly increased mean diffusivity ($P < 0.05$), $\lambda 1$ ($P < 0.01$), $\lambda 2$ ($P < 0.05$), and $\lambda 3$ ($P < 0.01$) compared to breath holding. During systole significant increases in fractional anisotropy ($P < 0.05$), mean diffusivity ($P < 0.05$), and $\lambda 1$ ($P < 0.05$), compared to diastole, were found in the left lobe. The right lobe, which is less affected by cardiac motion, showed no significant change in DTI metrics over the cardiac cycle.

Conclusions: Respiratory and cardiac motion tends to increase liver DTI metrics.

KEYWORDS:

Magnetic resonance imaging (MRI), Diffusion tensor imaging (DTI), Healthy liver

INTRODUCTION:

Diffusion-weighted imaging (DWI) and diffusion tensor imaging (DTI) are well recognized methods to assess microstructural characteristics of tissues. Diffusion imaging has been reported with acceptable sensitivity and specificity in diagnosing liver fibrosis and inflammation.[1] Others have also reported the usefulness of DWI in detection of tumor response[2,3], liver metastases [4], and cirrhosis [5]. Compared to DTI, DWI is more clinically accepted because breath holding is possible. Although the precision of the measured DTI metrics are, in theory, superior to DWI metrics [6,7], only a limited amount of research has been done on the application of DTI in liver [8–10]. The reason behind this is that most likely, the DTI sequence is very sensitive to motion [11,12]. However, cardiac and breathing-induced artifacts are significant in liver, especially in the left lobe. Furthermore, Taouli et al reported that liver DTI data were noisier compared with DWI [13,18], which led to their conclusion that DWI was better at staging fibrosis and grading inflammation [19].

To compensate for technical issues associated with liver diffusion measurement navigator echoes (1-dimensional [1D] and 2D), breath holding and respiratory triggering have been applied to reduce motion problems [14–17]. Furthermore, reducing diffusion *b*-value is essential for improving signal-to-noise ratio (SNR) for any liver diffusion work. This is even more important for DTI, where the combinations of multiple concurrent gradients, required to encode the

tensor, reduces overall signal. Improved SNR for DTI is often achieved through increased averaging, making the scan length even longer than DWI.

In addition to DTI technical difficulties when probing the abdomen, a further reason limiting use for liver imaging is the assumption that liver diffusion is isotropic, based on the histological organization of its parenchyma [18]. Isotropy is assumed based on the statistical similarity between measured diffusivity along orthogonal directions x, y, and z in DWI (ie, $D_{xx} = D_{yy} = D_{zz} = 0$, where D corresponds to the measured diffusivity and the subscript corresponds to the gradient encoding direction). If valid, isotropic diffusion would be reflected in a fractional anisotropy (FA) near zero. However, DTI studies in both humans and animals have reported significantly nonzero FA values, implying that the assumption of isotropic diffusion is false [14–16]. However, this conclusion should be made with caution as apparent increased FA of an isotropic medium occurs when image noise is elevated [19]. Alternatively, as FA reflects the shape of the sphere of water diffusivity, tissue deformation could, in theory, change FA. A tagging sequence has shown that the left liver lobe changes shape and deforms during the cardiac cycle [20]. It has also been suggested that deformation of the liver tissue leads to change in water diffusivity [21] known as hepatic pseudoanisotropy [22]. We hypothesized that this deformation could lead to changes in liver DTI metrics. Because DTI is more quantitative than DWI, and as such could be beneficial to better quantifying disease before and after therapy, it is essential to understand normal physiological variations caused by thoracic

motion. Therefore, in this study, we assessed the effects of both cardiac cycle and respiratory motion on DTI metrics.

MATERIALS AND METHODS:

Fifteen healthy volunteers (7 men and 8women; mean age, 33 ± 11 years) were recruited for the study, and informed consent was obtained from each. The study was approved by our local research ethics board before the start of the study, and all subjects provided written consent for their participation.

All magnetic resonance (MR) scanning was performed using a 1.5-T Siemens Espree MR scanner and a dedicated 12-channel body radio frequency receiver array (Siemens Healthcare, Erlangen, Germany) with subjects in supine position. A routine 3-plane localizer and coronal T2-weighted half Fourier acquired single turbo spin echo scan (echo time [TE]/repetition time [TR], 78/750 milliseconds [ms]; matrix, 460 × 512; field of view [FOV], 35 cm; number of excitations, 1; slices, 5; slice thickness, 10 mm; no gap; fat saturation on) were collected to localize anatomical structures.

Two separate experiments focused on assessing effects of either respiratory or cardiac motion were conducted. The influence of respiratory motion was determined by comparing DTI data acquired during free breathing or breath holding. Cardiac motion effect on DTI was studied by comparing calculated DT metrics acquired during multiple phases of the cardiac cycle. To assess the relationship between DTI metrics and thoracic induced motion, we

acquired DT images in the coronal direction. Liver motion is primarily superior-inferior [23]. Coronal images allow better motion compensation than axial images, and part of the myocardium can also be included in the imaging plane.

Assessing Effect of Respiratory Motion

Ten healthy volunteers (5 men and 5 women, mean age, 34 ± 12) participated in this part of the study. Breath holding included 3 separate contiguous coronal DTI scans using a dual spin echo diffusion echo planar imaging sequence (TE/TR, 69/2200 ms; matrix, 110 × 110; number of excitations, 1; FOV, 35 cm; slices, 5; thickness, 10 mm; no gap; b value, 300 seconds/mm^2, gradient directions, 6; fat saturation on; partial fast Fourier transform, 6/8; 24 seconds per average). Each volunteer was instructed to perform breath holding at inspiration for each acquisition. All scans were done using identical prescan values (shim settings, center frequency, and transmit/receive gain values) and geometric prescription. Motion and eddy current corrections were done before summation of the 3 scans, making the end result effectively a 3-average acquisition. Although respiratory motion was compensated for by breath holding, nonlinear registration was still deemed required. Registration was done by linearly transforming the images of each acquisition to the chronologically first b = 0 second/mm^2 image of the first DTI acquisition of each subject. This was accomplished with the MCFLIRT utility of The FMRIB Software Library (FSL) [24] (FSL 4.1, Oxford Centre for Functional Magnetic Resonance Imaging of the Brain Analysis Group, Oxford, UK). Eddy current correction was then performed

on each motion-corrected acquisition using FSL, and the results were summed before calculating the tensor. The resultant DTI metrics (FA, mean diffusivity (MD), λ_1, λ_2, and λ_3) calculated using the FMRIB diffusion toolbox plugin of FSL [25] were subsequently statistically analyzed (described in a later section).

Free-breathing DTI acquisition was performed using the same scan parameters and analysis pipeline as that of the breath-holding acquisition.

Assessing Effect of Cardiac Motion

Five healthy volunteers (2 men and 3 women; mean age, 32 ± 11) participated in this part of the study. Eight sets of coronal liver DTI acquisitions, each at a differing cardiac trigger delays (beginning at end systole), were acquired using a dual spin echo DTI-echo planar imaging sequence (TE/TR, 69/1000 ms; matrix, 110 × 110; 1 average; FOV, 35 cm; 5 slices; thickness, 10 mm; no gap; b value, 300 seconds/mm^2; gradient directions, 6; fat saturation on; partial fast Fourier transform, 6/8; 18 seconds per average). The eight trigger delays (0, 50, 100, 200, 300, 400, 500, and 600 ms) were chosen such that components of both systole (early delays) and diastole (later delays) could be visualized. A total of 3 separately acquired DTI data sets (ie, averages) were acquired for each cardiac trigger delay (ie, a total of 24 liver DTI scans per volunteer).

Motion compensation was performed prospectively by a combination of breath holding (at inhalation) and pulsed oximeter triggering at peak of the pulse, attached to the left index finger or the left middle finger. Average heart rate was recorded concurrently with each scan for use in calculating the temporal

occurrence of individual cardiac phases. Motion and eddy current corrections were performed on each acquisition before combining all three, effectively resulting in an acquisition with 3 averages, which was then used in calculating the diffusion tensor. Nonlinear registration, eddy current correction, and calculation of the diffusion tensor metrics (FA, MD, λ_1, λ_2, and λ_3) for each of the 8 cardiac phases were performed as previously described using the FMRIB diffusion toolbox plugin of FSL 4.1.

Statistical Analysis

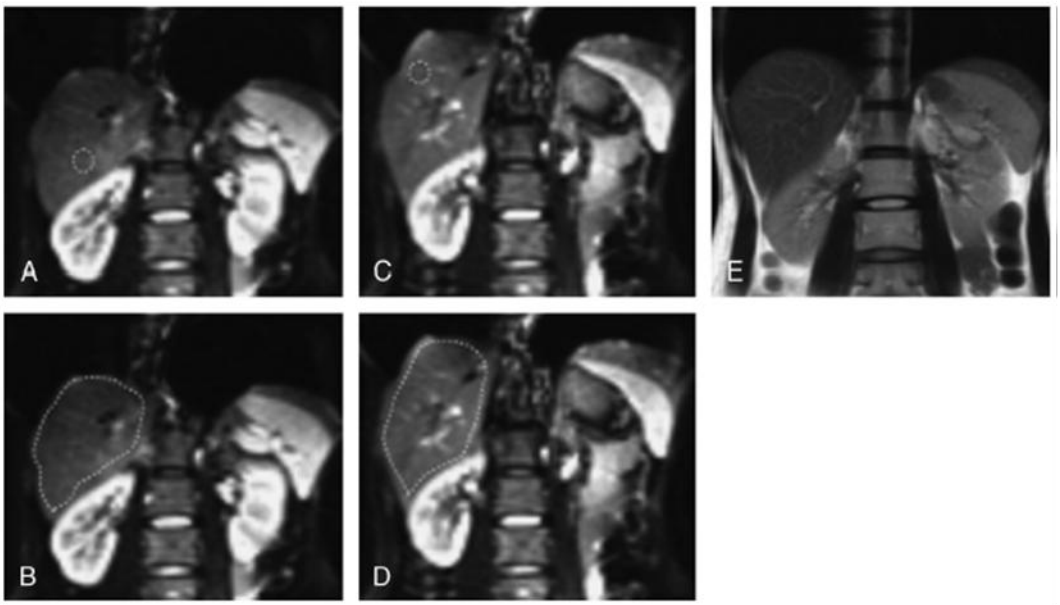

Figure 4.1: *Regions of interest shown on b = 0s/mm^2 images in healthy volunteer's liver during breath holding (A and B) and free breathing (C and D). Circular ROIs (A and C) were chosen in the most homogeneous region of the right lobe, avoiding major blood vessels. Whole-liver ROIs (B and D) show that major blood vessels were not excluded. Figure (E) shows the T2-weighted half Fourier acquired single turbo spin echo image of the same slice.*

To compare the effect of respiratory motion, 5 circular regions of interest (ROIs) (diameter, 10 mm; one per slice) were selected within the right liver lobe parenchyma on both the free breathing and breath-holding scans. Regions of

interest were chosen using the T2-weighted anatomical scans to avoid major blood vessels (Figure 4.1). The global mean of all 5 ROIs was used in subsequent statistical analysis. Region of interest analysis of the whole liver was also performed using the T2-weighted anatomical images as a guide (Figure 4.1). Statistical evaluation of the effect of breath holding, on regional and whole liver DTI metrics, was done using a 2-tailed paired Student's *t* test

In assessing effects of cardiac motion, analysis was done on a single slice in which the inferior aspect of the heart could be visualized over all 8 trigger delay settings. Analysis was performed on 10-mm diameter circular ROIs, selected on T2-weighted images to ensure blood vessel avoidance, in each of the right and left liver lobes (Figure 4.2). Data from the calculated cardiac phases occurring before 400 ms were assumed systolic, and those larger than 400 ms were assumed diastolic. Only data from cardiac phases ranging between 100 and 400 ms, and between 500 and 800 ms were included in statistical analysis to account for possible occurrence of a longer diastolic phase in any subject. Our cardiac phase selection was inclining with selection reported in the literature [20,21].

A statistical comparison was performed to compare diastole with systole, on a regional basis (ie, for either the left or right lobe) using a 2-tailed paired Student's t test.

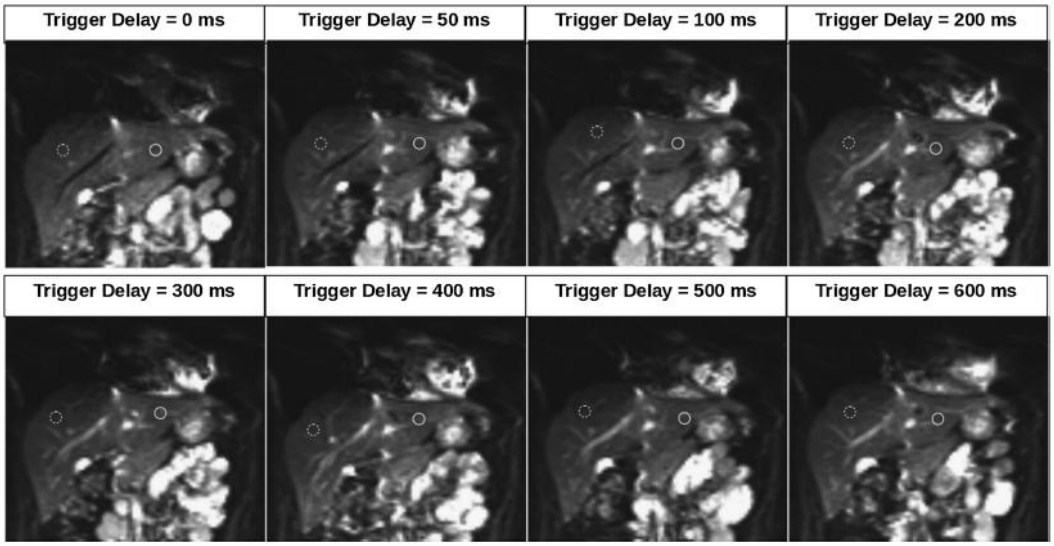

Figure 4.2: *Circular ROIs of the left (solid line) and right (dotted line) liver lobe shown on b = 0 mm2/s images at each trigger delay.All ROIs were selected to avoid major blood vessels.*

RESULTS:

Respiratory Motion Effects

Whole liver FA and MD and were significantly increased during free breathing compared to breath holding ($P < 0.05$; Figure 4.3). Furthermore, both the first and second eigenvalues (λ_1 and λ_2) were statistically greater ($P < 0.01$) when DTI data were acquired during free breathing (Figure 4.3). When only considering a subsample of the entire liver (ROI in the right lobe), free breathing resulted in a significantly increased MD ($P < 0.05$), λ_1 ($P < 0.01$), λ_2 ($P < 0.05$), and λ_3 ($P < 0.01$), with no statistically relevant effect on FA (Figure 4.3).

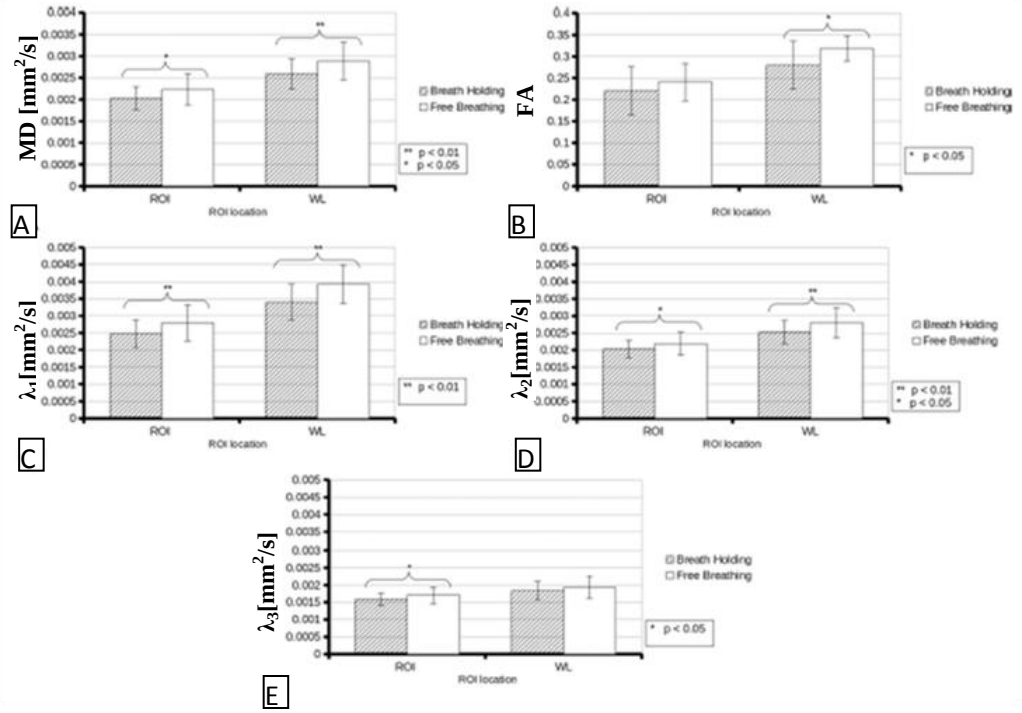

Figure 4.3: *A, Right liver lobe MD averaged over small ROIs and over the whole liver (WL) are illustrated. Based on a 2-tailed paired Student t test, significant increase in MD during free breathing was observed in both ROI and WL analyses. B, Significant increase in FA during free breathing was observed in WL. C, Significant increase in λ_1 during free breathing was observed in both ROI and WL. D, Significant increase in λ_2 during free breathing was observed in ROI and in WL. E, Significant increase in λ_3 during free breathing was observed in ROI (*P < 0.05, **P < 0.01).*

measurements showed when DTI data were acquired during systole; there was a significant increase in FA ($P < 0.05$), MD ($P < 0.05$), and λ_1 ($P < 0.05$) in the left liver lobe. Diffusion tensor imaging metrics did not significantly vary between diastole and systole in the right liver lobe (Figure 4.5).

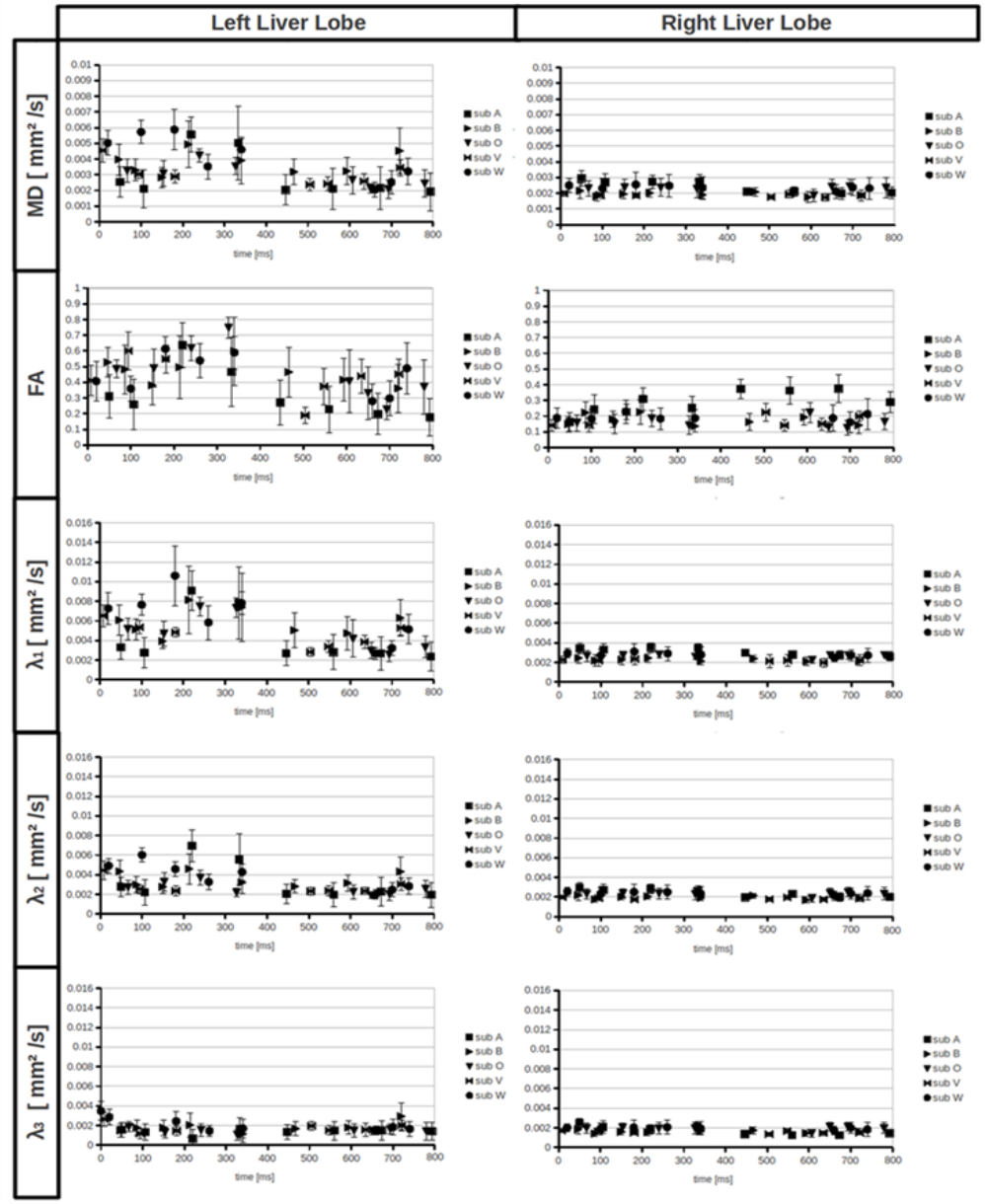

Figure 4.4: *Calculated DTI metrics (FA, MD, and eigenvalues), in the right and left liver lobes, during various trigger delays throughout the cardiac cycle. The variability was consistently higher for all measurements in the left lobe. The maximal FA (left lobe) was approximated to occur at approximately 300 ms*

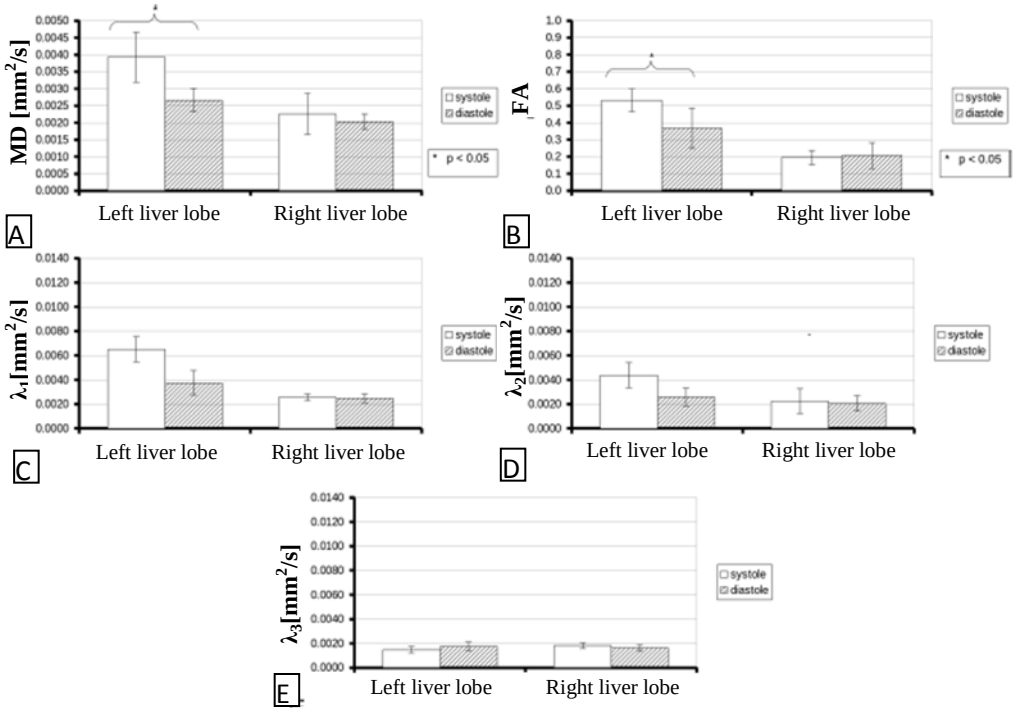

Figure 4.5: *Using 2-tailed paired Student t tests: A, MD significantly increased (*P < 0.05) only in the left lobe and during systole; FA significantly increased (*P < 0.05) only in the left lobe during systole (B); λ_1 significantly increased (*P < 0.05) in the left lobe during systole (C); no significant change in λ_2 was noted between systole and diastole in either left or right lobes (D); and no significant differences in λ_3 was found between systole and diastole in either left or right lobes (E).*

DISCUSSION:

Application of DWI or DTI in the liver can be challenging owing to signal loss in the left lobe, leading to increased error in diffusion calculations [21,26,30]. In fact, it is of clinical importance to be able to apply DWI or DTI in both liver lobes. As cardiac contractility, vascular pulsation, and respiratory motion all leading to nonlinear deformation have been suggested as factors involved in this

signal loss [20,21,30,31], better understanding in the effects of motion on the DT metrics should improve its clinical significance in categorizing diffusive liver diseases. As the right liver lobe seems less affected by cardiac motion, we assessed respiratory and cardiac sources as possible factors driving regional variation in DT metrics.

To the extent of our knowledge, comparisons between free breathing and breath holding reported in the literature were all done using DWI. Although direct comparison between the apparent diffusion coefficient (ADC) (determined using DWI) and mean diffusivity (determined using DTI) is difficult owing to their difference in the fundamental nature, they have been shown to be similar in healthy liver using multi–breath holding (MD and ADC ranging between 128 to 180×10^{-5} mm^2/s and 127 to 199×10^{-5} mm^2/s, respectively) [19]. Mean diffusivity obtained in our study in the right liver lobe, which was $200 \pm 53 \times 10^{-5}$ mm^2/s during breath holding and significantly elevated to $220 \pm 94 \times 10^{-5}$ mm^2/s during free breathing, was comparable but at the higher end of the published range. Our differing result could be the result of our choice of b value, where ADC or MD can be elevated when a low b value is chosen [27]. Another confounding factor could also be perfusion, which can result in apparently higher ADC or MD owing to the intravoxel incoherent motion (IVIM) effect. However, IVIM typically is visible with b values less than 50. As our choice of b values was 0 and 300 seconds/mm^2, or approximately 6 times larger than the "perfusion region" [30] in signal versus b value plots (with good reproducibility [28]), any

pseudoelevation in MD due to our choice in b value should lead to the same small source of error. Therefore, any perfusion effects should not affect our conclusion that motion leads to increase in MD. Similar results has been reported in patients with cirrhosis and/or focal liver lesions, where a significant increase in ADC using 2D navigator compensated DWI ($100 \pm 27 \times 10^{-5}$ mm^2/s) compared to breath holding (91 ± 26 × 10−5 mm2/s) was observed [23]. Twee et al reported ADC of healthy liver parenchyma ranging between 157 and 162 $\times 10^{-5}$ mm^2 /s during breath holding, between 162 and 165 $\times 10^{-5}$ mm^2/s during free breathing and 207 to 227 $\times 10^{-5}$ mm^2 /s with respiratory triggering using a 3-diffusion direction DWI scan [22]. They further concluded that change in ADC between free breathing and breath holding was insignificant. However, they did not correct for the possible calculation error that may arise from misregistration between each breath hold acquisition.

Healthy human liver has been shown to have a nonzero FA approaching 0.3 (whole liver) [16]. We report FA of 0.22 ± 0.05 during breath holding and 0.24 ± 0.04 during free breathing for the right lobe. As MD, FA, and eigenvalues were calculated using the same set of measured data, the observed increases in the absence of respiratory modulation should be reliable. The nonzero FA value can be explained through the hepatic pseudo anisotropy artifact, which is caused by liver deformation inducing regional signal loss when motion-probing gradients are applied [31]. Small local motion due to nonlinear organ motion is directional and can be detected by diffusion encoding scans as a contaminant in water diffusion

motion [31]. In the presence of cardiac motion and arterial pulsation, small nonrigid liver motion may still exist even during breath hold [21]. Thus, this is misinterpreted as anisotropic diffusion [21,31]. Nevertheless, the standard deviation of MD and eigenvalues were larger in free breathing DTI scan than in breath-holding DTI, showing that motion contributes, not surprisingly, to error.

We noted a significant difference in DT metrics between left and right liver lobes when the diffusion acquisition was cardiac gated during breath holding at inhalation Figs. 4, 5). The FA in the left liver lobe, as opposed to the right, varied during cardiac triggering. Kwee et al [21] concluded that left liver lobe signal loss during DWI was the result of cardiac motion. However, it is worth emphasizing that motion compensation can only minimize the effect of motion [31]. Our observed regional difference showed that change in DT metrics is not purely due to liver motion. In a further study by Chung et al, where liver stiffness was assessed throughout the cardiac cycle using an electrocardiogram (ECG)-gated SPAtial modulation of magnetization sequence, the left liver lobe showed higher strain and motion than the right [29]. Furthermore, Nasu et al reported liver image from cirrhotic patients were less susceptible to hepatic pseudoanisotropy artifact than healthy volunteers [31]. This implied that the amount of liver deformation plays an important role in this artifact. During the cardiac cycle, the heart interacts with the diaphragm to produce superior-to-inferior pressure waves, which propagate through the liver and distort the symmetry of the liver parenchymal structure. As eigenvalues refer to the

magnitude molecular displacement in a particular voxel, they are sensitive to the change in the shape of the diffusion ellipsoid. In this case, the disturbance of the liver parenchyma is reflected as a change in FA and eigenvalues.

It has even been shown that cardiac pulsation artifacts in the brain resulted from stretch and shear of the tissue and were greatest at 120 ms after the R wave [17]. Murtz et al also reported the signal loss was greatest when the cardiac trigger delay was set between 400 and 600 ms from peak oxygenation using a pulsed oximeter [20]. This agrees with our observation that significant change occurs at systole, where the contractile motion of the heart leads to the enchantment of the hepatic pseudoanisotropy artifact. At diastole, on the other hand, the heart is not contracting; and as such, the hepatic pseudoanisotropy artifact is reduced.

Despite the delay time between the ECG QRS complex and the plethysmographic pulse wave in subjects, this variation was reported to be negligible in healthy subjects [17]. Thus, cardiac trigging based on pulsed oximeter provides an acceptable estimation of the cardiac phase if the time delay is correctly included in the estimation. Furthermore, a pulsed oximeter is easier to use. Our way of estimating the cardiac phase using the pulsed oximeter is reliable because the MR system was able to log the triggering time and beat-to-beat heart rate of each volunteer. Nonetheless, the potential phase difference between the ECG QRS complex and the peak of the plethysmographic pulse wave was considered and shown as insignificant in our interpretation.

Concurrent respiratory and cardiac triggering cannot easily be done simultaneously using our system, without pulse programming. Moreover, it is not practical and considerably lengthens scan time. Hence, more efficient scanning is done with fast scanning and cardiac triggering. To achieve a manageable breath hold time, we were forced to reduce the scan time by reducing TR. However, this leads ultimately to reduction of SNR owing to incomplete signal recovery. Although the required SNR level for reliable DTI metrics is related to the organ and b value used, it has been suggested that 20 is the minimum requirement, albeit for skeletal muscle [29]. The average SNR for a single average was between 15 and 20. As 3 averages were combined in our study, the resultant final SNR used in tensor calculations was between 26 and 35. Therefore, it was concluded that the low TR for the DTI acquisition still resulted in reliable data, based on SNR requirements.

This study has several limitations. First, the distance between the heart and the liver increased during inhalation. Extra time delay may be needed for the mechanical wave to travel from the heart to the liver. Performing the scan at end expiration could reduce this possible error. However, this would even be more difficult to perform, even for healthy individuals, as the experiment would then involve breath holding at end expiration for 18 seconds repeatedly 24 times. The application of breath holding in cardiac-triggered DTI limits the feasibility of liver DTI clinically, where patients often have difficulty in performing breath holding. In addition, if DTI is to be of use clinically, an increase in the number of

diffusion-encoding gradients would be necessary to estimate the tensor better. This would lead to longer breath holding times. Although multi–breath hold DTI scans with cardiac triggering can potentially solve these problems, this is not currently a feature on clinical systems.

CONCLUSIONS:

In this study, we demonstrated that DTI metrics increase with respiratory and cardiac motion. Based on our results, error from respiratory motion leads to increased MD, FA, and eigenvalues in the right lobe. However, the significant increase in DT metrics in the left lobe when compared to the right lobe was not solely due to motion error. We showed how FA, MD, and $\lambda 1$ change significantly according to the phase of the cardiac cycle and concluded that the hepatic pseudoanisotropic effect related to the degree of liver deformation is the cause.

REFRENCE:

1. Taouli B, Chouli M, Martin AJ, et al. Chronic hepatitis: role of diffusion-weighted imaging and diffusion tensor imaging for the diagnosis of liver fibrosis and inflammation. J Magn Reson Imaging. 2008;28:89–95.
2. Dudeck O, Zeile M, Wybranski C, et al. Early prediction of anticancer effects with diffusion-weighted MR imaging in patients with colorectal liver metastases following selective internal radiotherapy. Eur Radiol. 2010;20:2699–2706.
3. Eccles CL, Haider EA, Haider MA, et al. Change in diffusion weighted MRI during liver cancer radiotherapy: preliminary observations. Acta Oncol. 2009;48:1034–1043.
4. Hardie AD, Naik M, Hecht EM, et al. Diagnosis of liver metastases: value of diffusion-weighted MRI compared with gadolinium-enhanced MRI. Euro Radiol. 2010;20:1431–1441.
5. Patel J, Sigmund E, Rusinek H, et al. Diagnosis of cirrhosis with intervoxel incoherent motion diffusion MRI and dynamic contrast enhanced MRI along and in combination: preliminary experience. J Magn Reson Imaging. 2010;31:589–600.
6. Jones DK, Horsfield MA, Simmons A. Optimal strategies for measuring diffusion in anisotropic system by magnetic resonance imaging. Magn Reson Med. 1999;42:515–525.

7. Basser PJ, Mattiello J, LeBihan D. MR diffusion tensor spectroscopy and imaging. Biophys J. 1994;66:259–267.
8. Cheung JS, Fan SJ, Gao DS, et al. Diffusion tensor imaging of liver fibrosis in an experimental model. J Magn Reson Imaging. 2010;32:1141–1148.
9. Cheung JS, Fan SJ, Chow AM, et al. In vivo DTI assessment of hepatic ischemia reperfusion injury in an experimental rat model. J Magn Reson Imaging. 2009;30:890–895.
10. Lu L, Haus JM, Flask CA. Liver DTI of obese insulin resistant subjects with fatty liver disease. In: Proceedings of the18th Annual Meeting of International Society for Magnetic Resonance in Medicine (ISMRM), Stockholm, Sweden: 2010;18:4710.
11. Pierpaoli C, Marenco S, Rohdes G, et al. Analyzing the contribution of cardiac pulsation to the variability of quantities derived from the diffusion tensor. In: Proceedings of the 11th Annual Meeting of International Society of Magnetic Resonance in Medicine (ISMRM), Toronto, Canada. 2003;11:70.
12. Taouli B, Koh DM. Diffusion weighted MR imaging of the liver. Radiology. 2010;254:47–66.
13. Taouli B, Martin AJ, Qayyum A, et al. Parallel imaging and diffusion tensor imaging for diffusion weighted MRI of the liver: preliminary experience in healthy volunteers. AJR Am J Roentgenol. 2004;183:677–680.

14. Mürtz P, Flacke S, Träber F, et al. Abdomen: diffusion-weighted MR imaging with pulse-triggered single shot sequences. Radiology. 2002;224:258–264.
15. Kwee TC, Takahara T, Niwa T, et al. Influence of cardiac motion on diffusion-weighted magnetic resonance imaging of the liver. Magn Reson Mater Phy. 2009;22:319–325.
16. Kwee TC, Takahara T, Koh D, et al. Comparison and reproducibility of ADC measurements in breathhold, respiratory triggered and free-breathing diffusion-weighted MR imaging of the liver. J Magn Reson Imaging. 2008;28:1141–1148.
17. Taouli B, Sandberg A, Stemmer A, et al. Diffusion-weighted imaging of the liver: comparison of navigator triggered and breathhold acquisition. J Magn Reson Imaging. 2009;30:561–568.
18. Taouli B, Vilgrain V, Dumont E, et al. Evaluation of liver diffusion isotropy and characterization of focal hepatic lesions with two single shot echo planar MR imaging sequences: prospective study in 66 patients. Radiology. 2003;226:71–78.
19. Basser PJ, Jones DK. Diffusion tensor MRI: theory, experimental design and data analysis—a technical review. NMR Biomed. 2002;15:456–467.
20. Chung S, Breton E, Mannelli L, et al. Liver stiffness assessment by tagged MRI of cardiac-induced liver motion. Magn Reson Med. 2011;65:949–955.

21. Koh D, Collins D. Diffusion weighted MRI in the Body: Applications and challenges in oncology. AJR Am J Roentgenol. 2007;188:1622–1635.
22. Nasu K, Kuroki Y, Fujii H, et al. Hepatic pseudo-anisotropy: a specific artifact in hepatic diffusion-weighted images obtained with respiratory triggering. Magn Reson Mater Phys. 2007;20:205–211.
23. Nguyen NT,Moseley JL, Dawson LA, et al. Adapting liver motion models using a navigator channel technique. Med Phys. 2009;36:1061–1074.
24. Jenkinson M, Bannister PR, Brady JM, et al. Improved optimization for the robust and accurate linear registration and motion correction of brain images. NeuroImage. 2002;17:825–841.
25. Behrens TEJ, Woolrich MW, Jenkinson M, et al. Characterization and propagation of uncertainty in diffusion-weighted MR imaging. Magn Reson Med. 2003;50:1077–1088.
26. Nasu K, Kuroki Y, Kazama T, et al. Measurement of the apparent diffusion coefficient in the liver: is it a reliable index for hepatic disease diagnosis? Radiat Med. 2006;24:438–444.
27. Yamada I, Aung W, Himeno Y, et al. Diffusion coefficients in abdominal organs and hepatic lesions: evaluation with intravoxel incoherent motion echo-planar MR imaging. Radiology. 1999:210:617–623.
28. Stefano C, Pasquinelli F, Mazzoni L N, et al. MR-diffusion weighted imaging of healthy liver parenchyma: repeatability and reproducibility of apparent diffusion coefficient measurement. J Magn Reson Imaging. 2010;31:912–920.

29. Damon BM. Effects of image noise in muscle diffusion tensor (DT)-MRI assessed using numerical simulations. Magn Reson Med. 2008;60:934–944.

CHAPTER 5

MULTIGRADIENT DIRECTION AND LIVER IVIM

Evaluation and Minimization of the Pseudo-Hepatic Anisotropy Artifact in Liver Intravoxel Incoherent Motion (IVIM)

Oi Lei Wong, MSc, Gladys Goh Lo, MD., Jing Yuan, Ph.D., Wai Kit Chung, Wai Kong Law, Ph.D., Benny W.H. Ho, MSc and Michael D. Noseworthy, Ph.D., P.Eng.

5.1 CONTEXT OF THE PAPER

Although IVIM allows quantification of microvascular perfusion and diffusion without the use of an intravenous contrast agent, it has not been widely applied in clinical settings due to its poor reliability (47). Based on our previous liver DTI study (87), we found that the pseudo-hepatic anisotropy artifact leads to a change in DT metrics that is most pronounced in the left liver lobe. However, the effect of this artifact on IVIM metrics is not currently well understood. In this study, we hypothesized that the pseudo-hepatic anisotropy artifact mainly affects perfusion-related IVIM metrics (i.e. perfusion fraction and pseudo-diffusion coefficient). We further investigated how the IVIM fit quality is affected both by performing the IVIM fit on the data with and without averaging over multiple non-coplanar gradient directions, and the application of motion compensation.

5.2 DECLARATION STATEMENT

Oi Lei Wong, as principle author, designed the experiment, wrote the article, collected the data, performed all analysis, and created figures and tables as appropriate. Michael D. Noseworthy, as corresponding author, provided guidance and advice, and performed proofreading/editing and submission of the manuscript for publication. Dr. Gladys Lo provided clinical guidance and commentary. Jing Yuan provided guidance and advice, and performed proofreading/editing for publication. Wai Kit Chung and Benny W.H. Ho provided clinical commentary and performed the MR image acquisition.

This paper has been submitted for publication to the *Journal of Magnetic Resonance Imaging.*

5.3 PAPER

Evaluation and Minimization of the Pseudo-Hepatic Anisotropy Artifact in Liver Intravoxel Incoherent Motion (IVIM)

Oi Lei Wong, MSc[1,2,3], Gladys Goh Lo, MD.[4], Jing Yuan, Ph.D.[3], Wai Kit Chung[4], Max W.K. Law, Ph.D.[3], Benny W.H. Ho, MSc[4] and Michael D. Noseworthy, Ph.D., P.Eng.[1,2,5,6†]

[1]Department of Medical Physics and Applied Radiation Science, McMaster University, Hamilton, Ontario, Canada.
[2]Imaging Research Center, St. Joseph's Healthcare, Hamilton Ontario, Canada.
[3]Medical Physics and Research Department, Hong Kong Sanatorium & Hospital, Hong Kong Special Administrative Region (SAR), China.
[4]Intervention and Radiology Department, Hong Kong Sanatorium & Hospital, Hong Kong Special Administrative Region (SAR), China.
[5]School of Biomedical Engineering, McMaster University, Hamilton, Ontario, Canada.
[6]Department of Electrical and Computer Engineering, McMaster University, Hamilton, Ontario, Canada.

***Corresponding Author:**

Dr. Michael D. Noseworthy, Ph.D., P.Eng.

Director, McMaster School of Biomedical Engineering,

Associate Professor, Department of Electrical and Computer Engineering,

McMaster University.

Hamilton, Ontario, Canada.

email: nosewor@mcmaster.ca

voice: +1 1 (905) 925-9140 ext.32727

http://www.ece.mcmaster.ca/~mikenose/web/HOME.html

ABSTRACT:

Purpose: To evaluate the effect of the pseudo-hepatic anisotropy artifact on liver intravoxel incoherent motion (IVIM) metrics and whether the use of multiple gradient directions in the IVIM acquisition minimizes the pseudo-hepatic artifact.

Materials and Methods: Multiple breath holding and shallow free breathing IVIM scans (*b-value* = 0, 10, 20, 30, 40, 50, 100, 200, 300, 400, 500 mm^2/s) were performed on eight healthy volunteers using 1 and 6 gradient directions. Cluster analysis was carried out to separate motion-contaminated parenchyma from unaffected liver parenchyma and vessels. An observer rating test was then performed to identify the anatomical association of the resultant clusters. Non-linear motion analysis was also performed to look for a possible link between IVIM metrics and non-linear liver motion.

Results: Anatomical association between clusters and the rank of the corresponding IVIM metrics were identified. In particular, motion-contaminated parenchyma is located in the left liver lobe, where the prominent pseudo-hepatic artifact has previously been identified. A significant reduction in outliers was obtained using the data after averaging over 6 non-coplanar gradient directions and when using restricted free breathing.

Conclusion: The pseudo-hepatic anisotropy artifact can be minimized when data was averaged over multiple gradient directions and restricted depth of breathing during IVIM acquisition.

KEYWORDS:

MRI, liver, motion, intravoxel incoherent motion (IVIM).

INTRODUCTION:

Intravoxel incoherent motion (IVIM) modeling enables quantification of perfusion and diffusion effects without the use of an intravenous contrast agent. However, the original IVIM model was derived without accounting for motion and pulsation effects [1]. Although the clinical usefulness of IVIM has been reported in a few recent studies [2,3], clinical application of the technique has been hindered due to poor reliability [4]. Koh *et al.* have further concluded that the IVIM fit should be done using region of interest (ROI)-based analysis, because voxel-wise IVIM fitting leads to poor reproducibility in parametric estimation [5]. Difficulty in obtaining reliable estimations of IVIM metrics is mainly the result of three key issues: (1) the IVIM model is non-linear; (2) the sample size of diffusion weighted (DW) images (i.e. number of b-values and number of measurements per b-value) is small due to practical issues; and (3) the signal-to-noise ratio (SNR) of body DW images is low [4]. Motion is another important factor leading to signal loss and artificially elevated apparent diffusion coefficient (ADC) [6]. Due to these limitations, IVIM metrics are susceptible to both the choice of fitting strategy [7,8,9] and the motion correction algorithm [6,10,11].

Motion correction in liver IVIM scans has been done using real-time approaches (i.e. prospective), such as cardiac [6] and respiratory triggering [10], and using offline image registration (i.e. retrospective) [11]. Triggering

techniques assume the liver shape does not change and images are acquired at the same respiratory and cardiac phase. As a result, the triggering approach cannot completely remove small non-linear liver motion [6,12]. Chun *et al.* proposed the use of an MR tagging sequence to quantify liver motion during respiration [13,14]. However, the tag signal has a very short half-life in comparison to the period of the respiratory cycle. Thus, a tagging technique can only be performed using a collection of MR tagged images throughout the respiratory cycle, which potentially biases the results of liver motion assessment. More recently, liver motion evaluation has been proposed using 4D MR images and sequential deformable registration [15]. A similar image registration approach has been shown to be useful in improving results in fetal brain diffusion weighted imaging (DWI) [16] and human liver IVIM studies [6,11]. However, the deformable registration approach often involves modification of the raw DW signal. As such, validation of the non-linear motion correction is very challenging due to the absence of a gold standard [6,15]. These studies suggest caution when applying non-linear image registration in quantifying IVIM metrics.

Non-linear liver motion has been related to the pseudo-hepatic anisotropy artifact seen on DWI [12] and diffusion tensor imaging (DTI) [17]. Non-linear motion, in general, can lead to subvoxel shifts during application of the diffusion gradients, which is mis interpertated as diffusion signal [16]. Such error is composed of two components: error due to voxel shift and phase error [6]. The Although correction of the voxel shift seems to improve the IVIM fit of the

diffusion modulated MR signal [11], correction of the phase induced error is still challenging as the underlying mechanism is not clear. A better understanding of the relationship between the pseudo-hepatic anisotropy artifact and IVIM metrics should further improve IVIM parameter estimation.

In the first part of this study, we proposed that non-linear liver motion leads to an artifactual change in perfusion related IVIM fitted parameters. Based on our previous results, enhanced pseudo-hepatic anisotropy artifact was observed in the left liver lobe which suggested a possible relationship between geometric distribution and the pseudo-hepatic anisotropy artifact [17]. In addition, a lower *f* value in cirrhotic liver parenchyma was reported when compared with healthy liver parenchyma [18]. Cirrhotic liver parenchyma has been observed to be less susceptible to pseudo-hepatic anisotropy artifact. We, therefore, hypothesized that cardiac motion-contaminated liver parenchyma has higher *f* compared to motion-free liver parenchyma. Three groups of liver clusters were first identified based on a Gaussian Mixture model using the voxel-wise IVIM metric. An observer rating test was then performed to look for possible linkage between IVIM metrics and their geometric distribution. Following classification of liver regions, we identified approaches to minimize both linear and non-linear liver motion. To maintain a reasonable image acquisition time, IVIM scans were performed with multiple breath-holds and shallow free breathing instead of respiratory triggering. To compensate for the linear liver motion, offline retrospective rigid body registration was then performed, which has been reported

to result in reliable liver ADC when used in combination with free breathing [18]. We further hypothesize that pseudo-hepatic anisotropy artifact can be minimized with the use of multiple diffusion gradient directions. The best approach to minimize the pseudo-hepatic anisotropy artifact was determined based on fitting efficiency.

MATERIALS AND METHODS:

Data Acquisition

Eight healthy volunteers (1 male and 7 females, mean age ± standard deviation (years): 25.0 ± 3.0) were recruited for the study and informed consent was obtained from each participant. The study was approved by the Institutional Research Board (Hong Kong Sanatorium & Hospital, Hong Kong SAR, China). All MR scans were done at Hong Kong Sanatorium & Hospital (Hong Kong SAR, China) using a 1.5T MR scanner and a dedicated 32-channel body RF receiver array (Optima MR450w, General Electric Healthcare, Milwaukee, USA) with subjects in the supine position. For each volunteer, diffusion scans were done using identical prescan values (shim settings, center frequency, and transmit/receive gain values) and geometric prescription. To assess the effect of respiratory motion, each volunteer was instructed to repeat both the DTI and DWI acquisitions twice under multiple breath-holds and shallow free breathing. Ten sets of coronal liver DTI/DWI acquisitions, each with a range of b-values (details below), were first acquired with multiple breath-holds using a dual spin echo

echo-planar imaging (EPI) sequence (TE/TR = 77/2200ms, 6 gradient directions for the DTI acquisition and 1 gradient direction (along the left-right direction) for the DWI acquisition, 5 slices, slice thickness = 10mm, 35cm FOV, 256 x 64 acquisition matrix, zero-filled to 256x256 matrix (voxel size=10x1.4x5.5mm), 1 signal average (NSA), 18s per b-value for DTI acquisition and 7s per b-value for DWI acquisition). For the purpose of intra-scan motion evaluation, a b-value = 0 s/mm^2 image was acquired prior to each non-zero b-value scan (i.e. the order of b-values was set as 0, 10, 0, 20, 0, 30, 0, 40, 0, 50, 0, 100, 0, 200, 0, 300, 0, 400, 0, 500 s/mm^2). To achieve the same acquisition scan time equivalency (STE) while maintaining a reasonable number of breath-holds, 6 gradient directions were used in the IVIM acquisition with 1 NSA, and 1 gradient direction was used in the IVIM acquisition with 6 NSA. In total, the data was acquired under four conditions: free breathing 1 gradient direction (*FB 1dir*), free breathing 6 gradient directions (*FB 6dir*), breath-holding 1 gradient direction (*BH 1dir*) and breath-holding 6 gradient directions (*BH 6dir*).

IVIM Metrics Calculation

Registration of both free breathing and breath-holding images was done by linearly transforming the images of each acquisition to the chronologically first b=0s/mm^2 image of the first DTI/DWI acquisition of each subject. This was accomplished with the MCFLIRT utility of the FMRIB software library (FSL) package [19] (FSL 4.1, FMRIB Analysis Group, Oxford, UK). Eddy current

correction was then performed on each motion corrected acquisition using FSL. Results for all 6 repetitions of the 1 direction IVIM scans were averaged prior to further calculations. For DTI scans, results of all 6 directions were averaged over prior to metric calculation. Voxel-based IVIM metrics (perfusion fraction (*f*), pseudo-diffusion (*D**) and diffusion (*D*)) were then calculated using a custom written Matlab script (Matlab 2010a, Mathworks, Natick MA). Voxel-wise log-linear fit of the normalized signal, as a function of the b-value in the diffusion region (i.e. b-value > 200s/mm^2), was performed to estimate *D* (i.e. slope) and initial value of *f* (i.e. 1- intercept). The initial value of *D** and f were estimated using the voxel-wise log-linear fit in the perfusion region (i.e. b-value < 200s/mm^2)[5]. Similarly the initial value of D was estimated using the voxel-wise log-linear fit in the diffusion region. The following boundary conditions were placed on the initial values: $0 < f \leq 1$, $D^* \geq D$, and $D^* < 1$ mm^2/s. Finally, the values of *f* and *D** were estimated using the IVIM model and a Levenberg-Marquardt minimization algorithm, with *D* estimated using the log-linear fit from the diffusion region.

Intra-scan Motion Analysis

Intra-scan motion analysis was performed using the b = 0 s/mm^2 image acquired with each non-zero b-value scan (i.e. 10 b-value = 0 s/mm^2 images in total). **Figure 5.1** illustrates the workflow for each four-dimensional motion map. The three dimensional image of frame *n-1* was linearly transformed to frame *n*

using FMRIB's linear image registration tool (FLIRT) from FSL [20,21]. The translated frame *n-1* was then non-linearly deformed to frame *n* using FMRIB's nonlinear image registration tool (FNIRT) from FSL [22]. A corresponding warp field map, which contained the voxel-wise translational information in the x, y, and z directions, was generated. To generate the three-dimensional translation profile for each voxel, the voxel index was adjusted based on the translational information from the field map of the pervious time point (i.e. $(x_i, y_i, z_i)_n = (x_i,y_i,z_i)_{n-1} + (\Delta x_i, \Delta y_i, \Delta z_i)_{n-1}$). The variation of the deformable motion during the scan was quantified using the standard deviation of the one-dimensional motion (i.e. left-to-right (LR), superior-to-inferior (SI) and anterior-to-posterior (AP)) of each voxel.

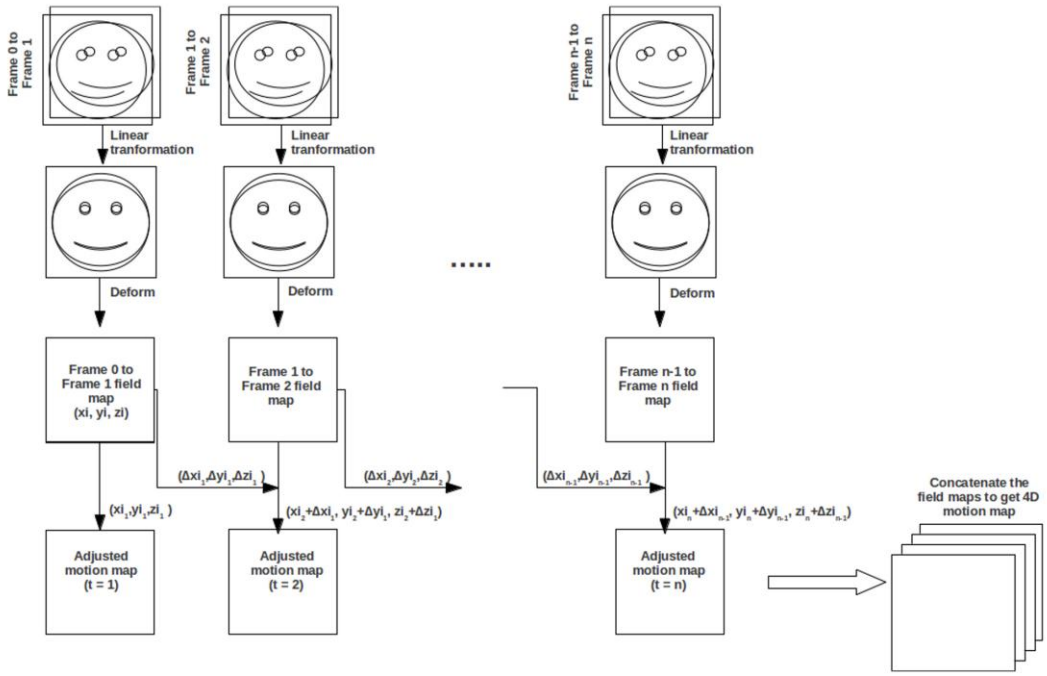

Figure 5.1: *Workflow of intra-scan motion analysis. The linear mismatch between frame n-1 and frame n was first removed using rigid body transformation. To estimate the non-linear motion of the liver during the scan, minor adjustment was performed based on the displacement from the frame of the previous time point.*

Statistical Analysis

An ROI of the whole liver was selected on the chronologically first b-value = 0 s/mm^2 image using the T_2 anatomical image as a guide (**Figure 5.2**). Based on the calculated *f* and *D** values within this liver ROI, voxels with *D** ≥ 1000 x 10^{-3} mm^2/s, *f* < 0 or *f* > 1 were first categorized as outliers. A four-dimensional Gaussian mixture model was then applied to the remaining voxels within the liver ROI (the four dimensions corresponded to the three IVIM metrics (*D*, *D** and *f*) and the sum of residual squares, the goodness of fit obtained from

the voxel-wise IVIM fit). Three binary cluster maps for each of the four conditions (*FB 1dir*, *FB 6dir*, *BH 1dir*, *BH 6dir*) were then generated. Sample cluster maps and their corresponding histograms are illustrated in **Figure. 5.2**.

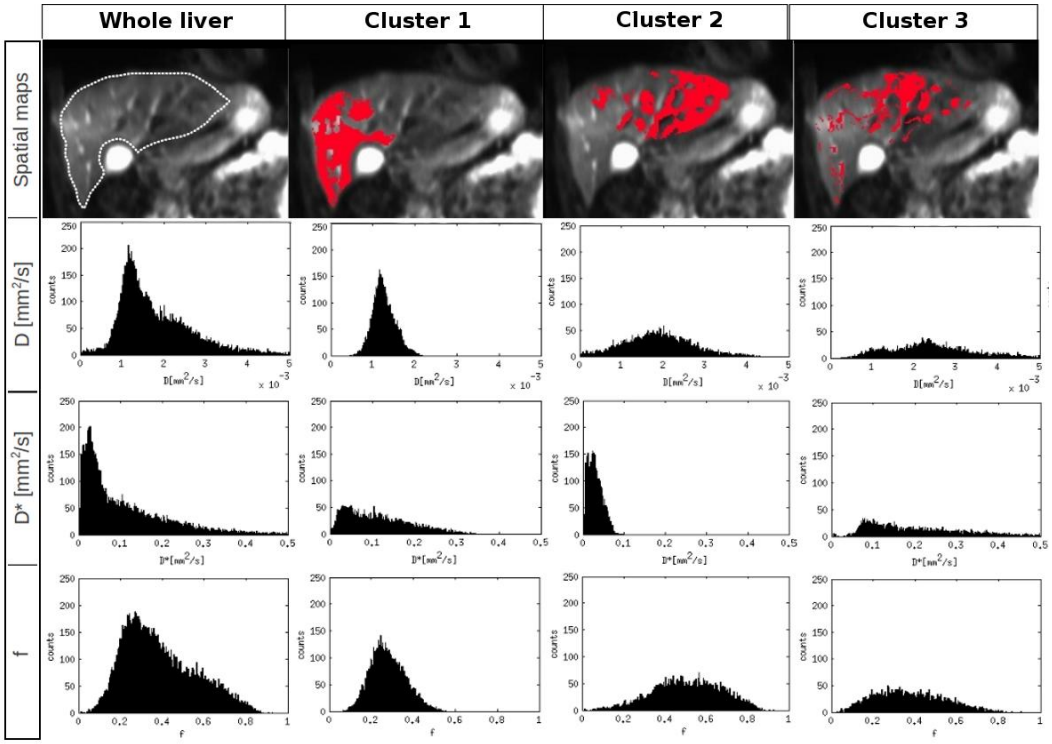

Figure 5.2: *Binary maps and histograms of IVIM metrics (rows from top to bottom) over the whole liver, and the 3 resultant clusters obtained from the 4 dimensional Gaussian distribution model. The binary maps denoted the spatial distribution of these clusters. The majority of voxels were found in the right liver lobe, left liver lobe and vessels, respectively, for resultant cluster 1 to 3.*

The categorization results obtained using the 4-dimensional Gaussian Distribution model provide no indication on the anatomical location of the resultant clusters (for example, cluster 1 may be mainly located in the right liver for subject A but located in the left liver lobe for subject B). Although the anatomical location of each of the three resulting clusters can be identified manually using the binary map generated for each resultant cluster, this is a

practical approach only for single subject analysis. However, if one wanted to do group analysis, an alternative approach to identify the spatial distributions of the resultant clusters is necessary. In this study, non-linear liver motion is hypothesized to lead to elevated perfusion related IVIM metrics. As such, right liver lobe should be associated with the cluster exhibiting the lowest f and D^* values. However, the most effective IVIM metric for reliable spatial identification is not known. We, therefore, evaluated the performance of each IVIM metric in the identification of the anatomical association using the observer rating test. For each liver, each of the three binary cluster maps was first non-parametrically categorized according to the rank of their (1) median f value (f_{low}, f_{medium} and f_{high}, respectfully), (2) median D^* value, classified as low medium and high clusters (i.e. D^*_{low}, D^*_{medium} and D^*_{high}) and (3) median D value (i.e. D_{low}, D_{medium} and D_{high} clusters). The spatial distribution of each set of binary maps was then categorized by a physicist (with 5 years of experience in analyzing DTI and liver MRI) as the right liver lobe, left liver lobe or vessels. For each IVIM metric, the total score for each tissue type was summed prior to the observer rating calculation (defined as percent total score of a particular tissue type over total number of binary masks in the corresponding category). As an example using data from the f_{high} category and *BH 6dir* experimental condition (**Table 5.1**), a score for each binary map in the f_{high} category (There are 8 volunteers in this study, thus 8 maps in total for each category), the total scores for right liver lobe, left

liver lobe and vessels were calculated to be 0, 2 and 6, respectively. Thus, the corresponding observer ratings were 0% (i.e. 0/8 × 100% = 0%), 25% and 75%.

For the rest of the statistical analysis, the binary cluster maps were categorized according to their median *f* value. The percent volume fraction (number of voxels within each cluster over the total number of voxels in the whole liver calculated as a percentage) was determined for each volunteer. A sign-rank test was then performed on the calculated IVIM metrics to assess for any statistical difference between the five defined groups (i.e. whole liver, outlier, low f_{low}, f_{medium} and f_{high} clusters). Statistical comparison between the IVIM metrics obtained from the four defined conditions (i.e. *FB 1dir*, *FB 6dir*, *BH 1dir* and *BH 6dir*) was also performed using a sign-rank test. The statistical evaluation of percent volume fraction and one-dimensional motion standard deviation was performed using the same pipeline as previously described using IVIM metrics. All statistical analyses were performed using Matlab.

RESULTS:

The anatomical relationship between each cluster and the rank of the IVIM metrics (*D*, *D** and *f*) is shown using the observer rating (**Table 5.1)**. For all choices of gradient directions and both motion compensation approaches (free and restricted breathing), the maximum observer rating was always noted in the D_{low}, D^*_{medium} and f_{low} categories of the right liver lobe (**Table 5.1**). For the left liver lobe, the maximum observer rating was consistently obtained in the D_{medium}, D^*_{low}

and f_{high} categories (**Table 5.1**). Furthermore, 100% of the f_{low} category was rated as the right liver lobe using the *FB 1dir* and *FB 6dir* IVIM acquisitions.

Table 5.1: *Observer rating of each tissue for each category. The largest observer rating (in red boxes with yellow highlights) corresponds to a higher frequency of a particular tissue type rated by the observer.*

label	category	observer rating			category	observer rating			category	observer rating		
		Right Lobe	Left Lobe	vessel		Right Lobe	Left Lobe	vessel		Right Lobe	Left Lobe	vessel
BH, 1dir	D_{low}	75	12.5	12.5	D^*_{low}	12.5	50	37.5	f_{low}	87.5	0	12.5
	D_{medium}	25	62.5	12.5	D^*_{medium}	62.5	37.5	0	f_{medium}	12.5	25	62.5
	D_{high}	0	25	75	D^*_{high}	25	12.5	62.5	f_{high}	0	75	25
BH, 6dir	D_{low}	87.5	12.5	0	D^*_{low}	12.5	75	12.5	f_{low}	62.5	0	37.5
	D_{medium}	12.5	50	37.5	D^*_{medium}	87.5	12.5	0	f_{medium}	37.5	25	37.5
	D_{high}	0	37.5	62.5	D^*_{high}	0	12.5	87.5	f_{high}	0	75	25
FB, 1dir	D_{low}	75	25	0	D^*_{low}	25	75	0	f_{low}	100	0	0
	D_{medium}	25	62.5	12.5	D^*_{medium}	75	25	0	f_{medium}	0	25	75
	D_{high}	0	12.5	87.5	D^*_{high}	0	0	100	f_{high}	0	75	25
FB, 6dir	D_{low}	100	0	0	D^*_{low}	25	75	0	f_{low}	100	0	0
	D_{medium}	0	87.5	12.5	D^*_{medium}	75	12.5	12.5	f_{medium}	0	12.5	87.5
	D_{high}	0	12.5	87.5	D^*_{high}	0	12.5	87.5	f_{high}	0	87.5	12.5

Table 5.2: *IVIM metrics (f, D* and D) for each group of cluster (i.e. f_{low}, f_{medium}, f_{high}, outlier and whole liver) using IVIM scans under each of the 4 conditions (1dir BH, 6dir BH, 1dir FB and 6dir FB). Significant results are highlighted in yellow. * indicates significantly different from whole liver, # denotes significant difference compared to the f_{low} cluster, & denotes significantly different from the f_{medium} cluster, ♣ denotes significant difference between 1 and 6 gradient directions, § indicates significantly different between FB and BH (Significance was set to $p<0.05$ for all comparisons).*

label	category	f median (min,max)	D* [x10^{-3} mm^2/s] median (min,max)	D [x10^{-3} mm^2/s] median (min,max)
BH, dir1	f_{low}	0.22 (0.16, 0.28)*&♣	99.7 (22.2, 250.4)	1.21 (1.00, 2.17)
	f_{medium}	0.31 (0.24, 0.41)*#	86.4 (27.8, 187.3)	1.48 (1.08, 2.27)
	f_{high}	0.41 (0.33, 0.56)*#&	28.1 (18.4, 86.7)	1.41 (0.96, 1.83)
	outlier	0.17 (0.13, 0.26)*#&	1552.1 (1447.7, 2214.4) *#&	1.65 (1.32, 2.24) *#
	whole liver	0.26 (0.22, 0.36)#&	75.6 (31.1, 125.5)	1.36 (1.12, 1.51)
BH, dir6	f_{low}	0.27 (0.22, 0.34)	101.4 (31.2, 144.2)	1.28 (1.02, 2.11)
	f_{medium}	0.33 (0.30, 0.38)#	86.1 (27.8, 162.0)	1.49 (0.89, 2.10)
	f_{high}	0.42 (030, 0.60)*#&	23.0 (14.2, 245.2)§	1.30 (0.79, 2.62)
	outlier	0.19 (0.14, 0.34)*#&	1677.1 (1508.3, 3786.5)*#&	1.52 (1.41, 2.78) *
	whole liver	0.28 (0.22, 0.39)	44.7 (36.9, 349.2)	1.30 (1.02, 1.49)
FB, dir1	f_{low}	0.25 (0.18, 0.28)*&	67.3 (16.2, 133.5)	1.21 (1.11, 1.57) *
	f_{medium}	0.30 (0.24, 0.38)*#	154.5 (11.9, 209.0)#	1.82 (1.11, 3.01) #
	f_{high}	0.44 (0.34, 0.60)*#&	39.4 (12.9, 145.4)♣	1.87 (1.05, 2.68) #
	outlier	0.18 (0.15, 0.27)*#&	1598.8 (1478.1, 2229.5)*#&	1.79 (1.67, 2.64) *#
	whole liver	0.28 (0.21, 0.34)#&	95.7 (24.9, 157.4)	1.46 (1.30, 2.02) #
FB, dir6	f_{low}	0.24 (0.18, 0.29)*&	64.0 (20.0, 133.7)	1.21 (0.98, 1.76) *
	f_{medium}	0.31 (0.23, 0.40)*#	150.9 (22.7, 100.3)*#&	2.12 (1.24, 2.95) *#
	f_{high}	0.41 (0.34, 0.51)*#&	37.4 (20.7, 100.3)*#&	1.62 (1.19, 2.00) *#
	outlier	0.21 (0.09, 0.33)*&	1515.1 (1347.8, 2964.0)*#&	1.83 (1.59, 2.51) *#
	whole liver	0.28 (0.22, 0.37)&	68.2 (24.6, 126.8) &	1.39 (1.17, 1.97) #&

Table 5.2 illustrates the median of *f*, *D* and *D** for each ROI (obtained from the binary map from clustering) in each condition (i.e. *BH 1dir*, *BH 6dir*, *FB 1dir* and *FB 6dir*). Compared with *BH 6dir*, a significant reduction was noted for the *BH 1dir f* value in the f_{low} cluster ($p<0.05$). A significantly lowered *f* value was also observed in the outlier group compared to the f_{low}, f_{medium}, f_{high} and whole liver groups using *BH 1dir*, *BH 6dir* and *FB 1dir* ($p<0.05$). When compared to

the f_{medium} and whole liver groups, a significantly smaller *FB 6dir f* value was noted in the outlier group (p<0.05). In addition, a reduced *BH 1dir f* value was seen in the f_{low} and outlier groups compared to the *BH 1dir f* value of the whole liver group (p<0.05). Relative to the *BH 1dir f* value of the f_{medium} and f_{high} groups, a significantly reduced *BH 1dir f* value was observed in the whole liver group(p<0.05). A similar trend was also seen in the *FB 1dir f* value and the *FB 6 dir f* value, where a smaller *f* value was observed in the f_{low} and outlier groups compared to the corresponding value of the whole liver (p<0.05). In addition, a large *f* value was noted in the f_{medium} and f_{high} groups compared with the corresponding values of the whole liver group under the *FB 1dir* and the *FB 6dir* conditions (p<0.05). The *f* value of the *BH 6dir* of the whole liver group was significantly larger than the corresponding *f* value of the f_{medium} and f_{high} groups (p<0.05). In the f_{low} group and for all four experimental conditions, a significantly lower *f* value was observed when comparing with the corresponding value in the f_{medium} and f_{high} groups (p<0.05). The estimated *f* value of the f_{low} group was significantly larger than that of the *BH 1dir* outlier group, the *BH 6dir* outlier group and the *FB 1dir* outlier group (p<0.05).

In the high *f* cluster, a larger *FB 1dir D** value was observed compared to the *FB 6dir D** value (p<0.05). In addition, an increased *BH 6dir f* value was noted compared to the *FB 6dir f* value (p<0.05). For all four conditions, the *D** value of the outlier cluster was significantly higher than the *D** value of the f_{low}, f_{medium}, f_{high}, and whole liver groups (p<0.05). A significantly higher *FB 6dir D**

value was also observed in the f_{medium} cluster compared to the f_{high}, f_{low}, and whole liver groups (p<0.05). Moreover, the *FB dir1 D** value of the f_{medium} cluster was significantly larger than that of the f_{low} cluster (p<0.05).

The *D* value of the outlier group was noted to be larger than that of the whole liver group for all four conditions (p<0.05). In contrast, a lower *D* value was observed in the outlier group when comparing the f_{low} cluster for the *BH 1dir*, *FB 1dir* and *FB 6dir* scans (p<0.05). Comparing the f_{low} group with the f_{medium}, f_{high}, and whole liver groups, a significantly smaller *D* value was obtained in the *FB 1dir* and *FB 6 dir* conditions. A significantly larger *FB 6 dir D* value was observed in the f_{medium} and f_{high} groups when comparing with the whole liver ROI (p< 0.05).

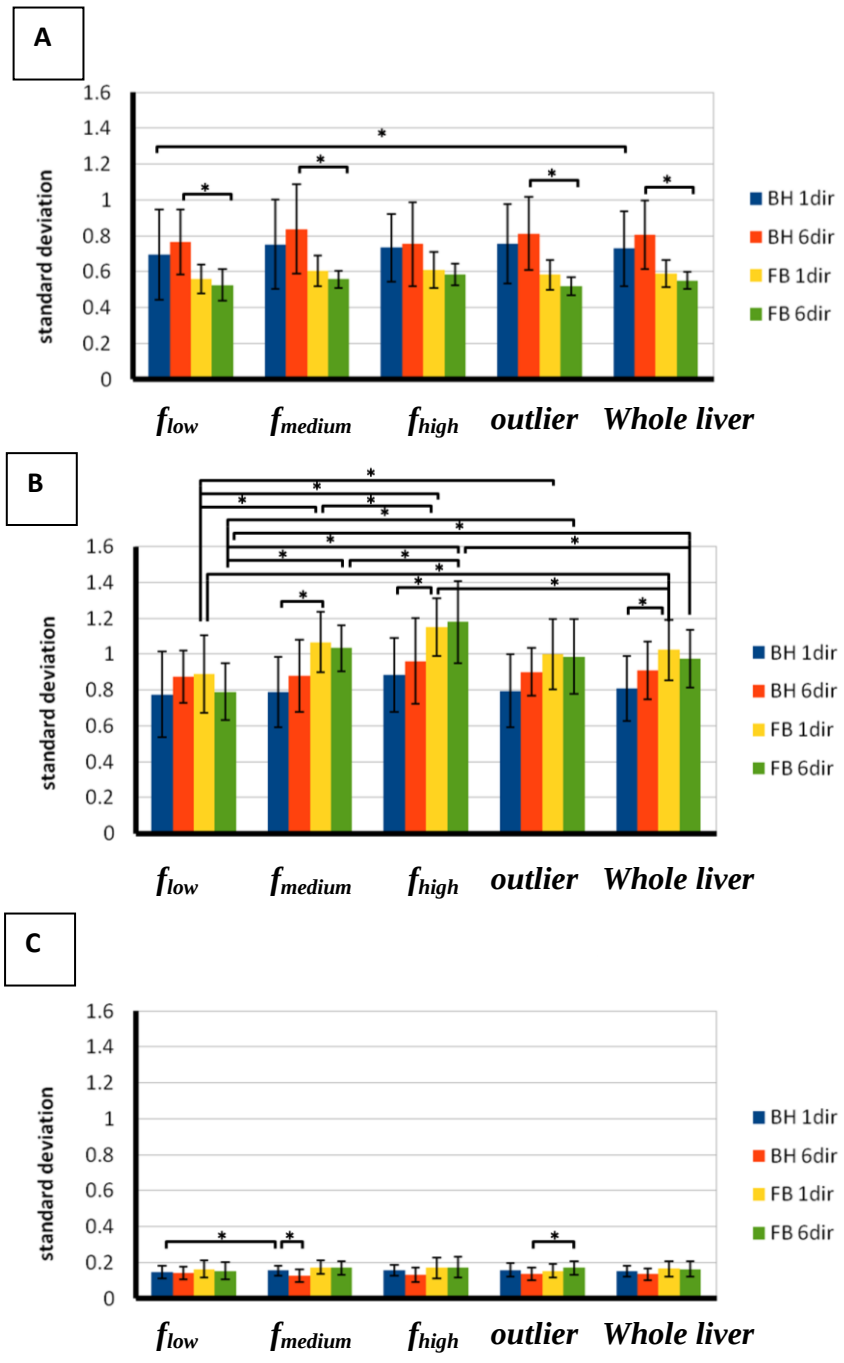

Figure 5.3: *Standard deviation of the non-linear deformation of the liver during IVIM scans along the various directions (A) left-right (LR), (B) superior-inferior (SI) and (C) anterior-posterior (AP) directions. * denotes $p<0.05$.*

As shown in **Figure 5.3**, a significantly elevated standard deviation (SD) was noted along the left-right (LR) direction in the *BH 6 dir* of the f_{low}, f_{medium}, outlier, and whole liver groups compared to the *FB 6dir* scans ($p<0.05$). The SD of the non-linear liver motion along the LR direction in f_{low} clusters was significantly smaller than that of the whole liver using the *FB 1dir* scan ($p<0.05$). Significantly elevated SD was also noted along the superior-inferior (SI) direction in the f_{medium}, f_{high}, and whole liver ($p<0.05$) groups in the *FB 1dir* scan. The SD of the non-linear motion was found to be reduced along the SI direction in the f_{low} cluster relative to that of the f_{high}, f_{medium}, outlier and whole liver cluster using the *FB 1dir* and *FB 6dir* acquisitions ($p<0.05$). In the f_{high} cluster, a significantly higher non-linear motion SD was noted along the SI direction compared to that of f_{medium} cluster for both the *FB 1dir* and *FB 6dir* conditions ($p<0.05$). Along the anterior-posterior (AP) direction, the SD of the non-linear motion was found to be significantly lower in the *BH 6dir* scan relative to the corresponding free breathing scan ($p<0.05$). The f_{medium} clusters showed significantly lower SD of non-linear motion along the AP direction than the f_{low} clusters ($p<0.05$) using *BH 1dir* scans. Finally, in relation to the results from the 6 gradient directional scans, a larger SD of non-linear displacement along the AP direction was observed in the f_{medium} clusters ($p<0.05$) using the *BH 1dir* condition.

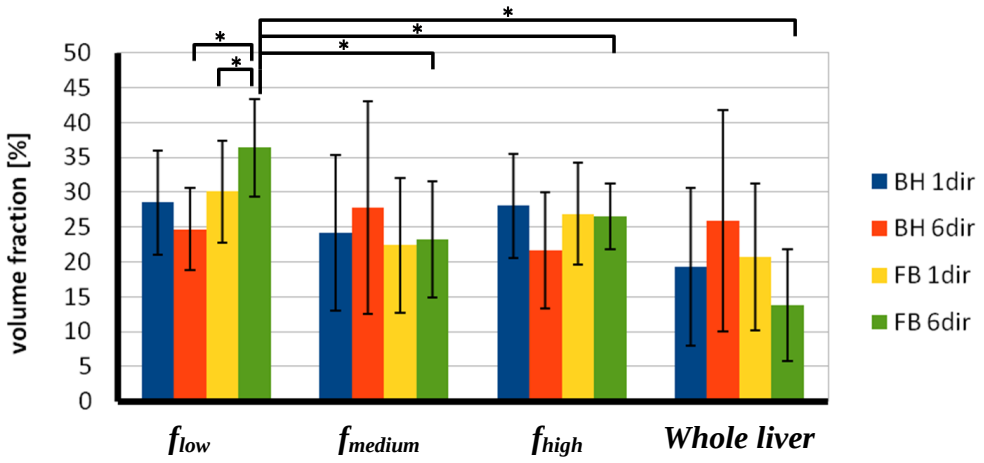

Figure 5.4: *Percent volume fraction of the f_{low}, f_{medium}, f_{high} and outlier cluster. Significantly lowered FB 6dir percentage volume fraction was observed in the outlier, high f and medium f clusters. This suggests that 6 gradient direction IVIM scans could be useful in improving the robustness of the IVIM fit. * denotes P< 0.05.*

As shown in **Figure 5.4**, a significantly higher percent volume fraction was obtained in the f_{low} cluster when comparing with the f_{medium}, f_{high}, and outlier groups (p<0.05). Under shallow free breathing, the percent volume fraction was found to be low in the f_{low} group using the *BH 6dir* scan (p<0.05). For the 6 gradient-direction acquisitions, the f_{low} cluster showed significantly lower percent volume fraction using the *FB 1dir* scan (p<0.05).

DISCUSSION:

Based on our previous work, non-linear liver motion resulting from respiration and cardiac contractility leads to a pseudo-hepatic anisotropy artifact [17]. Furthermore, the pseudo-hepatic anisotropy artifact is more pronounced in the left liver lobe due to its close proximity to the heart [12,23]. The magnitude of this non-linear liver motion is small compared to bulk cardiac and respiratory motion. Furthermore, a lower value of *f* value was reported in cirrhotic liver parenchyma, (which is through to be less sensitive to pseudo-hepatic anisotropy artifact [12]) when compared with healthy liver parenchyma [18]. We, therefore, assumed that IVIM metrics are susceptible to pseudo-hepatic anisotropy artifact. We further hypothesized that the right liver lobe should show the lowest value of *f* among these three tissue regions. The motion contaminated liver parenchyma, on the other hand, was hypothesized to be located in the left liver lobe. Based on our observer-rating test, a strong relationship was noted between the spatial distribution and the IVIM metrics (**Table 5.1**). Cluster maps with the lowest *f* were often found in the right liver lobe, while the highest was typically localized to the left liver lobe (**Table 5.1**). Most importantly, our observed spatial distribution in the left liver lobe was found to agree with our previous observation that the pseudo-hepatic artifact is most pronounced in the left liver lobe [17].

For the purpose of this study, clustering of liver pixels was performed while assuming the IVIM metrics were composed of only three groups that were each Gaussian distributed. The effect of further statistical analysis, such as the

calculation of the Akaie information criterion (AIC) or the Bayesian information criterion (BIC), on the choice of Gaussian mixture distribution (using different number of groups) was not investigated. Since our sample size was relatively small, the choice of a model based on AIC or BIC comparisons was assumed inappropriate due to high likelihood of non-reliable clustering [24]. In addition, based on our results, the observer rating test was found to be powerful enough in revealing the relationship between the anatomical information and the IVIM metrics. If our assumption of the number of tissue types was incorrect, the observer rating of all tissue types would be expected to be very close to one another. Since this was not the case, our assumption of the number of tissue types in the liver was believed to be appropriately selected.

Our IVIM metrics (f, D^* and D) of the f_{low} cluster (f = 0.22 to 0.27, D^*=64.0 to 101.4 x10^{-3} mm^2/s, D=1.21-1.28 x10^{-3} mm^2/s for all 4 conditions) were similar to those previously reported [9] . In addition, D for the f_{high} cluster (D=1.30 to 1.87x10^{-3} mm^2/s for all 4 conditions) and f_{medium} cluster (D=1.48 to 2.12 x10^{-3} mm^2/s for all 4 conditions) were close to those in the literature [2,9]. Yamada *et al.* reported f as 0.29±0.14 and D = 0.76±0.27 x 10^{-3} mm^2/s in healthy human liver using a breath hold IVIM acquisition [2]. Dyvorne *et al.* reported 0.12±0.04 for f, 73.2±34.4 x 10^{-3} mm^2/s for D^* and 1.08±0.14 x 10^{-3} mm^2/s for D in healthy volunteers using free breathing IVIM scans [9]. The use of 2D navigator IVIM scans was found to lead to values of f = 0.12±0.6, D^* = 61.1±24.1 x 10^{-3} mm^2/s and D = 1.02±0.09 x 10^{-3} mm^2/s by the same research group [9].

Since the f_{low} cluster was correlated with the right liver lobe based on our observer rating test, the agreement between our results and the literature results further confirmed our hypothesis (i.e. the right liver lobe had the lowest rank in terms of the *f* value). Not surprisingly, our *f* and *D** values for f_{high} (*f* = 0.41 to 0.44, *D** = 23.0 to 39.4 x10^{-3} mm^2/s) and f_{medium} (*f* = 0.30-0.31, *D** =86.1-154.5 x10^{-3} mm^2/s) cluster groups were found to be different from those available in the literature, most likely due to the following reasons. First, the literature results are often done based on selection of an ROI from within the right liver lobe, which has been associated with the f_{low} cluster based on our observer rating test. Thus, IVIM metrics from the f_{low} cluster should be close to the previous reported results. Secondly, the f_{high} and f_{medium} clusters correspond to vessels and the left liver lobe. These regions are typically not selected in literature studies, hence such *f* and *D** values are not reported. Based on our hypothesis, however, higher *f* and *D** values should be observed in the condition with prominent non-linear liver motion. Compared to breath-holding acquisition, liver motion is assumed larger during free breathing acquisition. In fact, significant lower D* was observed in the f_{high} cluster using *FB 6 dir* experimental condition ($p < 0.05$) when compared to *FB 1 dir* experimental condition. This observation, thus, supports our hypothesis that the application of multiple non-coplanar diffusion encoding gradients may minimize the pseudo-hepatic anisotropy artifact.

Even though bulk motion was previously assumed completely removed using a combination of breath holding and linear registration techniques [11], our

motion analysis results showed that residual motion was still present, even after applying these methods. For scans acquired while breath holding, non-linear motion lead to a large variation along the LR direction, while a small variation was observed along the SI direction. This is unusual given the fact that maximal motion during free breathing is always in the SI axis [25]. This was most likely due to two main issues. (1) The use of an asymmetric voxel size (1.4mm along the SI direction and 5.5mm along LR) to achieve a reasonable scan time for the breath holding experimental conditions. In the hope of more accurately estimating the deformation along the SI direction (thought to be most prominent), images were acquired with a resolution of 1.4mm. However, resolution differences along LR, AP and SI direction could conceivably introduce different levels of uncertainty and, thus, biasing motion analysis results. (2) Anatomical mismatch of the liver between breath holds, where volunteers often showed difficulty performing multiple breath-holds at an exact amount of inspiration. This leads to a different level of liver deformation at the start of each breath holding scan. Thus, a significantly larger SD in the LR direction was observed in the breath holding scans. Since our study was done in healthy volunteers, respiratory motion can be assumed slow and periodic, as previously suggested [11]. Furthermore, respiratory liver motion is expected to be most prominent along the SI direction [11]. More importantly, our use of the non-elastic belt to limit the amplitude of the respiratory cycle, combined with rigid body motion registration, was found to be an effective strategy.

Although a larger non-linear motion variation was expected in the left liver lobe compared to the right liver lobe, such a conclusion could not be drawn based on our results. This is potentially due to the large voxel size ($10 \times 1.4 \times 5.5 mm^3$) used in our motion analysis. Based on fast-spin echo scans of liver tracking for external beam radiation, Rohlfing *et al.* reported a superior-inferior translation between inspiration and expiration ranging from 12 to 26mm and 1 to 12 mm using rigid and nonrigid registration, respectively [15]. Although the voxel size of that study ($6 \times 1.56 \times 1.56 mm^3$) was smaller than ours ($10 \times 1.4 \times 5.5 mm^3$)[15], their reported value was drawn based on a very small sample size. Further voxel size reduction in the EPI scans, on the other hand, leads to SNR reduction, longer scan time and increased geometric distortion. Although application of an isotropic voxel in DTI is ideal, the major concern focuses on bias introduced in brain fiber orientation and anisotropy assessment [26]. Unlike brain, liver has close to isotropic diffusion and is not filled with diffusion-restricted bundles. The error arises from unequal numbers of fiber tracts and directional sampling along each side of the voxel should be small in this study. Nevertheless, our motion analysis result has shown that shallow free breathing is superior to that of multiple breath-holding techniques.

Cardiac and respiratory motion induces voxel shifts and phase errors in DW images, where non-linear registration can only correct errors due to voxel shift but not the phase error [6]. In the case of liver diffusion, the motion induced phase error is related to the pseudo-hepatic anisotropy artifact and leads to

directional signal modulation [6,12,27]. Thus, it is expected that the artificially elevated perfusion seen in IVIM metrics *f* and *D**, is due to the pseudo-hepatic anisotropy artifact and that this can be minimized using multiple non-coplanar DW gradient directions. This effect is reflected in the comparison between 1 and 6 gradient direction scans using the *D** value of the f_{high} clusters (i.e. motion contaminated liver parenchyma). A similar conclusion can be drawn based on the comparison using percent volume fraction. As IVIM is used to model micro-vascular perfusion and diffusion effects, it is not surprising that arteries are included in outlier binary maps. However, the IVIM metrics, especially *D**, are susceptible to motion compensation [11]. Depending on the amount of non-linear liver motion and the image mis-registration, the IVIM fitting error may be identified as an outlier group. If the application of multiple gradient encoding directions minimizes the pseudo-hepatic anisotropy artifact, a reduction in outlier cluster size and increased size of the liver parenchyma cluster should be observed. In fact, the largest percent volume fraction was observed in the f_{low} cluster using 6 direction diffusion scans. When compared to the 1 direction scan, a significantly elevated percent volume fraction of the f_{low} clusters was also observed. The application of 6 non-coplanar gradient directions in the IVIM scans only minimized the non-linear motion, not eliminate it. Error due to misregistration could be dealt with using better motion compensation (such as through prospective gating using 2D navigator echoes and retrospective non-linear registration), and faster scanning techniques (such as multiband EPI acquisitions).

It is worth noting that the result of our cluster analysis is strongly influenced by the location and number of outlier voxels in the liver. As the Gaussian mixture model assumes each component is Gaussian distributed, the simple inclusion of outliers results in violation of this assumption. As a result, outlier voxels were removed prior to the performance of cluster analysis in this study. However, the removal of a large amount of outliers prior to cluster analysis would lead to less reliable results. This, in turn, affects the results of the non-linear motion analysis. As shown in **Figure 5.2**, the histogram of each cluster may not be Gaussian, which is particularly true for D^*. More robust clustering can potentially be done with a non-Gaussian approach, using multivariate statistical methods such as independent component analysis (ICA) and principle component analysis (PCA). These approaches may result in maps that are better segmented. For the purpose of this study, however, we only wished to identify the geometric meaning of the cluster results, while the robustness of the segmentation result was less important.

Although multiple gradient IVIM scans have been shown to be advantageous, the pseudo-hepatic anisotropy artifact is not the sole cause of poorly fitted IVIM results. Caution should also be taken in the choice of the fitting strategy. More importantly, our current technique did not fully utilize the directional information obtained. Additional parameters such as fraction anisotropy (FA) could be generated providing further insight into liver microstructure and hence possible disease assessment. As noted in the literature,

liver diseases such as cirrhosis and hepatitis, often lead to liver structural changes [28] that occur before routine MRI can detect them. The livers of cirrhotic patients are less susceptible to the pseudo-hepatic anisotropy artifact [12] most likely due to increased tissue stiffness. More research, including studies that examine IVIM model modifications, pulse sequence optimizations to include double triggering (respiratory and cardiac) and multiband EPI, should be done in the future.

CONCLUSION

In this study, we have shown that the pseudo-hepatic anisotropy artifact leads to elevated perfusion-related IVIM metrics (i.e. D^* and f). Based on our results, multiple-gradient IVIM acquisitions slightly improve the IVIM fit. Although previous studies define motion error as a combination of voxel shift and phase shift, our proposed method only tackle on the phase shift induced error. Although IVIM modeling was improved, further modification through prospective or retrospective liver motion correction, may improve fitting and as such lead to better quantification of liver tissue.

REFERENCE:

1. Le Bihan D, Breton E, Lallemand D, Aubin ML, Vignaud J, Laval-Jeantet M. Separation of Diffusion and Perfusion in Intravoxel Incoherent Motion MR Imaging. Radiology. 1988;168(2):497-505.

2. Yamada I, Aung W, Himeno Y, Nakagawa T, Shibuya H. Diffusion Coefficients in Abdominal Organs and Hepatic Lesions: Evaluation with Intravoxel Incoherent Motion Echo-planar MR Imaging. Radiology. 1999;210(3):617-23.

3. Lewis S, Dyvome H, Cui Y, Taouli B. Diffusion-Weighted Imaging of the Liver Techniques and Applications. Magn Reson Imaging Clin N Am. 2014;22(3):373-95.

4. Freiman M, Perez-Rossello JM, Callahan JM, Voss SD, Ecklund K, Mulkern RV, Warfield SK. Reliable estimation of incoherent motion parametric maps from diffusion-weighted MRI using fusion bootstrap moves. Med Image Anal. 2013;17(3):325-36.

5. Koh DM, Collins DJ, Orton MR. Intravoxel Incoherent Motion in Body Diffusion-Weighted MRI: Reality and Challenges. Am J Roentgenol. 2011;196(6):1351-61.

6. Murphy P, Wolfson T, Gamst A, Sirlin C, Bydder M. Error Model for Reduction of Cardiac and Respiratory Motion effects in Quantitative Liver DW-MRI. Magn Reson Med. 2013;70(5):1460-9.

7. Lemke A, Stieltjes B, Schad LR, Laun FB. Toward an optimal distribution of b values for intravoxel incoherent motion imaging. Magn Reson Imaging. 2011;29(6):766-76.

8. Orton MR, Collins DJ, Koh DM, Leach MO. Improved Intravoxel Incoherent Motion Analysis of Diffusion Weighted Imaging by Data Driven Bayesian Modeling. Magn Reson Med. 2014;71(1):411-20.

9. Dyvome H, Galea N, Nevers T, Fiel IM, Carpenter D, Wong E, Orton M, de Oliveira A, Feiweier T, Vachon ML, et al. Diffusion-weighted Imaging of the Liver with Multiple b Values: Effect of Diffusion Gradient Polarity and Breathing Acquisition on Image Quality and Intravoxel Incoherent Motion Parameters - A Pilot Study. Radiology. 2013;266(3):920-9.

10. Jerome NP, Orton MR, d'Arcy JA, Collins DJ, Koh DM, Leach MO. Comparison of Free-Breathing With Navigator-Controlled Acquisition Regimes in Abdominal Diffusion-Weighted Magnetic Resonance Images: Effect on ADC and IVIM Statistics. J Magn Reson Imaging. 2014;39(1):235-240.

11. Mazaheri Y, Do RKG, Shukla-Dave A, Deasy JO, Lu Y, Akin O. Motion Correction of Multi-b-value Diffusion-weighted Imaging in the Liver. Academic Radiology. 2012;19(12):1573-80.

12. Nasu K, Kuroki Y, Nakijima H, Minami M. Hepatic pseudo-anisotropy: a specific artifact in hepatic diffusion-weighted images obtained with respiratory triggering. MAGA. 2007;20(4):205-11.

13. Chun SY, Reese TG, Ouyang J, Guerin B, Catana C, Zhu X, Alpert NM, El Fakhri G. MRI-Based Nonrigid Motion Correction in Simultaneous PET/MRI. J Nucl Med. 2012;53(8):1284-91.

14. Chen Q, Mai VM, Bankier AA, Napadow VJ, Gilbert RJ, Edelman RR. Ultrafast MR Grid-Tagging Sequence for Assessment of Local Mechanical Properties of the Lung. Magn Reson Med. 2001;45(1):24-28.

15. Rohlfing T, Maurer CR, O'Dell WG, Zhong J. Modeling liver motion and deformation during respiratory cycle using intensity-based nonrigid registration of gated MR images. Med. Phys. 2004;31(3):427-32.

16. Kim DH, Chung S, Vigneron DB, Barkovich JA, Glenn OA. Diffusion-Weighted Imaging of the Fetal Brain In Vivo. Magn Reson Med. 2008;59(1):216-20.

17. Wong OL, Lo GG, Lee R, Li WW, Chan PL, Yu SK, Noseworthy MD. The effect of respiratory and cardiac motion in liver diffusion tensor imaging (DTI). J Comput Assist Tomogr. 2014;38(3):352-9.

18. Girometti R, Esposito G, Bagatto D, Avellini C, Bazzocchi M, Zuiani C. Is Water Diffusion Isotropic in the Cirrhotic Liver? A study with Diffusion-weighted Imaging at 3.0 Tesla. Acad Radiol. 2012;19(1):55-61.

19. Behrens TEJ, Woolrich MW, Jenkinson M, Johansen-Berg H, Nunes RG, Clare S, Matthews PM, Brady JM, Smith SM. Characterization and Propagation of Uncertainty in Diffusion-Weighted MR Imaging. Magn Reson Med. 2003;50(5):1077-88.

20. Jenkinson M, Bannister P, Brady M, Smith S. Improved optimization for the robust and accurate linear registration and motion correction of brain images. Neuroimage. 2002;17(2):825-41.

21. Jenkinson M, Smith SM. A global optimisation method for robust affine registration of brain images. Med Image Anal. 2001;5(2):143-56.

22. Andersson JL, Jenkinson M, Smith S. Non-linear registration, aka Spatial normalisation FMRIB technical report TR07 JA1. FMRIB Analysis Group of the University of Oxford. 2007.

23. Kwee TC, Takahara T, Niwa T, Ivancevic MK, Herigault G, Van Cauteren M, Luijten PR. Influence of cardiac motion on diffusion-weighted magnetic resonance imaging of the liver. Magn Reson Mater Phy. 2009;22(5):319-25.

24. Burnham KP, Anderson DR. Multimodel Inference Understanding AIC and BIC in Model Selection. Sociol Methods Res. 2004;33(2):261-304.

25. Noseworthy MD, Haider MA, Sussman MS, Wright GA. Free-breathing motion compensation using template matching: a technique allowing for tracer kinetic modelling of liver metastases. J Comput Assist Tomogr. 2007; 31(2):193-7

26. Soares JM, Marques P, Alves V, Sousa N. A hitchhiker's guide to diffusion tensor imaging. Front Neurosci. 2013;12(7):31

27. Taouli B, Vilgarin V, Dumont E, Daire JL, Fan B, Menu Y. Evaluation of Liver Diffusion Isotropy and Characterization of Focal Hepatic Lesions with Two single-Shot Echo-planar MR Imaging Sequence: Prospective Study in 66 Patients. Radiology. 2003;226(1):71-8.

28. Debbaut C, Segers P, Cornillie P, Casteleyn C, Dierick M, Laleman W, Monbaliu D. Analyzing the human liver vascular architecture by combining vascular corrosion casting and micro-CT scanning: a feasibility study. J. Anat. 2014;224(4):509-17.

CHAPTER 6

IVIM-DTI IN HEALTHY HUMAN LIVER

Assessment of Perfusion and Diffusion Effects in Healthy Human Liver using Combined Intravoxel Incoherent Motion and Diffusion Tensor Imaging

Oi Lei Wong, MSc, Jing Yuan, Ph.D., and Michael D. Noseworthy, Ph.D., P.Eng.

6.1 CONTEST OF PAPER

Based on our previous liver DTI (chapter 4) and multi-directional liver IVIM (chapter 5) studies, the pseudo-hepatic anisotropy artifact leads to change in both DT and IVIM metrics. This suggests that modifications in the estimate of DT and IVIM metrics may be needed. Combined IVIM-DTI has been applied to the evaluation of human kidney [62] and muscle [84], showing the combination of both methods is feasible. Both DT and IVIM metrics may provide useful information in quantitatively categorizing diseased liver. However, the analysis can be done in two ways: by performing DTI analysis prior to IVIM analysis (i.e. DTI-IVIM), or IVIM before DTI analysis. (i.e. IVIM-DTI). In this paper, we assessed both analysis approaches. The best technique was then determined using error analysis.

6.2 DECLARATION STATEMENT

Oi Lei Wong as principle author wrote the article, designed the experiment, collected the data, performed analysis and created figures and tables. Michael D. Noseworthy, as corresponding author, provided guidance and advice, and performed proofreading/editing and submission of the manuscript for publication. Jing Yuan, Ph.D. provided guidance and advice, and performed proofreading/editing for publication.

This paper has been submitted for publication to *Magnetic Resonance in Medicine.*

6.3 PAPER

Assessment of Perfusion and Diffusion Effects in Healthy Human Liver using Combined Intravoxel Incoherent Motion (IVIM) and Diffusion Tensor Imaging (DTI)

OL Wong, MSc[1,2,3] J Yuan, Ph.D.[3] and Michael D. Noseworthy, Ph.D., P.Eng.[1,2,4,5†]

[1]Department of Medical Physics and Applied Radiation Science, McMaster University, Hamilton, Ontario, Canada.
[2]Image Research Center, St. Joseph's Healthcare, Hamilton Ontario, Canada.
[3]Medical Physics and Research Department, Hong Kong Sanatorium & Hospital, Hong Kong Special Administrative Region (SAR), China.
[4]School of Biomedical Engineering, McMaster University, Hamilton, Ontario, Canada.
[5]Department of Electrical and Computer Engineering, McMaster University, Hamilton, Ontario, Canada.

***Corresponding Author:**
Dr. Michael D. Noseworthy, Ph.D., P.Eng.
Director, McMaster School of Biomedical Engineering,
Associate Professor, Department of Electrical and Computer Engineering,
McMaster University.
Hamilton, Ontario, Canada.
email: nosewor@mcmaster.ca
voice: +1 1 (905) 925-9140 ext.32727
http://www.ece.mcmaster.ca/~mikenose/web/HOME.html

ABSTRACT

Purpose: Two different analysis approaches to combine intravoxel incoherent motion (IVIM) and diffusion tensor imaging (DTI) results from healthy human liver were compared. The difference in methods was simply the order in which DTI and IVIM analysis was done (IVIM-DTI and DTI-IVIM). The better approach was determined using error analysis.

Method: Four healthy subjects were scanned using a 3T MRI. Axial liver DT images (20 diffusion encoding directions) with 15 b-values (from 0 to 500 s/mm^2) were acquired during multiple breath-holds. A Wilcoxon rank-sum test was performed to compare results using IVIM-DTI and DTI-IVIM to those obtained through typical DTI.

Results: Significantly lower liver parenchyma fractional anisotropy (FA; p<0.05), compared to the whole liver FA, was obtained using both IVIM-DTI and DTI-IVIM approaches. Both IVIM-DTI and DTI-IVIM approaches provided similar fitting robustness ($R^2 > 0.98$).

Conclusion: We demonstrate that both IVIM-DTI and DTI-IVIM approaches were feasible in the liver with breath hold (prospective) motion compensation. Both approaches minimized the pseudo-hepatic anisotropic artifact, which artificially increases liver FA, thus providing more robust quantitative values for the potential assessment of diffusive liver disease.

KEYWORDS

Diffusion tensor imaging, Intravoxel incoherent motion, liver, MRI

INTRODUCTION

Diffusion weighted imaging (DWI) is a well-established technique for assessing tissue water diffusivity that has been widely used for many clinical applications [1]. In liver imaging often directional dependency is not considered due to respiratory motion and the assumption of isotropic diffusion [2]. Although reasonable measurement of isotropic diffusion has been shown in the liver based on its hexagonal prism-shaped lobules [3], recent studies have suggested the human liver lobule can be irregular in shape [4]. When compared to pig and rodent liver, human liver lobules appear to have more irregular shapes due to reduced connective tissue content [5]. However, the work of Nasu *et al*. [6], and our recent liver DTI work [7], have shown that non-linear liver motion leads to pseudo hepatic-anisotropic artifact. This suggests directional dependency should be considered in liver DW imaging.

Incorporating rotationally invariant directional information with diffusion is done using diffusion tensor imaging (DTI). DT metrics, such as fractional anisotropy (FA) and mean diffusivity (MD), have been shown to be clinically useful in brain tissue characterization [8]. However, there have been very few publications on liver DTI. Liver DTI derived MD, but not FA, was previously reported as being significantly different, when comparing cysts, hemangiomas,

and liver metastases [9]. When taking into consideration the effect of microvascular perfusion, diffusion weighted signal was shown to be non-monoexponential [10,11,12]. As such, liver DTI results may potentially be biased when monoexponential diffusion signal behaviour is assumed. Although the microvascular perfusion effect and diffusion can both be quantified using intravoxel coherent motion (IVIM) modeling, directional dependency of the IVIM signal is rarely investigated as the spatial orientation of capillaries is generally assumed random [13].

Recently, a directional-dependent IVIM model was proposed for analysis of human kidney [14] and skeletal muscle [13]. The diffusion signal model derived by Karampinos *et al.* [13] is based on an a priori assumption that there is anisotropic distribution of skeletal muscle capillaries. However, work by Natohamiprodjo *et al.* [14] on human kidney, simplified the problem by assuming that f, D and D* share the same set of eigenvectors, estimated from monoexponential fit results. By making this assumption the minimum number of gradient directions can be reduced. A combined IVIM and DTI assessment could quantify the directional dependent diffusion and perfusion effects, and hence lead to better characterization of tissue microstructure. In this study, we proposed two different approaches in combining IVIM and DTI assessment in healthy human liver, referred to as IVIM-DTI and DTI-IVIM.

THEORY

IVIM theory hypothesizes that water DWI signal is affected by both microvascular perfusion (pseudo-diffusion) and true diffusion. Based on this assumption, water DWI signal can be described using a two compartment bi-exponential model [15]:

$$S/S_0 = f\, e^{-bD} + (1 - f e^{-b(D+D^*)} \quad [1]$$

where S is the measured signal at a chosen b-value, S_0 is the signal without diffusion weighting, b is the diffusion weighting (i.e. b-value), f is the capillary perfusion fraction, D^* is the pseudo-diffusion coefficient and D is the true diffusion coefficient. Such a model is sufficient for single direction diffusion encoding, or even for 3 directional diffusion weighted imaging (DWI). In the latter, typical calculation of D, D^* and f are done through averaging each parameter obtained from the 3 diffusion gradient encoded directions. However, when diffusion is encoded as a tensor, one now has two approaches to analysis, that of performing tensor analysis separately for each b-value and then subsequent calculation of the IVIM parameters using the scalar values obtained from the tensor (here called DTI-IVIM). Alternatively one could calculate IVIM parameters (i.e. multiple b-values for each encoded gradient direction) with subsequent tensor analysis resulting in tensor representation of D, D^* and f (i.e. IVIM-DTI model). The latter approach, so called three-dimensional IVIM model,

involves the estimation of three rank two tensor matrices (*f*, *D* and *D**), corresponding to 18 degrees of freedom.

IVIM-DTI

The IVIM-DTI approach estimates the eigenvalues of *D*, *D** and *f* from the IVIM fitted metrics. In biological systems, water diffusion is restricted due to the presence of tissue structures such as cell membrane. Direction of true water diffusion and capillary blood flow are dependent on tissue structures but not on b-value and fitting model. Furthermore, Koh *et al.* defined the freely mobile water diffusion region to be from b-values larger than 100 s/mm^2 and flow related perfusion at b-values smaller than 100 s/mm^2 [12]. For these reasons, the estimated eigenvectors within the perfusion region from a standard DTI model are equal to the unit eigenvectors of *f*. Eigenvalues of *D*, *D** and *f* for IVIM-DTI can be estimated graphically using peanut plots, as suggested by Notohamiprojo *et al.* [14], where individual diffusivity is the projection of the eigenvectors on the diffusion-encoding gradient directions [16]. This method is impractical for voxel-wise analysis since data analysis can be tedious and time consuming. Consequently, we propose an alternative method to solve these eigenvalue sets.

The true diffusion D fitted from each gradient direction can be expressed using the following relationship [16]:

$$D = \lambda_1(\nu\cdot\varepsilon_1)^2 + \lambda_2(\nu\cdot\varepsilon_2)^2 + \lambda_3(\nu\cdot\varepsilon_3)^2 \qquad [2]$$

where ν denotes the employed unit vector of the gradient encoding direction, ε_1, ε_2 and ε_3 are the DT eigenvectors, and λ_1, λ_2, and λ_3 the corresponding

eigenvalues. In this case, ε_1, ε_2 and ε_3 can be estimated using a conventional DTI approach. A bi-exponential IVIM fit allows estimation of *D*. The unit vector of each diffusion-encoding gradient (ν) is encoded by the MR scanner. In order to estimate diffusivity eigenvalues (λ_1, λ_2, and λ_3), the inverse matrix in equation [3] must exist:

$$\begin{bmatrix}\lambda_1\\ \lambda_2\\ \lambda_3\end{bmatrix} = \begin{bmatrix}(\nu_{diri}\bullet\varepsilon_1)^2 & (\nu_{diri}\bullet\varepsilon_2)^2 & (\nu_{diri}\bullet\varepsilon_3)^2\\ \vdots & \vdots & \vdots\end{bmatrix}^{-1}\begin{bmatrix}D_{diri}\\ \vdots\end{bmatrix} \quad [3]$$

As the inverse matrix does not exist in our case, modification of **equation [3]** is done using an approximated Moore-Penrose pesudoinverse, which has been applied in calculation of conductivity tensors for brain DTI [17]. Similarly, the estimation of λ_{1f}, λ_{2f}, and λ_{3f} (eigenvalues of *f*) can be done by assuming **equation [4]** is valid:

$$f = \lambda_{1f}(\nu\cdot\varepsilon_{1f})^2 + \lambda_{2f}(\nu\cdot\varepsilon_{2f})^2 + \lambda_{3f}(\nu\cdot\varepsilon_{3f})^2 \quad [4]$$

Since the direction of capillary blood flow and true water diffusion depends on tissue structure, the tensor describing perfusion fraction and true diffusivity should share the same set of ν values (i.e. gradient magnitudes in x, y and z). Thus, the proposed IVIM-DTI approach allows estimation of a 3 dimensional IVIM model using a minimum of three sets of 6 direction IVIM scans.

DTI-IVIM

In this approach, the eigenvalues of *D* and *f* of a tensor based IVIM model are estimated using the eigenvalues generated from conventional DTI analysis.

Here, the direction of capillary blood flow and true water diffusivity are assumed independent of b-value. As such, eigenvalues of each b-value calculated using standard DTI analysis are projected onto orthogonal Cartesian axes. As a result, three sets of normalized signal (S/S_{01}, S/S_{02} and S/S_{03}) as a function of b-value, each weighted along one of the principle axes, can each be calculated using the Stejskal-Tanner equation for diffusivity. Eigenvalues of D, D^* and f are then obtained directly from the IVIM fit on S/S_{01}, S/S_{02} and S/S_{03}.

METHODS

Data Acquisition

Four healthy volunteers (2 male and 2 female, mean age of 27 ± 6 years) were recruited and informed consent was obtained from each. The study was approved by the Research Ethics Board of St. Joseph's Healthcare (Hamilton, Ontario, Canada) prior to the study.

All scans were done at St. Joseph's Healthcare (Hamilton, Ontario, Canada) using a 3T MRI scanner and a dedicated 32 channel body RF receiver array (Discovery MR750, General Electric Healthcare, Milwaukee, USA) with subjects in a supine position. All imaging was performed during breath holding. Fourteen sets of axial liver DTI acquisitions, each at a different b-value setting, were acquired using a dual spin echo, echo planar imaging (EPI) sequence (TE/TR = 77/1600ms, 20 gradient directions, 16 slices, slice thickness = 10mm, 35cm FOV, 110 x 110 matrix, 35s per b-value setting per average). 15 b-value

settings were chosen to be 0, 10, 15, 20, 25, 30, 35, 40, 45, 50, 100, 200, 300, 400 and 500 s/mm^2. In total three separately acquired DTI datasets (i.e. averages) were performed for each b-value setting (i.e. 42 liver DTI scan per volunteer in total). All scans were done using identical prescan settings (shim settings, center frequency, and transmit/receive gain values) and geometric prescription. Motion and eddy current correction was done prior to summation of the three scans, making the end result effectively a three-averaged acquisition.

Image Analysis

Although respiratory motion was compensated for by breath holding, linear registration was still performed. Registration was done by linearly transforming images of each acquisition to the chronologically first b = 0 s/mm^2 image of the first DTI acquisition of each subject. This was accomplished with the MCFLIRT utility of FSL [18] (FSL 4.1, FMRIB Analysis Group, Oxford, UK). Eddy current correction was then performed on each motion corrected acquisition using FSL and the results were averaged. Then DTI calculations were performed for each of the 15 b-values using FDT plug-in of FSL.

IVIM-DTI computation method

All IVIM-DTI metrics were calculated using a custom Matlab script (Matlab 2010a, Mathworks, Natick MA). DT metrics, determined using FSL based on a monoexponential fit, was done to estimate unit eigenvectors from both the perfusion region (b = 0, 50 s/mm^2) and diffusion region (b = 0, 500 s/mm^2). The voxel-wise eigenvalues of f and D were estimated using the method described

previously in the theory section. Accordingly, the spherical shape of diffusion and pseudo-perfusion fraction (i.e. *FA* and FA_f) and the mean diffusion and pseudo-perfusion fraction (i.e. *MD* and *Mf*) were determined.

DTI-IVIM computation method

DTI metrics were first calculated using the FDT plug-in of FSL using each of the 14 b-values (i.e. 0 and 10, 15, 20, 25, 30, 35, 40, 45, 50, 100, 200, 300, 400 and 500 s/mm^2), each based on a monoexponential fit. Based on the method described in the theory session *FA*, FA_f, *MD* and *Mf* were calculated for each liver using the fitted eigenvalues of *D* and *f*.

Statistical Analysis

Statistical analysis was performed using a region of interest (ROI) drawn on the b-value = 0 s/mm^2 image. Besides the selected ROI of the whole liver, two smaller ROIs, one on right lobe liver parenchyma the other on a large hepatic blood vessel, were also analyzed to determine the extent of confounding due to blood flow (**Figure 6.1**). Monoexponential fitting, through all 15 b-values, was used as a reference for comparing improvement in quality of calculated IVIM-DTI and DTI-IVIM metrics. Comparisons for each ROI were performed using a Wilcoxon rank sum test. The fitting performance of the two bi-exponential approaches (i.e. IVIM-DTI and DTI-IVIM) and monoexponential approach were also evaluated based on the adjusted R^2, each fitted to the same set of diffusion signal averaged between subjects and voxel with in the whole liver ROI.

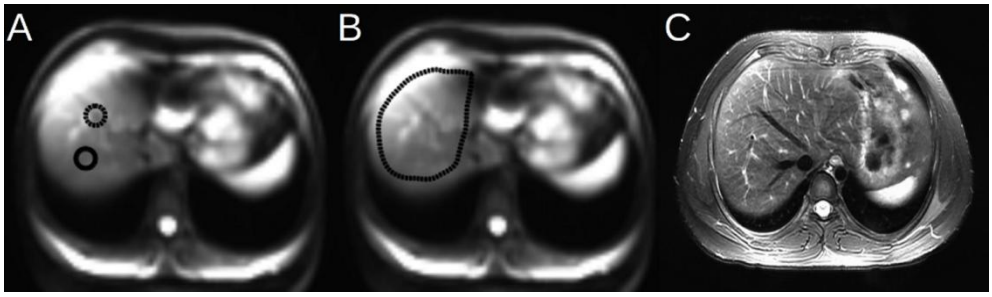

Figure 6.1: *Locations of regions of interest (ROIs). (A) Selection of small ROIs on the b=0 mm^2/s image for determining degree of blood flow associated confounding, where the upper circle contains hepatic blood vessels and the lower one does not. (B) The ROI of the whole liver superimposed on b = 0 mm^2/s image. (C) Proton density fat saturated (PDFS) image showing anatomical image of the location.*

RESULTS

When assessing the whole liver ROI and routine 2 point diffusion mono-exponential fitting (i.e. b=0 s/mm^2 and b= chosen diffusion weighting) *FA*, λ_1, λ_2, λ_3 and *MD*, all decreased with increasing b-values, with the decrease being most rapid with b < 50 s/mm^2 (**Figure 6.2**).

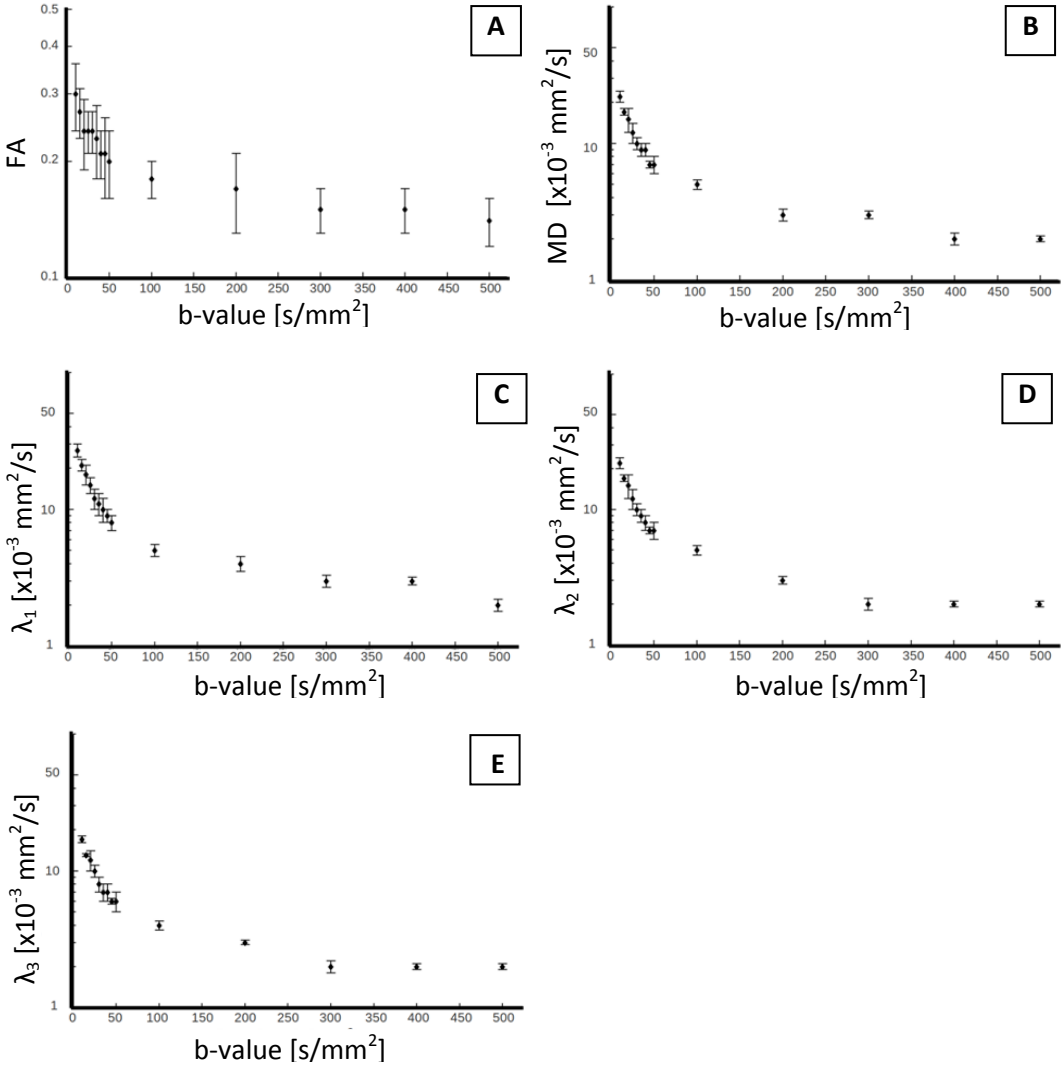

Figure 6.2: *Calculated DT metrics (FA, MD, λ_1, λ_2 and λ_3), at each b-value, using a monoexponential fit between b = 0 s/mm^2 and the set diffusion weighting b-value. For b-values less than 50s/mm,^{2} a rapid decrease in each DT metric was observed.*

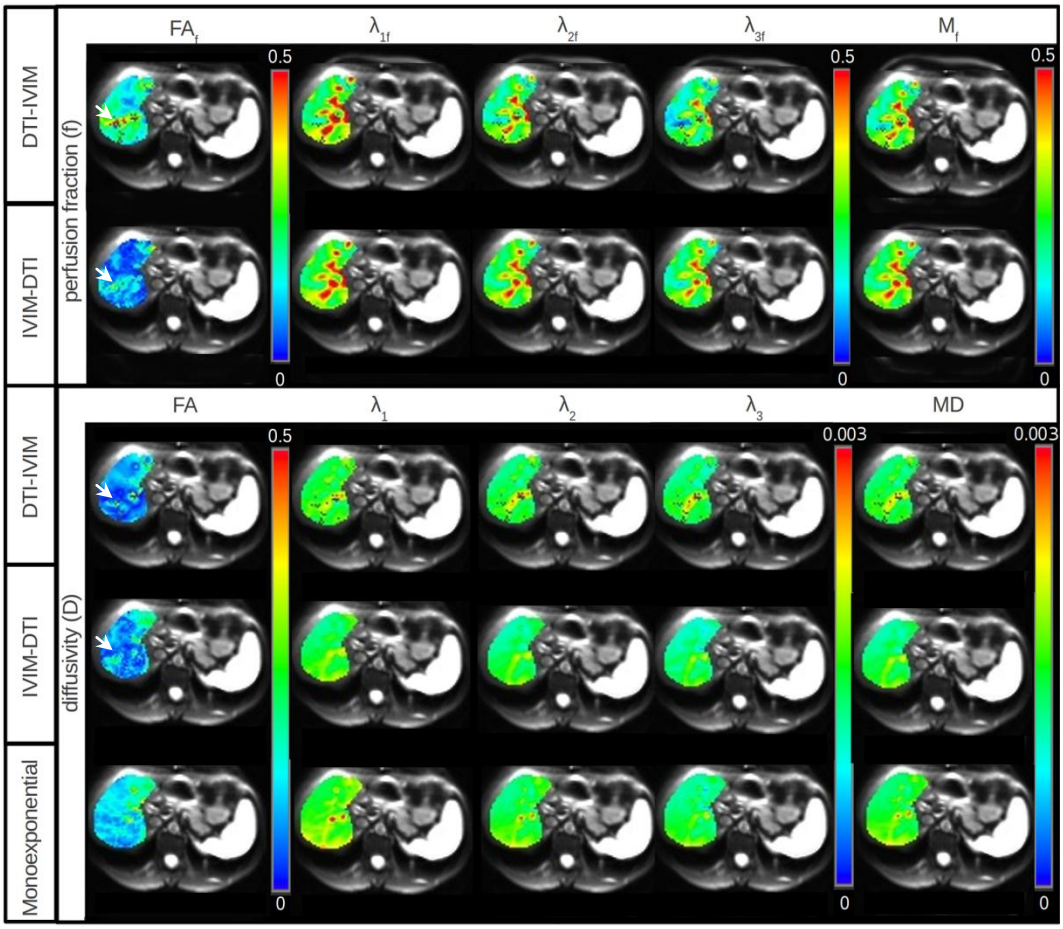

Figure 6.3: *Voxel-wise maps of IVIM-DTI, DTI-IVIM and routine DTI metrics from one volunteer scan, over a single slice. Although similar patterns were observed with IVIM-DTI, DTI-IVIM and conventional DTI approaches, DTI-IVIM occasionally fail at the area close to the vessels. Elevated FA_f next to the vessels while low FA inside the vessels were also noted using both IVIM-DTI and DTI-IVIM approaches (indicated using white arrows). Although similar observation is noted in the FA map of IVIM-DTI and DTI-IVIM approaches (indicated using white arrows), these FA maps are more homogeneous than their corresponding FA_f maps.*

The estimated voxel map of IVIM-DTI, DTI-IVIM and routine DTI metrics can be found in **Figure 6.3**, which shows the data from one volunteer scan. **Figure 6.4** shows a comparison of *FA*, λ_1, λ_2, λ_3 and *MD* for each fitting approach (i.e. IVIM-DTI and DTI-IVIM) and each ROI (liver parenchyma,

hepatic blood vessels and whole liver). Compared to whole liver, a significantly lower *FA* ($p < 0.05$) was found in the liver parenchyma ROI when using both IVIM-DTI and DTI-IVIM approaches (**Figure 6.4**). Significant differences between liver parenchyma and whole liver, and liver parenchyma and blood vessels were observed in λ_2 ($p < 0.05$) using the IVIM-DTI approach (**Figure 6.4**). Significant difference between λ_3 ($p < 0.05$) obtained using DTI-IVIM approach and conventional DTI was observed in the whole liver ROI (**Figure 6.4**).

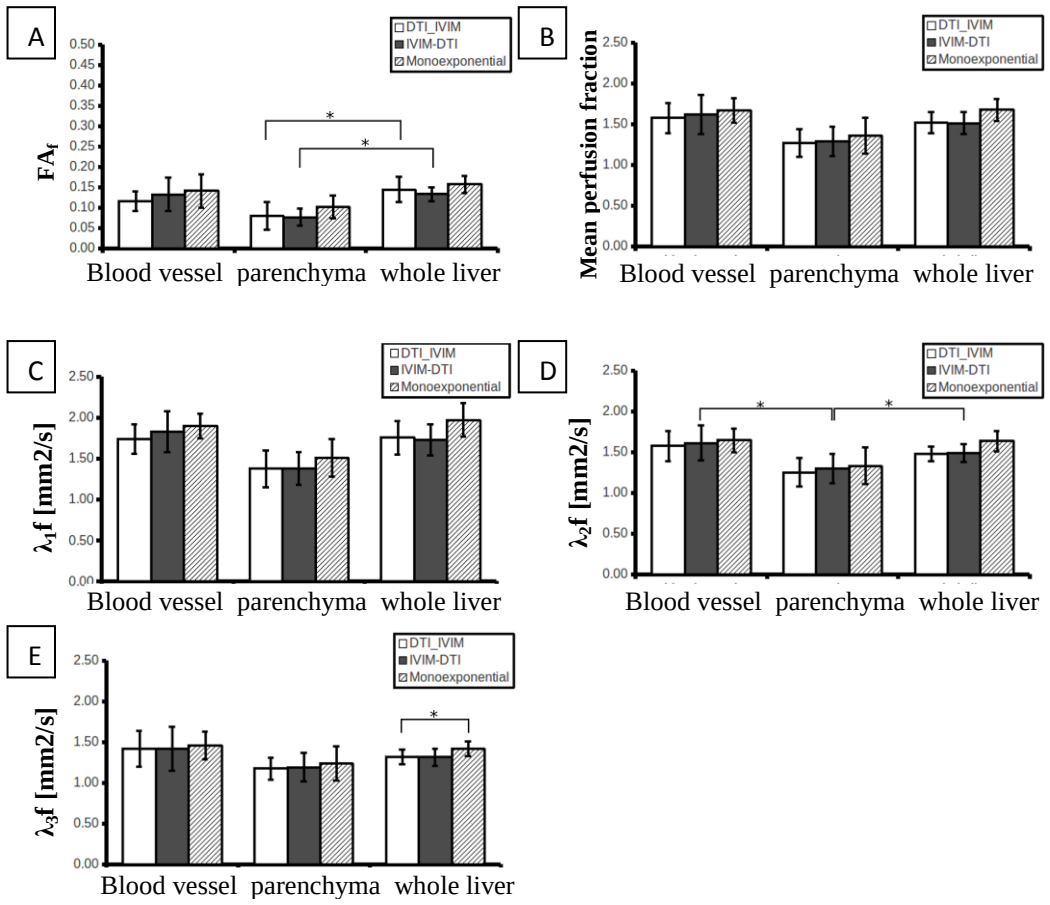

Figure 6.4: *Comparison of diffusion metrics (FA, MD, λ_1, λ_2 and λ_3) obtained using IVIM-DTI, DTI-IVIM and a standard monoexponential DTI approach (i.e. 2 b-value). (A) A larger standard deviation for hepatic blood vessel FA, liver parenchyma FA and whole liver FA were observed using DTI-IVIM. Compared to whole liver FA, significantly reduced liver parenchyma FA was observed using DTI-IVIM and IVIM-DTI approaches. (D) Significantly reduced λ_2 in liver parenchyma was observed with the IVIM-DTI approach. (E) A significant difference between DTI-IVIM and a conventional DTI approach was observed with λ_3 of whole liver (* $p<0.05$).*

Figure 6.5 shows that significantly larger FA_f ($p<0.05$) was observed using the DTI-IVIM approach, when compared to the IVIM-DTI method. We

also noted a larger standard deviation in the FA_f using DTI-IVIM approach for the ROIs of hepatic blood vessel and whole liver (**Figure 6.5**). Significantly larger λ_{3f} (p<0.05) was also observed in liver parenchyma, compared to whole liver, using DTI-IVIM.

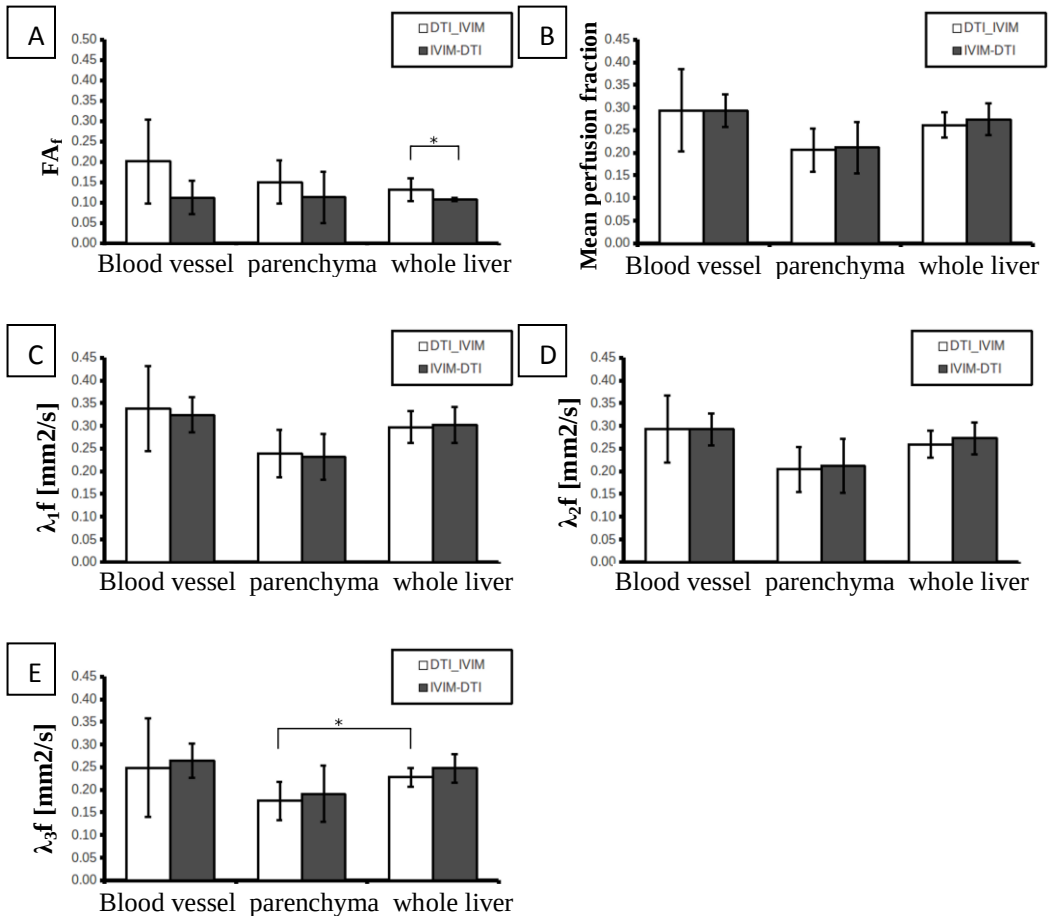

Figure 6.5: *Comparison between of perfusion metrics (FA_f, M_f, λ_{1f}, λ_{2f}, and λ_{3f}) between IVIM-DTI and DTI-IVIM. (A-D) A larger standard deviation in hepatic blood vessel diffusion measures and whole liver FA were observed using DTI-IVIM. Significantly increased whole liver FA was observed using DTI-IVIM, compared to IVIM-DTI. (E) Significantly lower FA for liver parenchyma and whole liver FA, relative to blood vessel, was observed using DTI-IVIM. (* p<0.05)*

The fitting result of the IVIM-DTI, DTI-IVIM and monoexponential DTI using whole liver ROI diffusion signal averaged between volunteers are illustrated in **Figure 6.6**. Lowest adjusted R^2 was obtained using monoexponential DTI (adjusted $R^2 = 0.904$). Slightly larger adjusted R^2 was obtained using IVIM-DTI (adjusted $R^2 = 0.982$), when compared DTI-IVIM (adjusted $R^2 = 0.980$).

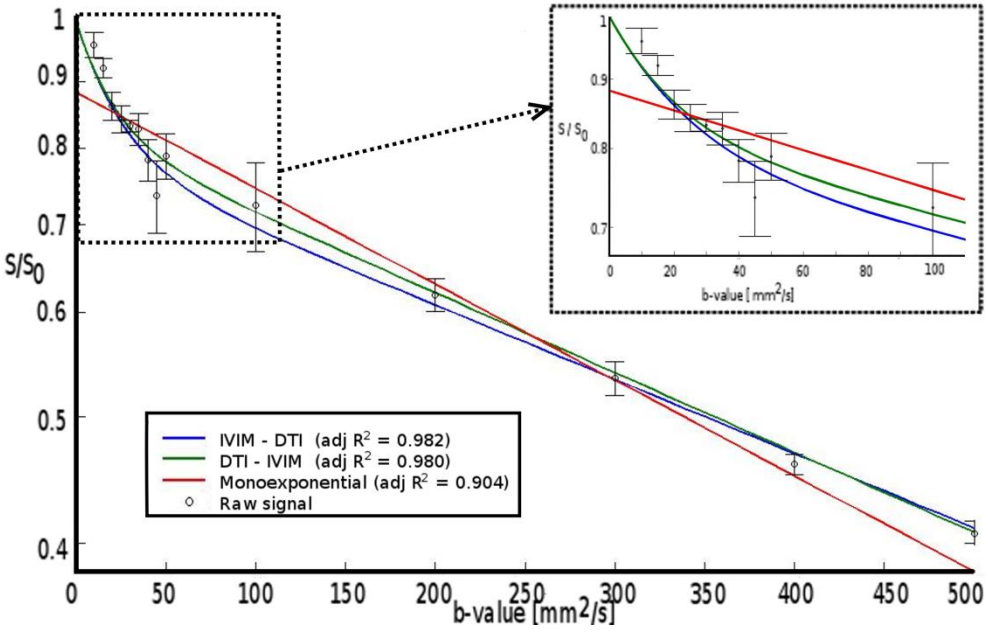

Figure 6.6: *Normalized signal as a function of b-value, shown on a semi-log scale. The data were poorly modeled using a monoexponential model, and biexponential is unequivocally the best choice. Although signal at perfusion region were poorly fitted using IVIM-DTI or DTI-IVIM technique, IVIM-DTI showed better measurement quantification of the measured signal at the diffusion region.*

DISCUSSION

We verified that a combination study of IVIM and DTI is feasible in human liver, when appropriate motion compensation is applied. Although the regularity of the hepatic lobule shape is still debated [5], true liver diffusion

should be close to isotropic [3]. Given the histological organization of liver parenchyma, our proposed combined approaches reduced liver FA to something that appears more reasonable. We suggest this could make such an approach that could be more sensitive to diagnosing diffusive liver disease.

Although the direction of liver sinusoidal (i.e. liver capillaries) blood flow and true water diffusion are assumed to be independent of b-value and fitting model, the magnitude of both can be affected by diffusion weighting as previously demonstrated in fitting of monoexponential brain DTI [19,20,21]. To the best of our knowledge, our work is the first to show the effect of b-value on liver DT metrics where DT metrics are elevated at low b-values (**Figure 6.2**), likely due to the microvascular perfusion effect. While the plot of measured diffusion signal with b-values are not shown, the log normal of our diffusion signals exhibit non-monoexponential behaviour with b-value, as suggested in the literature, which would lead to unreliable parameters if this observation not taken into consideration [22]. In fact, reduction in DT metrics with b-value also exhibit non-monoexponential behaviour as demonstrated in **Figure 6.2**. The choice of b-value, thus, leads to variation in estimated DT metrics; monoexponential DTI calculation is less reliable than non-monoexponential DTI calculation. Although our proposed IVIM-DTI approach makes use of the unit eigenvector from the conventional DTI approach, it mainly influences the estimation of flow and diffusivity direction. The effect on the magnitude of estimated IVIM-DTI metrics should be minimal.

The *ADC* and *MD* using either conventional DWI or DTI have been reported to be 1.52±0.15 x10^{-3} and 1.51±0.21 x10^{-3} mm^2/s, respectively [23]. Yamada *et al*. reported *D* and *f* from the IVIM model, in healthy human liver, to be 0.76±0.27 x10^{-3} s/mm^2 and 0.29±0.14, respectively [24]. Similar results have been reported by Luciani *et al*. using an IVIM fit, where *ADC*, *D* and *f* of healthy human liver were measured as 1.39±0.2 x10^{-3} s/mm^2, 1.10±0.7 x10^{-3} s/mm^2 and 0.27±0.05, respectively [25]. We obtained comparable liver parenchyma measures of *MD* and M_f using IVIM-DTI, with *MD*=1.29±0.18 x 10^{-3} s/mm^2 and M_f=0.21±0.06. Furthermore these values were not significantly different from the same calculated using the DTI-IVIM approach (*MD*=1.25±0.17 x 10^{-3} s/mm^2 and M_f=0.20±0.04).

Although diffusion in liver parenchyma has been reported to be isotropic [3], liver DTI has been reported with unexpectedly high *FA* value [9,26]. Lu *et al.*, reported *FA* close to 0.3 and 0.4 (with b = 400s/mm^2) in healthy human and subjects with fatty liver, respectively, using a 1.5T MR system [26]. In a recent study Erturk *et al.* reported *FA*s of 0.2±0.05, 0.37±0.1 and 0.46±0.1 for liver cysts, haemangioma and metastases, respectively [27]. Recently, Nasu *et al.* [6] suggested that diffusion weighted signal attenuation is strongly influenced by motion compensation. Indeed, respiratory and cardiac motion can lead to cyclic liver deformation and hence, what has been termed pseudo-anisotropy artifact, in liver diffusion [7]. Elevated liver *FA* due to this artifact is found to be flow related in our previous work. Compared to Lu *et al.,* lower healthy liver *FA* was

obtained using a multiple b-value monoexponential DTI calculation (0.10±0.03). The calculated *FA* of liver parenchyma was even lower using both DTI-IVIM and IVIM-DTI fitting (0.08±0.03 and 0.08±0.02, respectively) (p =0.058 for both case). The difference between our results and the literature reported *FA* may be attributed to the different choices of b-value and/or the fitting method.

As illustrated in Fig. 3, increased in λ_{1f}, λ_{2f} and λ_{3f} were obtained in the vessels using both IVIM-DTI and DTI-IVIM approaches. Opposite, low FA_f value inside the vessel was revealed based on the voxel map. However, it is also noted that higher FA_f value was observed in the liver parenchyma near to these large vessels (**Figure 6.3**). Depends on the choice of ROI, the both regions were often included within the ROI. The observed pattern is, thus, not otherwise reflected in our ROI-bases result (**Figure 6.4** and **Figure 6.5**). In addition, this effect is less obvious in the *FA* maps using both approaches. It is, therefore, suspected that non-linear liver motion is prominent near the large vessels, which is likely due to pulsation. As such, the increased FA_f value due to pseudo-hepatic anisotropic artifact is observed. When compared with the FA_f map, the corresponding *FA* map is more homogeneous. Furthermore, liver parenchyma *FA* was significantly lower than whole liver *FA* using both DTI-IVIM and IVIM-DTI approaches (p<0.05), which was not otherwise observed using monoexpoential DTI fit. Since IVIM involves the separation of the flow and diffusion components, lowered liver parenchyma *FA* may therefore be resulted.

Both IVIM-DTI and DTI-IVIM approaches exhibit excellent fitting robustness to raw signal (adjusted R^2 = 0.982 and 0.980, respectively) (**Fig. 6**). Ideally, both DTI-IVIM and IVIM-DTI approach are expected to show a similar fitting performance because they are only differ by the order of which DTI and IVIM is performed during the metrics estimation. However, it is noted that DTI-IVIM occasionally failed to provide physiological reasonable metrics during the fitting process. These voxels were considered as outlier and were rejected in this work during the calculation. Since the IVIM fitting was only conducted on S/S_{01}, S/S_{02} and S/S_{03}, FA and FA_f cannot be obtained when the results from any of these fitted data sets were rejected. Although similar problem were also observed during the estimation of IVIM-DTI metrics, these fitting results were rejected prior to application of pseudo-inverse, where in total of 20 sets of fitted data were utilized in this study. In addition, the minimum number of 3 fitted data sets is required to solve for the IVIM-DTI metrics in an ideal situation. Based on these results, IVIM-DTI is more effective and is potentially useful in reliable diagnosis of diffusive liver disease.

Despite that IVIM-DTI approaches may be potentially useful in improving diagnostic sensitivity of diffusive liver disease, further studies are needed. According to Jones [28], at least 20 non-coplanar gradient directions should be done for robust anisotropy estimation and at least 30 non-coplanar gradient directions for robust estimation of tensor orientation and mean diffusivity. Although our choice on the number of diffusion gradient is less than 30 (the

minimum requirement for tensor orientation and mean diffusivity estimation), consideration on a feasible breath holding time should be taken in our case. Moreover, the optimal number of gradient direction using IVIM-DTI approach in liver are yet to be determined. Lastly, we did not include any patient with disease in this study. Rigorous clinical validations are also warranted in future studies.

CONCLUSION

In this pilot study, IVIM-DTI and DTI-IVIM techniques have been shown to be feasible in the liver using multiple breath holds and image registration. Significantly lowered *FA* in liver parenchyma, when comparing to whole liver *FA*, were obtained using both IVIM-DTI and DTI-IVIM approaches. Moreover, IVIM-DTI is more robust and provides better fitting efficiency then DTI-IVIM. Since IVIM involves the separation of the flow and diffusion components which in turn lowered liver parenchyma *FA*, IVIM-DTI is also potentially useful in minimizing the effect of hepatic pseudo-anisotropy artifact to the estimated true diffusivity. In other words, better diffusive liver disease differentiation can potentially be done using IVIM-DTI.

REFERENCES

1. Koh DW, Collins DJ. Diffusion –Weighted MRI in the Body: Applications and Challenges in Oncology. AJR 2007; 188: 1622-1635.
2. Le Bihan D, van Zijl P. From the diffusion coefficient to the diffusion tensor. NMR Biomed 2002; 15:431-434
3. Taouli B, Vilgrain V, Dumont E, Daire JL, Fan B, Menu Y. Evaluation of Liver Diffusion Isotropy and Characteristization of Focal Hepatic Lesions with Two Single-Shot Echo-planar MR Imaging Sequences: Prospective Study in 66 Patients. Radiology 2003; 226:71-78.
4. Teutsch HF. The Modular Microarchitecture of Human Liver. Hepatology 2005: 42; 317-325
5. Debbaut C, Segers P, Cornillie P, Casteleyn C, Dierick M, Laleman W and Monbaliu D. Analyzing the liver vascular architecture by combining vascular corrosion casting and micro-CT scanning: a feasibility study. J anat. 2014; 224:509-517
6. Nasu K, Kuroki Y, Fujii H, Minami M. Hepatic pseudo-anisotropy: a specific in hepatic diffusion-weighted images obtained with respiratory triggering. Magn Reson Mater Phy 2007; 20:205-211.
7. Wong OL, Lo GG, Lee R, Li WW, Chan PL, Yu SK, Noseworthy MD. The effect of respiratory and cardiac motion in liver DTI. J Comput Assist Tomogr. 43; 38:352-359.

8. Dong Q, Welsh RC, Chenevert TL, Carlos RC, Maly-Sundgren P, Gomez-Hassan DM, Mukherji SK. Clinical Applications of Diffusion Tensor Imaging. J Magn Reson Imaging 2004; 19;6-18.
9. Erturk SM, Ichikawa T, Kaya E, Yapici O, Ozel A, Mahmutoglu AS and Basak M. Diffusion tensor imaging of cysts, hemagiomas, and metastases of the liver. Acta Radiologica 2013; published online Sep 16 DOI: 10.1177/0284185113504916.
10. Mulkern Rv, Gudbjartsson H, Westin CF, Zengingounl HP, Gartner W, Guttman CR, Robertson RL, Kyriakos W, Schwartz R, HolzmanD, Jolesz FA, Maier SE. Multi-component apparent diffusion coefficients in human brain. NMR Biomed 1999; 12:51-62.
11. Clark CA, Le Bihan D. Water diffusion compartmentation and anisotropy at high b values in human brain. Magn Reson Med 2000; 44:852-859.
12. Koh DW, Collins D, Orton M. Intravoxel Incoherent Motion in Body Diffusion-Weighted MRI: Reality and Challenges. AJR 2011; 196:1351-1361.
13. Karampinos DC, King KF, Sutton BP and Georgiadis JG. Intravoxel Partially coherent motion technique: characterization of the anisotropy of skeletal muscle microvasculature. J Magn Reson Imaging 2010: 31;942-953
14. Natohamiprodjo M, Chandarana H, Mikheev A, Raya JG, Grinstead J, Feiweier T, Rusinek H, Lee VS, Sigmund E. Combined IVIM and DTI for simultaneous assessment of diffusion and flow anisotropy of the kidney.

Proceeding of the 20th ISMRM Scientific Meeting, Melbourne, Australia, 2012. p.110.

15. Le Bihan D, Turner R, MacFall JR. Effects of Intravoxel incoherent motions (IVIM) in steady-state free precession (SSFP) imaging: application to molecular diffusion imaging. Magn Reson Med 1989; 10:324-337.
16. Kingsley P. Introduction to Diffusion Tensor Imaging Mathematics: Part I. Tensors, Rotations and Eigenvectors. Concepts Magn. Reson. 2006; 28:101-122.
17. Tuch D, Wedeen VJ, Dale AM, George JS, Belliveau JW. Conductivity tensor mapping of the human brain using diffusion tensor MRI. Proc Natl Acad Sci U S A; 2001; 98:11697-701
18. Behrens TEJ, Woolrich MW, Jenkinson M, Johansen-Berg H, Nunes RG, Clare S, Matthews PM, Brady JM, Smith SM. Characterization and propagation of uncertainty in diffusion-weighted MR imagine. Magn Reson Med 2003; 50:1077-1088.
19. Hui E, Cheung MM, Chan KC, Wu EX. B-value dependence of DTI quantitation and sensitivity in detecting neural tissue changes. NeuroImage 2010; 49: 2366-2374.
20. Jones DK, Basser PJ. "Squashing peanuts and smashing pumpkins": How noise distorts diffusion-weighted MR data. Magn Reson Med 2004; 52:979-993

21. Melhem R, Itoh R, Jones L, Barker P B. Diffusion tensor MR imaging of the brain: effect of diffusion weighting on trace and anisotropy measurements. Am J Neuroradiol 2003; 50; 510-514
22. Andreou A, Koh DM, Collins DJ, Blackledge M, Wallace T, Leach MO, Orton MR. Measurement reproducibility of perfusion fraction and pseudodiffusion coefficient derived by intravoxel incoherent motion diffusion-weighted MR imaging in normal liver and metastases. Eur Radiol 2013; 23:428-34
23. Taouli B, Martin AJ, Qayyum A, Merriman RB, Vigneron D, Yeh BM, Coakley FV. Parallel Imaging and Diffusion Tensor Imaging for Diffusion-Weighted MRI of the Liver: Preliminary Experience in Healthy Volunteers. AJR 2004; 183:677-680.
24. Yamada I, Aung W, Himeno Y, Nakagawa T, Shibuya H. Diffusion coefficients in abdominal organs and hepatic lesions: evaluation with intravoxel incoherent motion echo-planar MR imaging. Radiology 1999: 210:617-23
25. Luciani A, Vignaud A, Cavet M, Van Nhieu JT, Mallat A, Ruel L, Laurent A, Deux J, Brugieres P, Rahmouni A. Liver Cirrhosis: Intravoxel Incoherent Motion MR Imaging – Pilot Study. Radiology 2008; 249:891-899.
26. Lu L, Haus JM, Kirwan JP, Flask CA. Liver DTI of Obese Insulin Resistant Subjects with Fatty Liver Disease. Proceeding of the 18th ISMRM Scientific Meeting, Stockholm, Sweden, 2010. p.4710.

27. Erturk SM, Ichikawa T, Kaya E, Yapici O, Ozel A, Mahmutoglu AS and Basak M. Diffusion tensor imaging of cysts, hemagiomas, and metastases of the liver. Acta Radiologica 2013; published online Sep 16 DOI: 10.1177/0284185113504916.

28. Jones DK. The effect of gradient sampling schemes on measures derived from diffusion tensor MRI: a monte Carlo study. Magn Reson Imaging 2001; 13:769-80

CHAPTER 7

CONCLUSION AND FUTURE DIRECTIONS

7.1 CONCLUDING REMARKS

Many liver diseases are associated with a change in hepatic collagen content [80]. Many researchers have tried to non-invasively diagnose liver disease using DWI, while relating the microscopic water diffusion to the structural changes that accompany diseased liver tissue [42,44]. Although DWI is a useful imaging tool, it lacks the ability to provide rotationally invariant information on tissue structural properties, such as diffusion anisotropy, which can be only be obtained if diffusion is encoded as a tensor (i.e. DTI). The diffusion tensor is mathematically more suitable for describing the spatial organization of tissue micro-structures than DWI [71]. Furthermore, DTI has been developed and studied in the brain since the mid-1990s [60], inferring it is a well established and accepted MRI method. Extending diffusion MRI from brain to the abdomen is possible using most clinical scanners. Thus, there is growing research interest in liver DTI in hopes of improving the sensitivity of probing microstructural changes that accompany liver diseases. To date, there are a limited number of publications examining liver DTI, where high liver FA (close to the FA of muscle and sometimes even brain tissues) has been reported [42,71]. One drawback in liver diffusion imaging is motion and the subsequent effect of DTI metrics. In this work, it was suspected that a high FA value is the result of artificially increased diffusion weighted signal modulation that results due to non-linear liver motion.

This artefact is also known as the pseudo-hepatic anisotropy artifact. To address this issue, the thesis examined the change in DT metrics at various phases throughout the cardiac cycle.

Another drawback regarding liver DWI is the assumed monoexponential diffusion weighted signal change with increasing b-value. The work of Yamada *et al*. has shown that diffusion weighted signal modulation in the liver exhibits bi-exponential behaviour [45]. As such, IVIM should be performed to avoid overestimation of true water diffusion, which would otherwise be observed if a conventional liver DWI technique is performed [45]. In addition, IVIM involves quantification of microcapillary perfusion as well as true diffusion, which have been shown to be useful in diagnosing liver disease [45]. Based on previous results, cirrhotic liver has been shown to have a lower *f* value compared to healthy liver [41] and this hepatic change results in reduction in the pseudo-hepatic anisotropy artifact [78]. The work in this thesis, therefore evaluated whether the pseudo-hepatic anisotropy artifact mainly affects microcapillary perfusion. The spatial distribution of the voxel-wise IVIM metrics was studied using a clustering technique. In this technique, liver parenchyma that is most susceptible to the pseudo-hepatic anisotropy artefact is in the left liver lobe (due to elevated motion due to cardiac contractility) and this was expected to correspond to a higher *f* value than that in the right liver lobe (less susceptible to cardiac contractility).

Overall, the goal of this thesis was to evaluate the effect of pseudo-hepatic anisotropy artifact on the quality of DT and IVIM metrics, and to develop a

potential solution to minimize the effect of pseudo-hepatic anisotropy artifact. It was hypothesized that the effect of small non-linear liver motion on DT metrics could be minimized using multiple gradient directions. In addition, the thesis aimed at developing a better mathematical approach to characterize liver microstructure. Thus, an evaluation of the feasibility of the simultaneous assessment of IVIM and DTI using healthy human livers was examined.

7.2 MAIN FINDINGS AND CONCLUSIONS

In the first study (Chapter 3), inter-session and intra-session repeatability of liver DT metrics were evaluated. An overall acceptable repeatability was observed, where most of our DT metric CVs fell within previously reported ranges. When a large ROI encompassing the whole liver was chosen, the best intra-session and inter-session DT metrics repeatability was obtained. This is probably because the motion effect was compensated for with the use of a large ROI. The thesis work also aimed at understanding the effect of the choice of NSA and NGD on inter-session DT metric repeatability. Hence, four NSA/NGD combinations were chosen (1/30, 3/10, 3/12 and 5/6) while maintaining a similar level of STE. Although increased NGD was hypothesized to be of use in improving inter-session repeatability [65], our results did not confirm this. In previous work looking at muscle, a smaller NGD was reported for reliable estimation of muscle DT metrics due to less restricted water diffusion in muscle,

compared to brain [86]. In the case of liver, using points from the muscle work, an even smaller NGD is required for reliable liver DT metrics, where water diffusion is even less restricted in the liver than in the muscle tissues (i.e. liver sinusoids are the leakiest microvasculature in the body). To assess the effect of number of signal averages (NSA), 6 direction DTI was performed using 9 NSA settings (ranging from 1 to 9). The repeatability of DT metrics improved with increasing NSA. This result is similar to that previously reported from human brain [74] and muscle DTI data [86].

As the pseudo-hepatic anisotropy artifact is hypothesized to be related to cardiac and respiratory induced liver motion and hence spatial deformation, its effect will be reflected in altered DT (Chapter 4). The effect of respiratory motion was investigated though the comparison between the DT metrics from free-breathing and breath-holding acquisitions. Based on the results, respiratory motion leads to a significant elevation of FA, MD and tensor eigenvalues. In the second part of this study, the effect of cardiac motion was evaluated at eight trigger delay settings (0, 50, 100, 200, 300, 400, 500, and 600 ms), where respiration motion compensation was done using breath-holding. Surprisingly, with cardiac and respiratory motion compensation, FA in the left liver lobe, still varied during the cardiac cycle. Furthermore, significantly elevated liver FA was observed at systole in the left liver lobe, while no significant cardiac cycle variation was observed in the right. As the left liver lobe is proximal to the heart, it is more susceptible to deformation during heart beating. Therefore, it can be

generalized from this work that pseudo-hepatic anisotropy artifact leads to changes in liver DT metrics.

In the third study (Chapter 5), the effect of pseudo-hepatic anisotropy artifact on IVIM metrics was investigated. From the second study (Chapter 4), the pseudo-hepatic anisotropy artifact was prominent in the left liver lobe. Changes in IVIM metrics were therefore most evident in the left liver lobe. To minimize the bulk respiratory and pseudo-hepatic anisotropy artifact, the use of multiple gradient directions was explored. When combined with forced shallow free breathing, the use of a 6 gradient direction IVIM fit showed a slight improvement over the use of a single gradient direction.

Although the benefit of a multiple gradient direction IVIM approach was revealed in the third study (Chapter 5), the directional information was not fully utilized. Thus, two approaches (IVIM-DTI and DTI-IVIM) were proposed in the simultaneous assessment of IVIM and DTI in the fourth study (Chapter 6). Both IVIM-DTI and DTI-IVIM approaches showed a significant reduction in the liver parenchyma FA values when compared with whole liver FA, where the same result was not observed in conventional DTI approach. As shown in the third study (Chapter 4), the pseudo-hepatic anisotropy artifact mainly affects perfusion related IVIM metrics. The observed reduction in FA using IVIM-DTI and DTI-IVIM approaches did not only match with findings in the third study, but it also agreed with an expected liver FA value (i.e. 0, or near isotropic). Although both IVIM-DTI and DTI-IVIM approaches showed excellent adjusted R^2, the IVIM-

DTI approach seemed more effective and thus would be the ideal approach for us in a further investigation on structural changes that occur in liver disease.

7.3 CONTRI BUTIONS OF THIS WORK

There are three studies on liver DTI using human livers and all have reported higher FA values then the expected FA~0 [42,88]. All of these studies did not attempt to answer the cause of the observed high liver FA. Similarly to the work of Girometti *et al.*[71], liver DTI is concluded to be a repeatable measures in this study. However, that work was performed with b-value = 1000 s/mm^2 and 15 gradient directions. In our study, the intra-session and inter-session test-retest repeatability of liver DTI was evaluated with a lower b-value (300 s/mm^2). Furthermore, the effect of SNR and number of diffusion encoding gradient directions to the inter-session repeatability was also evaluated in this study. We noted that liver DT metric repeatability is related to SNR but not to number of diffusion encoding gradient directions, which has not been reported. We also found that liver DT metrics are dependent on the phase of the cardiac cycle. In particular, a higher FA value is observed at systole (hypothesized to result in the largest liver deformation) than at diastole. Although signal modulation in the left liver lobe has been suggested to be the result of non-linear liver motion in previous studies [89], the current work is the first relating the pseudo-hepatic anisotropy artifact to the cardiac contractile motion using liver DTI.

Other than liver DTI, the effect of IVIM metrics in the presence of pseudo-hepatic anisotropy artifact has been investigated [78]. Based on results from this thesis, elevated perfusion related IVIM metrics have been observed in the left liver lobe, where the pseudo-hepatic anisotropy artifact is more pronounced. This finding agrees with previous work where lower IVIM derived *f* was noted in cirrhotic liver parenchyma [41], which has been observed to be less deformable [78]. However, the relationship between the pseudo-hepatic anisotropy artifact and IVIM metrics in healthy liver has not been investigated. Indeed, this motion-induced error can be generalized into voxel shift error and phase error [57]. Although previous techniques have improved the IVIM fit by correcting the motion induced voxel shift error, the error in signal phase is ignored [59]. The work in this thesis has improved the IVIM fit by minimizing the phase error (thought to be related to the pseudo-hepatic anisotropy artifact) using multiple non-coplanar diffusion encoding directions. To fully utilize the directional information, the feasibility of the simultaneous assessment of IVIM and DTI in healthy human livers has been explored in the thesis. Two approaches (IVIM-DTI and DTI-IVIM) have been proposed where the IVIM-DTI approach has been inspired from the work of Natohamiprojo [62] in human kidney. Compared to the published results from the literature, a lower FA value was obtained using both IVIM-DTI and DTI-IVIM approaches, which is closer to what would be expected for healthy liver parenchyma (i.e. close to isotropic diffusion). The *FA* map from both IVIM-DTI and DTI-IVIM approaches were noted to be more homogeneous

than the FA_f map. The reason was suggested due to separation of the pseudo-hepatic anisotropy artifact from true diffusion. When comparing IVIM-DTI and DTI-IVIM approaches, the former was found to be slightly more effective based on results from this thesis. Therefore, it is believed that IVIM-DTI would be the better approach to assessing and grading diseased liver.

7.4 POSSIBLE APPLICATIONS AND FUTURE STUDIES

The studies in this thesis have revealed that the pseudo-hepatic anisotropy artifact, prominent in the liver left lobe, results in changes in both liver DT metrics and liver IVIM metrics. Furthermore, it was found that this artifact mainly affects the perfusion related IVIM metrics. The proposed IVIM-DTI approach reduces artificially inflated liver FA in the diffusion region, where high FA from the previously published data using routine DTI is likely due to the pseudo-hepatic anisotropy artifact. The separation of the pseudo-hepatic anisotropy artifact from the true diffusion should better reveal the microstructural change associated with diseased liver tissues.

In order to apply IVIM–DTI clinically more studies are required to optimize the number of gradient encoding directions. Here the IVIM-DTI protocol was performed using 20 diffusion encoding gradient directions with multiple breath-holds. However, this choice was based on similar work in kidney [62]. Although the optimum number of diffusion encoding gradient for repeatable DTI measures

was found be 6 in this work, further study is still needed to refine the optimal number of gradient directions for the IVIM-DTI protocol. But as the breath holding paradigm was often challenging, even for healthy volunteers, it is questionable whether the scanning done here would even be possible in people with illness. Future applications of IVIM-DTI should focus on concurrent cardiac and respiratory triggering, and the use of faster acquisitions, such as multiband DTI or compressed sensing. Optimum selection of b-values should also be investigated for the further improvement in estimation of IVIM-DTI metrics. With implementation of these changes, the clinical usefulness of IVIM-DTI could better be evaluated.

The relationship between the pseudo-hepatic anisotropy artifact and liver deformation revealed in this work is based on the DT metric change seen throughout the cardiac cycle. Although it can be assumed that the degree of liver deformation is related to liver stiffness, the correlation between liver stiffness and liver DT metrics should still be investigated. As MR elastography (MRE) is an expensive hardware addition to an MR system, and ultrasound is operator dependent and hence minimally quantitative, having a metric that correlates with elastography would be invaluable. Since the pseudo-hepatic anisotropy artifact mainly affected perfusion IVIM metrics, the proposed IVIM-DTI approach would be most suited to correlate against liver stiffness. Therefore, a study comparing MRE, DTI and IVIM-DTI of patients diagnosed with liver cirrhosis would be a reasonable next step for future work in this area.

IVIM-DTI allows estimation of not only perfusion metrics, but also structural measures such as FA and eigenvalues. As such, IVIM-DTI should be superior to both DTI and IVIM technique as separate techniques. Studies evaluating the sensitivity and specificity of IVIM-DTI in diagnosing and staging liver metastasis, which have higher regional blood volume and blood flow, should be done in the future, comparing to contrast enhanced MRI and liver biopsy.

7.5 CONCLUDING STATEMENT

Although there is a growing interest in applying DTI to the assessment of liver disease, research in liver DTI is still in its infancy. Better assessment of liver disease may be possible though the evaluation of the effect of psudo-hepatic anisotropy artifact of liver DTI and IVIM, performed in this work. By combining DTI and IVIM techniques, a better mathematical description of both microvascular perfusion, capillary spatial orientation and true water diffusion could be performed. This level of detail provided by the IVIM-DTI technique could be useful in non-invasively diagnosing and grading liver diseases.

BIBLIOGRAPHY

1. Magkos F, Fabbrini E, Klein S. Pathogenesis of Hepatic Steatosis and Fibrosis: Role of Leptin. In: Leptin. Springer; 2015. pp. 89–101.

2. Martini FH. Fundamentals of Anatomy & Physiology. 7 edition. San Francisco, CA: Benjamin Cummings; 2005.

3. Hussain SM. Appendix II: Liver Segmental and Vascular Anatomy. In: Liver MRI: Correlation with Other Imaging Modalities and Histopathology. Springer Science & Business Media; 2007. pp. 246–247.

4. Monga SPS. Molecular Pathology of Liver Diseases. Springer US; 2011.

5. Burroughs AK. The hepatic artery, portal venous system, and portal hypertension: the hepatic veins and liver in circulatory failure. In: Sherlock's diseases of the liver and biliary system. 12th ed. Oxford: Wiley-Blackwell; 2011. pp. 152–209.

6. Moteki T, Horikoshi H. Evaluation of noncirrhotic hepatic parenchyma with and without significant portal vein stenosis using diffusion-weighted echo-planar MR on the basis of multiple-perfusion-components theory. Magn. Reson. Imaging 2011;29:64–73.

7. Afdhal NH, Nunes D. Evaluation of liver fibrosis: a concise review. Am. J. Gastroenterol. 2004;99:1160–1174.

8. Malarkey DE, Johnson K, Ryan L, Boorman G, Maronpot RR. New insights into functional aspects of liver morphology. Toxicol. Pathol. 2005;33:27–34.

9. Fehrenbach H, Weiskirchen R, Kasper M, Gressner AM. Up-regulated expression of the receptor for advanced glycation end products in cultured rat hepatic stellate cells during transdifferentiation to myofibroblasts. Hepatology 2001;34:943–952.

10. Albanis E, Safadi R, Friedman SL. Treatment of hepatic fibrosis: almost there. Curr. Gastroenterol. Rep. 2003;5:48–56.

11. Kawada N. Molecular mechanism of stellate cell activation and therapeutic strategy for liver fibrosis. Comp. Hepatol. 2004;3:S3.

12. Mabuchi A, Mullaney I, Sheard P, Hessian P, Zimmermann A, Senoo H, Wheatley AM. Role of hepatic stellate cells in the early phase of liver regeneration in rat: formation of tight adhesion to parenchymal cells. Comp. Hepatol. 2004;3:S29.

13. Pan CC, Kavanagh BD, Dawson LA, Li XA, Das SK, Miften M, Ten Haken RK. Radiation-associated liver injury. Int. J. Radiat. Oncol. Biol. Phys. 2010;76:S94–S100.

14. Marieb EN, Hoehn K. Human anatomy & physiology. Pearson Education; 2007.

15. Gebhardt R, Matz-Soja M. Liver zonation: Novel aspects of its regulation and its impact on homeostasis. World J. Gastroenterol. WJG 2014;20:8491.

16. Jungermann K, Keitzmann T. Zonation of parenchymal and nonparenchymal metabolism in liver. Annu. Rev. Nutr. 1996;16:179–203.

17. Levy AD, Mortele KJ, Yeh BM. Gastrointestinal Imaging. Oxford University Press; 2015.

18. Lawrence SP. Advances in the treatment of hepatitis C. Adv. Intern. Med. 1999;45:65–105.

19. Taouli B, Ehman RL, Reeder SB. Advanced MRI Methods for Assessment of Chronic Liver Disease. AJR Am. J. Roentgenol. 2009;193:14–27. doi: 10.2214/AJR.09.2601.

20. Hamer OW, Aguirre DA, Casola G, Lavine JE, Woenckhaus M, Sirlin CB. Fatty Liver: Imaging Patterns and Pitfalls 1. Radiographics 2006;26:1637–1653.

21. Angulo P. Nonalcoholic fatty liver disease. N. Engl. J. Med. 2002;346:1221–1231.

22. Friedman SL. Mechanisms of disease: mechanisms of hepatic fibrosis and therapeutic implications. Nat. Clin. Pract. Gastroenterol. Hepatol. 2004;1:98–105.

23. Reddy JK, Rao MS. Lipid metabolism and liver inflammation. II. Fatty liver disease and fatty acid oxidation. Am. J. Physiol.-Gastrointest. Liver Physiol. 2006;290:G852–G858.

24. Clark JM, Brancati FL, Diehl AM. Nonalcoholic fatty liver disease. Gastroenterology 2002;122:1649–1657.

25. Shimada M, Hashimoto E, Taniai M, Hasegawa K, Okuda H, Hayashi N, Takasaki K, Ludwig J. Hepatocellular carcinoma in patients with non-alcoholic steatohepatitis. J. Hepatol. 2002;37:154–160.

26. Boyer TD, Manns MP, Sanyal AJ, Zakim D. Zakim and Boyer's Hepatology: A Textbook of Liver Disease. Elsevier Health Sciences; 2011.

27. Browning JD, Szczepaniak LS, Dobbins R, Horton JD, Cohen JC, Grundy SM, Hobbs HH. Prevalence of hepatic steatosis in an urban population in the United States: impact of ethnicity. Hepatology 2004;40:1387–1395.

28. El-Serag HB. Epidemiology of hepatocellular carcinoma in the United States: Where are we? Where do we go? Hepatology 2014;60:1767–1775.

29. Saadeh S, Younossi ZM, Remer EM, Gramlich T, Ong JP, Hurley M, Mullen KD, Cooper JN, Sheridan MJ. The utility of radiological imaging in nonalcoholic fatty liver disease. Gastroenterology 2002;123:745–750.

30. Ratziu V, Charlotte F, Heurtier A, Gombert S, Giral P, Bruckert E, Grimaldi A, Capron F, Poynard T. Sampling Variability of Liver Biopsy in Nonalcoholic Fatty Liver Disease. Gastroenterology 2005;128:1898–1906.

31. Rosenberg WM, Voelker M, Thiel R, et al. Serum markers detect the presence of liver fibrosis: a cohort study. Gastroenterology 2004;127:1704–1713.

32. Lewis JR, Mohanty SR. Nonalcoholic Fatty Liver Disease: A Review and Update. Dig. Dis. Sci. 2010;55:560–578.

33. Santillan CS, Tang A, Cruite I, Shah A, Sirlin CB. Understanding LI-RADS: a primer for practical use. Magn. Reson. Imaging Clin. N. Am. 2014;22:337–352.

34. Hagmann P, Jonasson L, Maeder P, Thiran J-P, Wedeen VJ, Meuli R. Understanding Diffusion MR Imaging Techniques: From Scalar Diffusion-weighted Imaging to Diffusion Tensor Imaging and Beyond 1. Radiographics 2006;26:S205–S223.

35. Colagrande S, Pasquinelli F, Mazzoni LN, Belli G, Virgili G. MR-diffusion weighted imaging of healthy liver parenchyma: Repeatability and reproducibility of apparent diffusion coefficient measurement. J. Magn. Reson. Imaging 2010;31:912–920.

36. Dudeck O, Zeile M, Wybranski C, et al. Early prediction of anticancer effects with diffusion-weighted MR imaging in patients with colorectal liver metastases following selective internal radiotherapy. Eur. Radiol. 2010;20:2699–2706.

37. Eccles CL, Haider EA, Haider MA, Fung S, Lockwood G, Dawson LA. Change in diffusion weighted MRI during liver cancer radiotherapy: preliminary observations. Acta Oncol. 2009;48:1034–1043.

38. Hardie AD, Naik M, Hecht EM, Chandarana H, Mannelli L, Babb JS, Taouli B. Diagnosis of liver metastases: value of diffusion-weighted MRI compared with gadolinium-enhanced MRI. Eur. Radiol. 2010;20:1431–1441.

39. Patel J, Sigmund EE, Rusinek H, Oei M, Babb JS, Taouli B. Diagnosis of cirrhosis with intravoxel incoherent motion diffusion MRI and dynamic contrast-enhanced MRI alone and in combination: Preliminary experience. J. Magn. Reson. Imaging 2010;31:589–600.

40. Taouli B, Chouli M, Martin AJ, Qayyum A, Coakley FV, Vilgrain V. Chronic hepatitis: Role of diffusion-weighted imaging and diffusion tensor imaging for the diagnosis of liver fibrosis and inflammation. J. Magn. Reson. Imaging 2008;28:89–95.

41. Girometti R, Esposito G, Bagatto D, Avellini C, Bazzocchi M, Zuiani C. Is water diffusion isotropic in the cirrhotic liver? A study with diffusion-weighted imaging at 3.0 Tesla. Acad. Radiol. 2012;19:55–61.

42. Erturk SM, Ichikawa T, Kaya E, Yapici O, Ozel A, Mahmutoglu AS, Basak M. Diffusion tensor imaging of cysts, hemangiomas, and metastases of the liver. Acta Radiol. 2014;55:564-60.

43. Naganawa S, Kawai H, Fukatsu H, Sakurai Y, AOKI I, MIURA S, MIMURA T, KANAZAWA H, ISHIGAKI T. Diffusion-weighted imaging of the liver: technical challenges and prospects for the future. Magn. Reson. Med. Sci. 2005;4:175–186.

44. Girometti R, Furlan A, Esposito G, Bazzocchi M, Como G, Soldano F, Isola M, Toniutto P, Zuiani C. Relevance of b-values in evaluating liver fibrosis: A study in healthy and cirrhotic subjects using two single-shot spin-echo echo-planar diffusion-weighted sequences. J. Magn. Reson. Imaging 2008;28:411–419.

45. Yamada I, Aung W, Himeno Y, Nakagawa T, Shibuya H. Diffusion coefficients in abdominal organs and hepatic lesions: evaluation with intravoxel incoherent motion echo-planar MR imaging. Radiology 1999;210:617–623.

46. Mulkern RV, Gudbjartsson H, Westin C-F, et al. Multi-component apparent diffusion coefficients in human brain. NMR Biomed 1999;12:51–62.

47. Koh D-M, Collins DJ, Orton MR. Intravoxel incoherent motion in body diffusion-weighted MRI: reality and challenges. Am. J. Roentgenol. 2011;196:1351–1361.

48. Le Bihan D, Breton E, Lallemand D, Grenier P, Cabanis E, Laval-Jeantet M. MR imaging of intravoxel incoherent motions: application to diffusion and perfusion in neurologic disorders. Radiology 1986;161:401–407.

49. Bennett KM, Schmainda KM, Rowe DB, Lu H, Hyde JS, others. Characterization of continuously distributed cortical water diffusion rates with a stretched-exponential model. Magn. Reson. Med. 2003;50:727–734.

50. Jensen JH, Helpern JA, Ramani A, Lu H, Kaczynski K. Diffusional kurtosis imaging: The quantification of non-gaussian water diffusion by means of magnetic resonance imaging. Magn. Reson. Med. 2005;53:1432–1440.

51. Le Bihan D, Breton E, Lallemand D, Aubin ML, Vignaud J, Laval-Jeantet M. Separation of diffusion and perfusion in intravoxel incoherent motion MR imaging. Radiology 1988;168:497–505.

52. Moteki T, Horikoshi H. Evaluation of hepatic lesions and hepatic parenchyma using diffusion-weighted echo-planar MR with three values of gradient b-factor. J. Magn. Reson. Imaging 2006;24:637–645.

53. Freiman M, Perez-Rossello JM, Callahan MJ, Voss SD, Ecklund K, Mulkern RV, Warfield SK. Reliable estimation of incoherent motion parametric maps from diffusion-weighted MRI using fusion bootstrap moves. Med. Image Anal. 2013;17:325–336.

54. Lemke A, Stieltjes B, Schad LR, Laun FB. Toward an optimal distribution of b values for intravoxel incoherent motion imaging. Magn. Reson. Imaging 2011;29:766–776.

55. Dyvorne HA, Galea N, Nevers T, et al. Diffusion-weighted Imaging of the Liver with Multiple b Values: Effect of Diffusion Gradient Polarity and Breathing Acquisition on Image Quality and Intravoxel Incoherent Motion Parameters? A Pilot Study. Radiology 2013;266:920–929.

56. Orton MR, Collins DJ, Koh D-M, Leach MO. Improved intravoxel incoherent motion analysis of diffusion weighted imaging by data driven Bayesian modeling. Magn. Reson. Med. 2014;71:411–420.

57. Murphy P, Wolfson T, Gamst A, Sirlin C, Bydder M. Error model for reduction of cardiac and respiratory motion effects in quantitative liver DW-MRI. Magn. Reson. Med. 2013;70:1460–1469.

58. Jerome NP, Orton MR, d' Arcy JA, Collins DJ, Koh D-M, Leach MO. Comparison of free-breathing with navigator-controlled acquisition regimes in abdominal diffusion-weighted magnetic resonance images: Effect on ADC and IVIM statistics. J. Magn. Reson. Imaging 2014;39:235–240.

59. Mazaheri Y, Do RK, Shukla-Dave A, Deasy JO, Lu Y, Akin O. Motion correction of multi-b-value diffusion-weighted imaging in the liver. Acad. Radiol. 2012;19:1573–1580.

60. Martino J, Lucas EM. Subcortical anatomy of the lateral association fascicles of the brain: a review. Clin. Anat. 2014;27:563–569.

61. Zaraiskaya T, Kumbhare D, Noseworthy MD. Diffusion tensor imaging in evaluation of human skeletal muscle injury. J. Magn. Reson. Imaging JMRI 2006;24:402–408.

62. Notohamiprodjo M, Dietrich O, Horger W, Horng A, Helck AD, Herrmann KA, Reiser MF, Glaser C. Diffusion tensor imaging (DTI) of the kidney at 3 Tesla–feasibility, protocol evaluation and comparison to 1.5 Tesla. Invest. Radiol. 2010;45:245–254.

63. Kozlowski P, Chang SD, Meng R, Mädler B, Bell R, Jones EC, Goldenberg SL. Combined prostate diffusion tensor imaging and dynamic contrast enhanced MRI at 3T—quantitative correlation with biopsy. Magn. Reson. Imaging 2010;28:621–628.

64. Mori S. Introduction to diffusion tensor imaging. Elsevier; 2007.

65. Jones DK, Horsfield MA, Simmons A. Optimal strategies for measuring diffusion in anisotropic systems by magnetic resonance imaging. Magn Reson Med 1999;42:515-25.

66. Basser PJ, Mattiello J, LeBihan D. MR diffusion tensor spectroscopy and imaging. Biophys. J. 1994;66:259.

67. Baltzer PA, Schelhorn J, Benndorf M, Dietzel M, Kaiser WA. Diagnosis of focal liver lesions suspected of metastases by diffusion-weighted imaging (DWI):

systematic comparison favors free-breathing technique. Clin. Imaging 2013;37:97–103.

68. Alexander AL, Lee JE, Lazar M, Field AS. Diffusion Tensor Imaging of the Brain. Neurother. J. Am. Soc. Exp. Neurother. 2007;4:316–329.

69. Sundgren PC, Dong Q, Gomez-Hassan D, Mukherji SK, Maly P, Welsh R. Diffusion tensor imaging of the brain: review of clinical applications. Neuroradiology 2004;46:339–350.

70. Cheung JS, Fan SJ, Gao DS, Chow AM, Man K, Wu EX. Diffusion tensor imaging of liver fibrosis in an experimental model. J. Magn. Reson. Imaging 2010;32:1141–1148.

71. Girometti R, Maieron M, Lissandrello G, Bazzocchi M, Zuiani C. Test–retest reliability of diffusion tensor imaging of the liver at 3.0 T. Radiol. Med. (Torino) 2014:1–9.

72. Mohammadi S, Hutton C, Nagy Z, Josephs O, Weiskopf N. Retrospective correction of physiological noise in DTI using an extended tensor model and peripheral measurements. Magn. Reson. Med. 2013;70:358–369.

73. Hui ES, Cheung MM, Chan KC, Wu EX. B-value dependence of DTI quantitation and sensitivity in detecting neural tissue changes. Neuroimage 2010;49:2366–2374.

74. Farrell JA, Landman BA, Jones CK, Smith SA, Prince JL, van Zijl PC, Mori S. Effects of SNR on the accuracy and reproducibility of DTI-derived fractional anisotropy, mean diffusivity, and principal eigenvector measurements at 1.5 T. J. Magn. Reson. Imaging JMRI 2007;26:756.

75. Ni H, Kavcic V, Zhu T, Ekholm S, Zhong J. Effects of number of diffusion gradient directions on derived diffusion tensor imaging indices in human brain. Am. J. Neuroradiol. 2006;27:1776–1781.

76. Noseworthy MD, Haider MA, Sussman MS, Wright GA. Free-breathing motion compensation using template matching: a technique allowing for tracer kinetic modeling of liver metastases. J. Comput. Assist. Tomogr. 2007;31:193–197.

77. Chen X, Qin L, Pan D, Huang Y, Yan L, Wang G, Liu Y, Liang C, Liu Z. Liver diffusion-weighted MR imaging: reproducibility comparison of ADC measurements obtained with multiple breath-hold, free-breathing, respiratory-triggered, and navigator-triggered techniques. Radiology 2014;271:113–125.

78. Nasu K, Kuroki Y, Fujii H, Minami M. Hepatic pseudo-anisotropy: a specific artifact in hepatic diffusion-weighted images obtained with respiratory triggering. Magn. Reson. Mater. Phys. Biol. Med. 2007;20:205–211.

79. Jenkinson M, Bannister P, Brady M, Smith S. Improved optimization for the robust and accurate linear registration and motion correction of brain images. Neuroimage 2002;17:825–841.

80. Debbaut C, Segers P, Cornillie P, Casteleyn C, Dierick M, Laleman W, Monbaliu D. Analyzing the human liver vascular architecture by combining vascular corrosion casting and micro-CT scanning: a feasibility study. J. Anat. 2014;224:509–517.

81. Guiu B, Petit J-M, Capitan V, et al. Intravoxel incoherent motion diffusion-weighted imaging in nonalcoholic fatty liver disease: a 3.0-T MR study. Radiology 2012;265:96–103.

82. Ismail MH, Pinzani M. Reversal of Liver Fibrosis. Saudi J. Gastroenterol. Off. J. Saudi Gastroenterol. Assoc. 2009;15:72–79.

83. Taouli B, Vilgrain V, Dumont E, Daire J-L, Fan B, Menu Y. Evaluation of liver diffusion isotropy and characterization of focal hepatic lesions with two single-shot echo-planar MR imaging sequences: prospective study in 66 patients. Radiology 2003;226:71–78.

84. Karampinos DC, King KF, Sutton BP, Georgiadis JG. Intravoxel partially coherent motion technique: characterization of the anisotropy of skeletal muscle microvasculature. J. Magn. Reson. Imaging JMRI 2010;31:942–953.

85. Anderson AW. Theoretical analysis of the effects of noise on diffusion tensor imaging. Magn. Reson. Med. 2001;46:1174–1188.

86. Froeling M, Nederveen AJ, Nicolay K, Strijkers GJ. DTI of human skeletal muscle: the effects of diffusion encoding parameters, signal-to-noise ratio and T2 on tensor indices and fiber tracts. NMR Biomed. 2013;26:1339–1352.

87. Wong OL, Goh Lo G, Lee R, Li WW, Chan PL, Yu SK, Noseworthy MD. The effect of respiratory and cardiac motion in liver diffusion tensor imaging (DTI). J. Comput. Assist. Tomogr. 2014;38:352–359.

88. Lu L, Haus JM, Kirwan JP, Flask CA. Liver DTI of obese insulin resistant subjects with fatty liver disease. In: Proceedings of the 18th Annual Meeting of ISMRM, Stockholm, Sweden. ; 2010. p. 4710.

89. Kwee TC, Takahara T, Niwa T, Ivancevic MK, Herigault G, Van Cauteren M, Luijten PR. Influence of cardiac motion on diffusion-weighted magnetic resonance imaging of the liver. Magma N. Y. N 2009;22:319–325.